LEVEL

AD A097740

DTIC
SELECTED
13 APR 1981

C

13 march 1981

81 4 13 084

ADAPTRONICS, INC.

Westgate Research Park

1750 Old Meadow Road • McLean, Virginia 22102

①

⑭ ADI-Ref-531

⑨ FINAL TECHNICAL REPORT, 15 Mar 78 – 15 Mar 81,

⑥ DEVELOPMENT OF AN ADVANCED, AUTOMATIC,
ULTRASONIC NDE IMAGING SYSTEM VIA ADAPTIVE
LEARNING NETWORK SIGNAL PROCESSING TECHNIQUES.

APPROVED FOR PUBLIC RELEASE
DISTRIBUTION UNLIMITED

⑩ Leo J. /O'Brien
Nancy A. /Aravanis
James R. /Gouge, Jr.
Anthony N. Mucciardi

DTIC
SELECTED
13 APR 198
C

⑪ 13 Mar 81

⑫ 151

Prepared for:

DEFENSE ADVANCED RESEARCH PROJECTS AGENCY
1400 Wilson Boulevard
Arlington, Virginia 22209
Under Contract MDA903-78-C-0223, (A03553)

⑮ N DARPA Order-3553

Prepared by:

ADAPTRONICS, INC.
1750 Old Meadow Road
McLean, Virginia 22102

003350

REPORT DOCUMENTATION PAGE

READ INSTRUCTIONS
BEFORE COMPLETING FORM

1. REPORT NUMBER	2. GOVT ACCESSION NO.	3. RECIPIENT'S CATALOG NUMBER
0042E	AD-A097740	--

4. TITLE (and Subtitle)	5. TYPE OF REPORT & PERIOD COVERED
Development of an Advanced, Automatic, Ultrasonic NDE Imaging System Via Adaptive Learning Network Signal Processing Techniques	Final Technical Report 3/15/78 - 3/15/81
	6. PERFORMING ORG. REPORT NUMBER

7. AUTHOR(s)	8. CONTRACT OR GRANT NUMBER(s)
Leo J. O'Brien, Nancy A. Aravanis James R. Gouge, Jr. and Anthony N. Mucciardi	MDA903-78-C-0223 NEW DARPA Order-3553

9. PERFORMING ORGANIZATION NAME AND ADDRESS	10. PROGRAM ELEMENT, PROJECT, TASK AREA & WORK UNIT NUMBERS
Adaptronics, Inc. 1750 Old Meadow Road McLean, Fairfax County, VA 22102	DAR 4-113, MIL STD 847A DAR 7-104.9 A03553

11. CONTROLLING OFFICE NAME AND ADDRESS	12. REPORT DATE
DCASMA, Baltimore, 300 E. Joppa Road Room 200 Towson, MD 21204	March 13, 1981
	13. NUMBER OF PAGES
	137

14. MONITORING AGENCY NAME & ADDRESS(if different from Controlling Office)	15. SECURITY CLASS. (of this report)
Defense Advanced Research Projects Agency 1400 Wilson Blvd. Arlington, VA 22209	Unclassified
	15a. DECLASSIFICATION/DOWNGRADING SCHEDULE

16. DISTRIBUTION STATEMENT (of this Report)

APPROVED FOR PUBLIC RELEASE
DISTRIBUTION UNLIMITED

17. DISTRIBUTION STATEMENT (of the abstract entered in Block 20, if different from Report)

Same as Report

18. SUPPLEMENTARY NOTES

To be published by: Electric Power Research Institute
3412 Hillview Avenue, P. O. Box 10412
Palo Alto, CA 94303

19. KEY WORDS (Continue on reverse side if necessary and identify by block number)

Ultrasonic Imaging
Adaptive Learning Networks
Defect Characterization

Signal Processing
Linear Arrays

20. ABSTRACT (Continue on reverse side if necessary and identify by block number)

A conventional pulse-echo imaging system has been modified to operate with a linear ultrasonic array and associated digital electronics to collect data from a series of defects fabricated in aircraft quality steel blocks. A thorough analysis of the defect responses recorded with this modified system has shown that considerable improvements over conventional imaging approaches can be obtained in the crucial areas of defect detection and characterization. A combination of advanced signal processing concepts with the Adaptive Learning Network (ALN) methodology forms the basis for these improvements. Use of established signal processing algorithms such as temporal and spatial beam-

DD FORM 1473 EDITION OF 1 NOV 65 IS OBSOLETE
1 JAN 73

20. ABSTRACT (continued)

forming in concert with a sophisticated detector has provided a reliable defect detection scheme which can be implemented in a microprocessor-based system to operate in an automatic mode. It is shown that signal features extracted from the detected responses contain diagnostic information which enables the defect to be characterized as to type, orientation, and size. Direct comparisons are made between conventional defect images and results obtained from this study; these demonstrate the improvements obtained with the new approach.

Accession For

NTIS GRA&I

DTIC TAB

Unannounced

Justification

By

Distribution/

Availability Codes

Avail and/or

Special

No. of Copies	Name and Address
2 (each)	Director DARPA Attention: Program Management Defense Advanced Research Projects Agency 1400 Wilson Blvd. Arlington, VA 22209
1 (each)	Attention: Dr. Gary J. Dau Electric Power Research Institute 3412 Hillview Avenue P. O. Box 10412 Palo Alto, CA 94303
1 (each)	Attention: Dr. Michael J. Buckley Rockwell International Science Center 1049 Camino Dos Rios P. O. Box 1085 Thousand Oaks, CA 91360
12 (each)	Defense Documentation Center Cameron Station Alexandria, VA 22314

FOREWORD

This is the Final Technical Report under the subject contract. This research was sponsored by the Defense Advanced Research Projects Agency under DARPA Order No. 3553, Contract No. MDA903-78-C-0223, monitored by Dr. Michael J. Buckley.

Effective Date: 15 March 1978

Expiration Date: 15 March 1981

Reporting Period: 15 March 1978 to 15 March 1981

NOTE: "The views and conclusions contained in this document are those of the authors and should not be interpreted as necessarily representing the official policies, either expressed or implied, of the Defense Advanced Research Projects Agency or the United States Government."

ABSTRACT

A conventional pulse-echo imaging system has been modified to operate with a
linear ultrasonic array and associated digital electronics to collect data
from a series of defects fabricated in aircraft quality steel blocks. A
thorough analysis of the defect responses recorded with this modified system
has shown that considerable improvements over conventional imaging approaches
can be obtained in the crucial areas of defect detection and characterization.
A combination of advanced signal processing concepts with the Adaptive Learn-
ing Network (ALN) methodology forms the basis for these improvements. Use of
established signal processing algorithms such as temporal and spatial beam-
forming in concert with a sophisticated detector has provided a reliable
defect detection scheme which can be implemented in a microprocessor-based
system to operate in an automatic mode. It is shown that signal features
extracted from the detected responses contain diagnostic information which
enables the defect to be characterized as to type, orientation, and size.
Direct comparisons are made between conventional defect images and results
obtained from this study; these demonstrate the improvements obtained with the
new approach.

ACKNOWLEDGEMENTS

TABLE OF CONTENTS

LIST OF FIGURES

LIST OF FIGURES
(Cont'd)

LIST OF FIGURES
(Cont'd)

LIST OF FIGURES
(Cont'd)

LIST OF TABLES

1. INTRODUCTION

One of the most common procedures for identifying the presence of a flaw in metals and ceramic material is the ultrasonic pulse-echo inspection technique (Wells, 1969). Conventional manual scanning procedures presently used with A-scan flaw detectors provide an initial indication of the component condition; however, under certain circumstances the echo returns from the flaws are not easily discernable because of large grain boundaries, attenuation or absorption of the reflected echo, and the masking of the defect response by large geometical reflectors. Another problem area which deserves attention concerns the subjective interpretation of the recorded data, which introduces inconsistencies that adversely impact the reliability and reproducibility of the inspection.

The objective of this effort has been to demonstrate that the problems identified above can be resolved with a higher degree of success through the use of advanced signal processing and adaptive learning network methodologies. Previous work in this area has demonstrated the advantages offered by this approach (Mucciardi, 1980). In addition to the direct improvements obtained in the detectability and characterization of the flaw responses, it should be noted that the procedures developed to accomplish these objectives can and have been implemented in a microprocessor-based system so that the flaw characteristics can be obtained automatically without the need for extensive operator interpretation.

The various components comprising the data acquisition system are described in Chapter 2. The procedures employed in collecting the ultrasonic signals with

this system are presented in detail in Chapter 3. Chapter 4 contains a discussion of the signal processing and detection algorithms used to improve the visibility of the defect responses. The feature extraction exercises and adaptive learning network models determined for defect characterization purposes are identified in Chapter 5. Conventional pulse-echo images obtained from the defect data base are shown in Chapter 6, along with improved images obtained through more sophisticated techniques. The conclusions of this effort are summarized in the final chapter with recommendations for future work efforts.

2. THE ULTRASONIC DATA ACQUISITION SYSTEM

2.1 SYSTEM DESIGN CONCEPT

The ultrasonic data acquisition system described in this chapter is composed of several distinct subsystems. The design concept of this system was based on the control of a linear array through use of a series of interconnected microprocessors which allow for the programmable selection of active transmitting and receiving elements within the array as well as for the automatic collection, digitization, and interpretation of the ultrasonic signals sensed at the receiver.

The initial design was based on commercial instrumentation provided by the Electric Power Research Institute (EPRI) and consisted of a conventional pulse-echo imaging system (Becker, et. al., 1979). This system was modified by Pacific Northwest Laboratories (BNW) through the construction of a linear array package and an array controller with a programmable attenuator capability. Adaptronics then interfaced the ALN 4000 Multi Purpose Processing System, a microprocessor-based signal acquisition and analysis system, with the other subsystems to obtain digital recordings which are analyzed for defect characterization purposes.

A block diagram of the system is shown in Figure 2.1. The major components of the data acquisition system are the scanning bridge and scanner controller (EPRI), the array package and array controller (BNW), and the ALN 4000 (manufactured for EPRI by Adaptronics). The ALN 4000 is responsible for supervising the activities of the other major system components as well as for
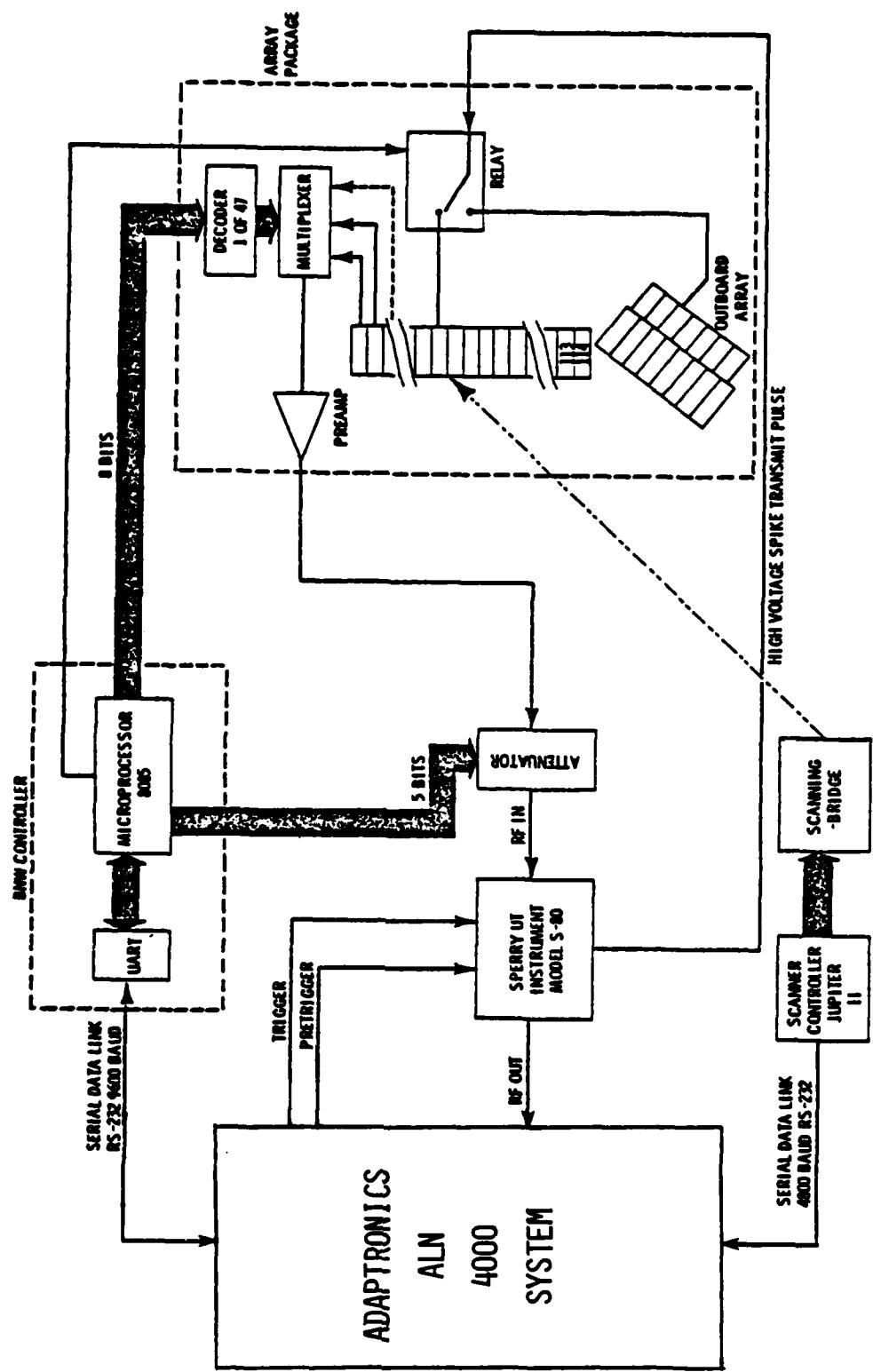
FIGURE 2.1: BLOCK DIAGRAM OF THE ALN 4000, ARRAY CONTROLLER AND SCANNING BRIDGE SYSTEM

starting and stopping the data acquisition and analysis activities. Each of
the major components comprising the data acquisition system is discussed in
detail in the sections which follow.

2.2 SCANNING BRIDGE AND CONTROLLER

The X-Y scanner covers an area of approximately 5 feet x 3 feet and positions
the ultrasonic array within this area in response to commands provided by a
Jupiter-II microprocessor system. A photograph of the scanning bridge is
shown in Figure 2.2. Communication between the ALN 4000 and the Jupiter-II is
accomplished by sending a set of specific commands from the ALN 4000 (in the
form of ASCII-coded characters) to the scanner controller over a serial data
link. In addition to this computer-controlled mode, a proportional-speed joy
stick is provided for manual scanner positioning. The scanner speed can be
set to a maximum of 6 inches/second or any binary submultiple (6.0, 3.0, 1.5,
0.75, ...) to a minimum of $6/2^{255}$. A single rate is used for both axes during
an automatic scan or during a position command. The current (X,Y) location
can be requested at any time by the ALN 4000, with these coordinates always
being relative to the point within the scanning area where the axes counters
were initialized to zero. A set of 13 different commands can be interpreted
by the controller from the ALN 4000. These include start and stop commands,
positioning operations, status requests, speed settings, and current position
requests. The format of the controller response to each command or request is
then decoded by the ALN 4000 to guarantee that the proper action has been
taken by the scanning bridge.
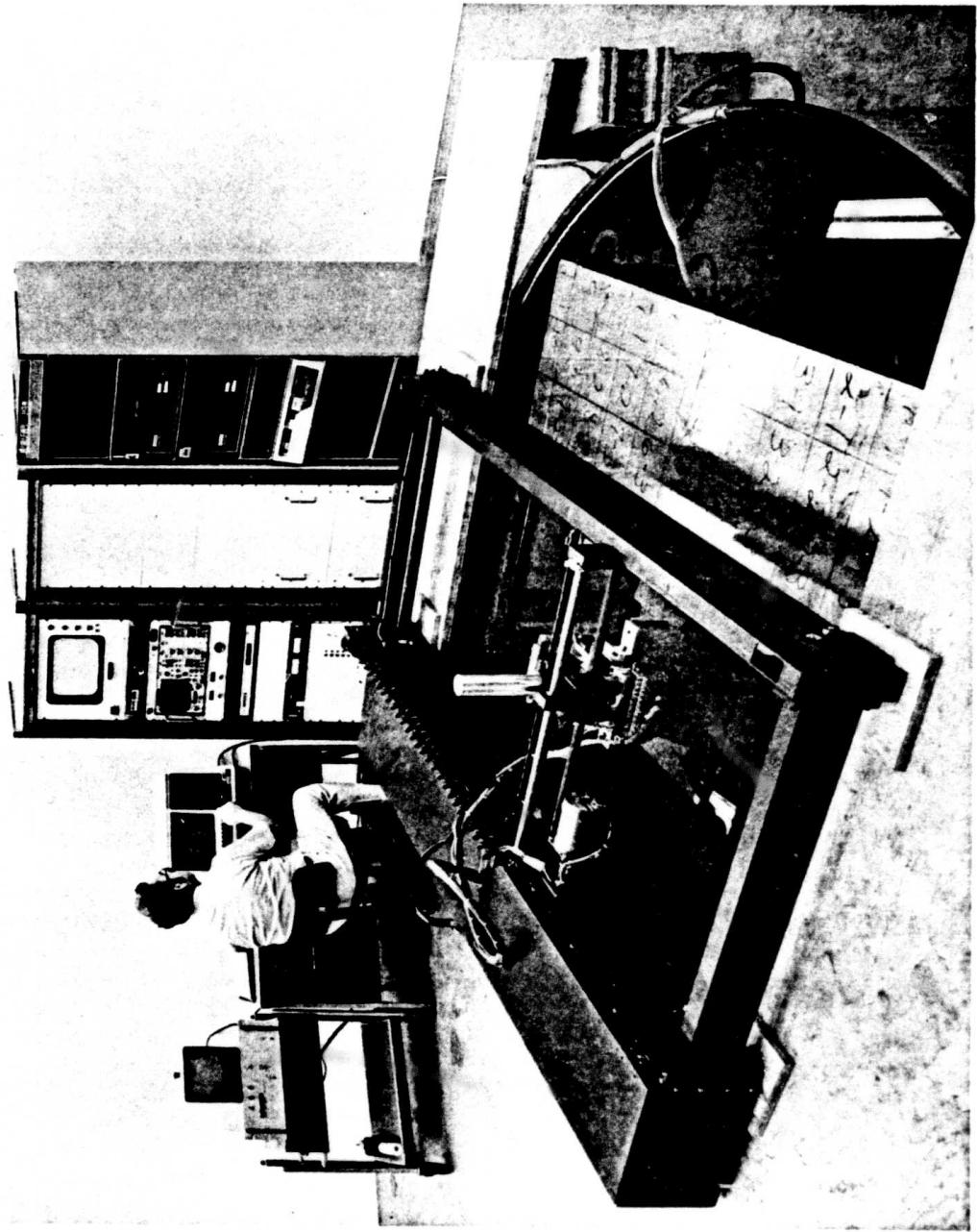
FIGURE 2.2: PHOTOGRAPH OF THE EPRI ULTRASONIC IMAGING SYSTEM HIGHLIGHTING THE X-Y SCANNER

2.3 ULTRASONIC ARRAY PACKAGE

An ultrasonic array package was fabricated by Battelle Northwest Laboratories for use in this project (Posakony, 1978). The package consists of two separate arrays which were constructed using identical procedures. The characteristics of these two arrays are shown in Figure 2.3. The long horizontal array consists of 114 individual elements, and the short angled array contains eight individual elements. A diagram illustrating the physical dimensions of the individual components is shown in Figure 2.4. Each element is 0.20 inch wide, 0.20 inch thick, and 0.50 inch long, with the center-to-center spacing between adjacent elements being 0.35 inch. The gaps between array elements have been filled with an absorptive substance which minimizes acoustic coupling or cross-talk. The entire face of the array has been protected by a thin layer of epoxy.

The outboard array consists of eight individual elements that have been electrically tied together to function as a single transmitter/receiver (#47). A goniometer has been attached to the outboard array to obtain accurate angular measurements. The inboard array is composed of 114 elements, from which a set of 47 has been selected for use in this study. The association between the receiver numbers and array elements is shown in Figure 2.5. The receiver group, 32-37, has been tied together and functions as a transmitter/receiver group within the inboard array. A photograph of the array head, goniometer, and associated electronics is shown in Figure 2.6.

A number of independent tests was performed by both BNW and Adaptronics to measure the performance of the array package. The relative sensitivity of the
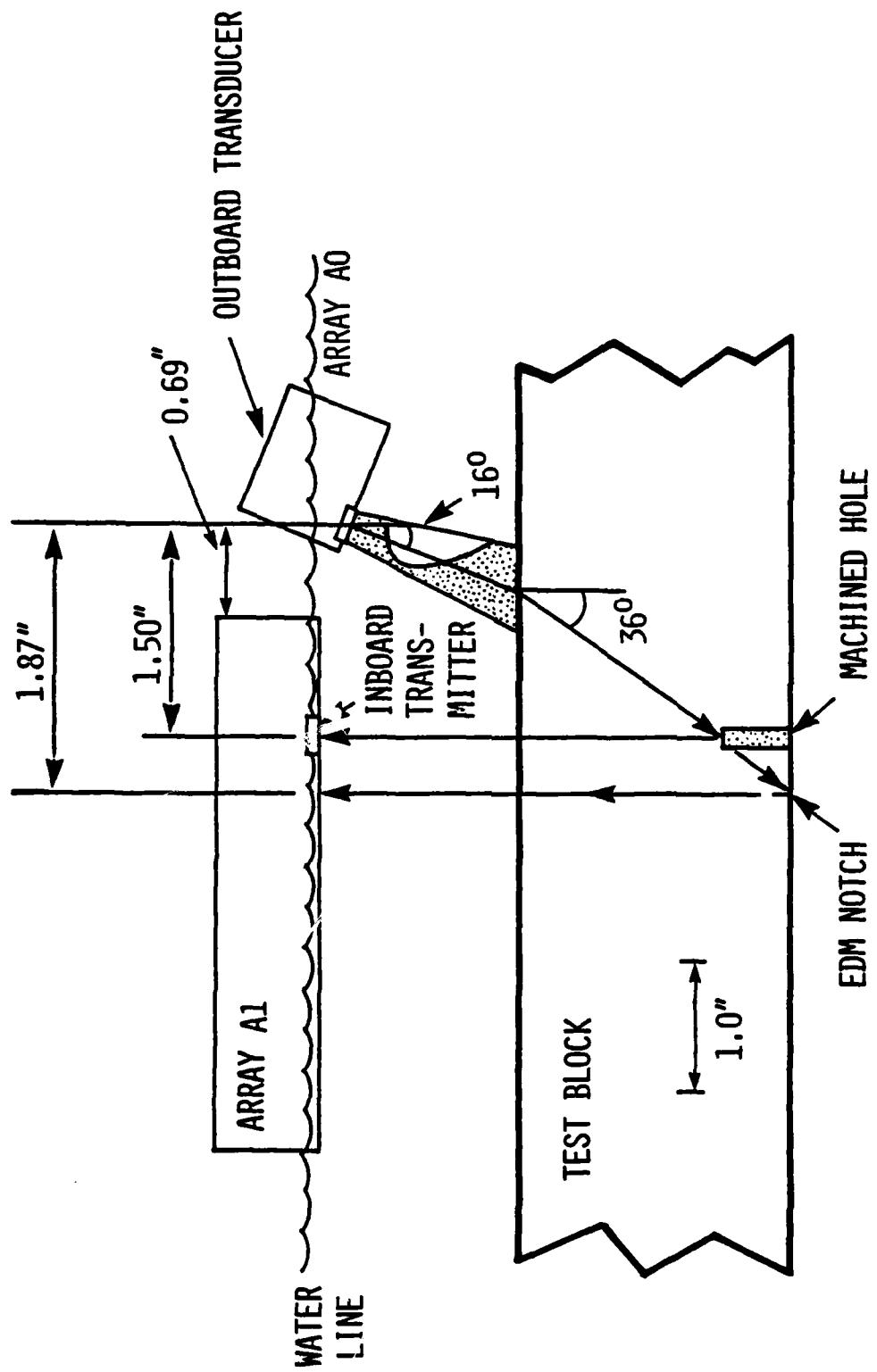
FIGURE 2.3: CHARACTERISTICS OF THE TEST BLOCK AND THE ULTRASONIC ARRAYS

LINEAR ARRAY #592

END VIEW

ELEMENT LENGTH

0.64"

0.500"

0.89"

SIDE VIEW

#592,

4.17"

BACKING

0.20"

0.020"

0.035"

ELEMENTS

FRONT OR FACE VIEW

114 ELEMENTS
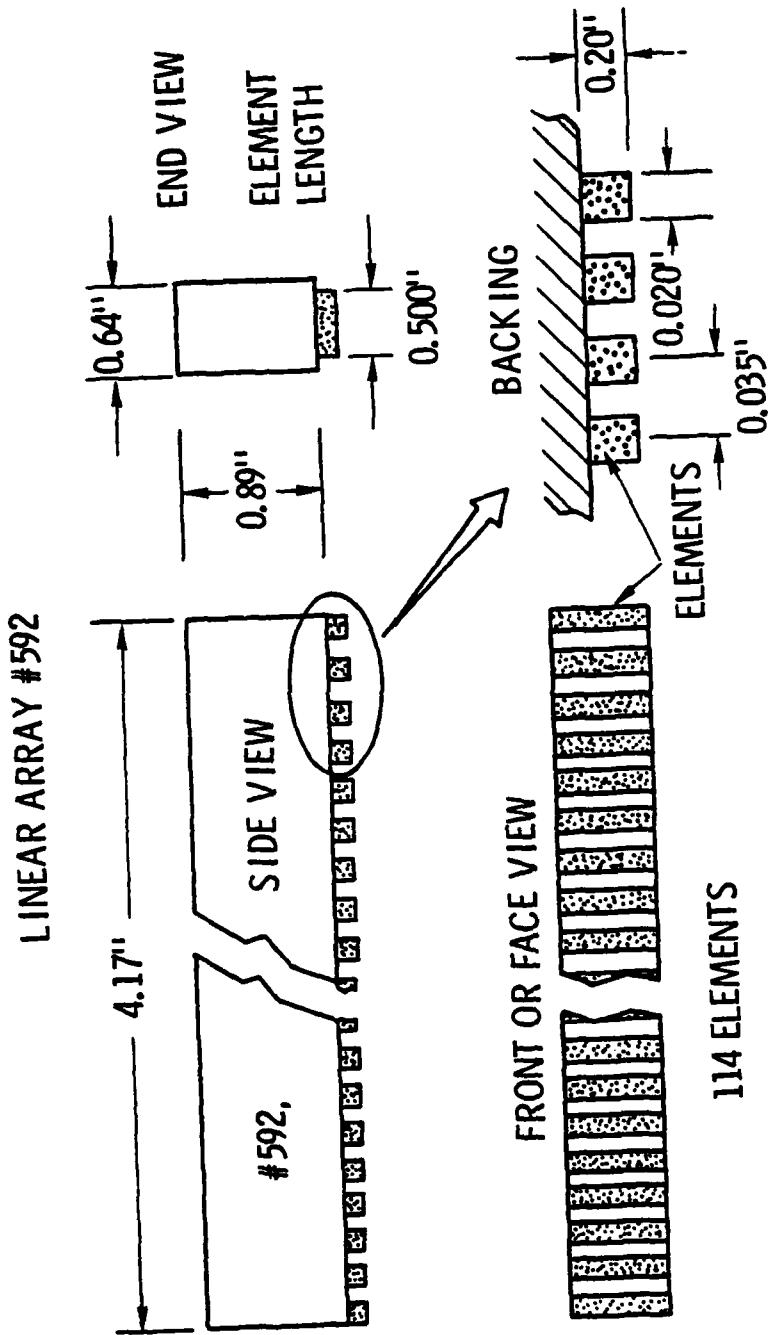
ELEMENTS

FIGURE 2.4: DIAGRAM OF THE ARRAY CONSTRUCTION
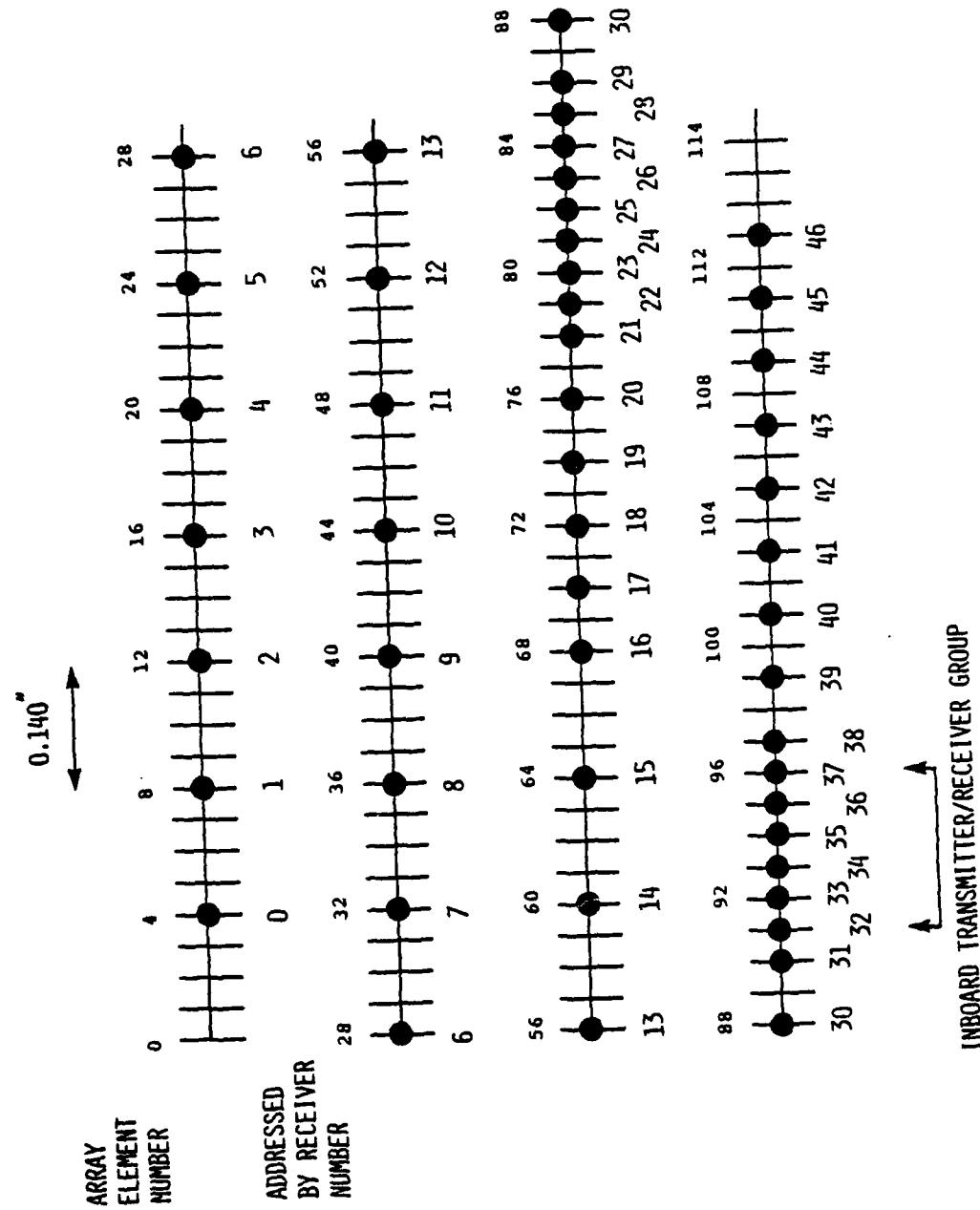
FIGURE 2.5: ASSOCIATION BETWEEN RECEIVER NUMBERS AND LINEAR ARRAY ELEMENT NUMBERS
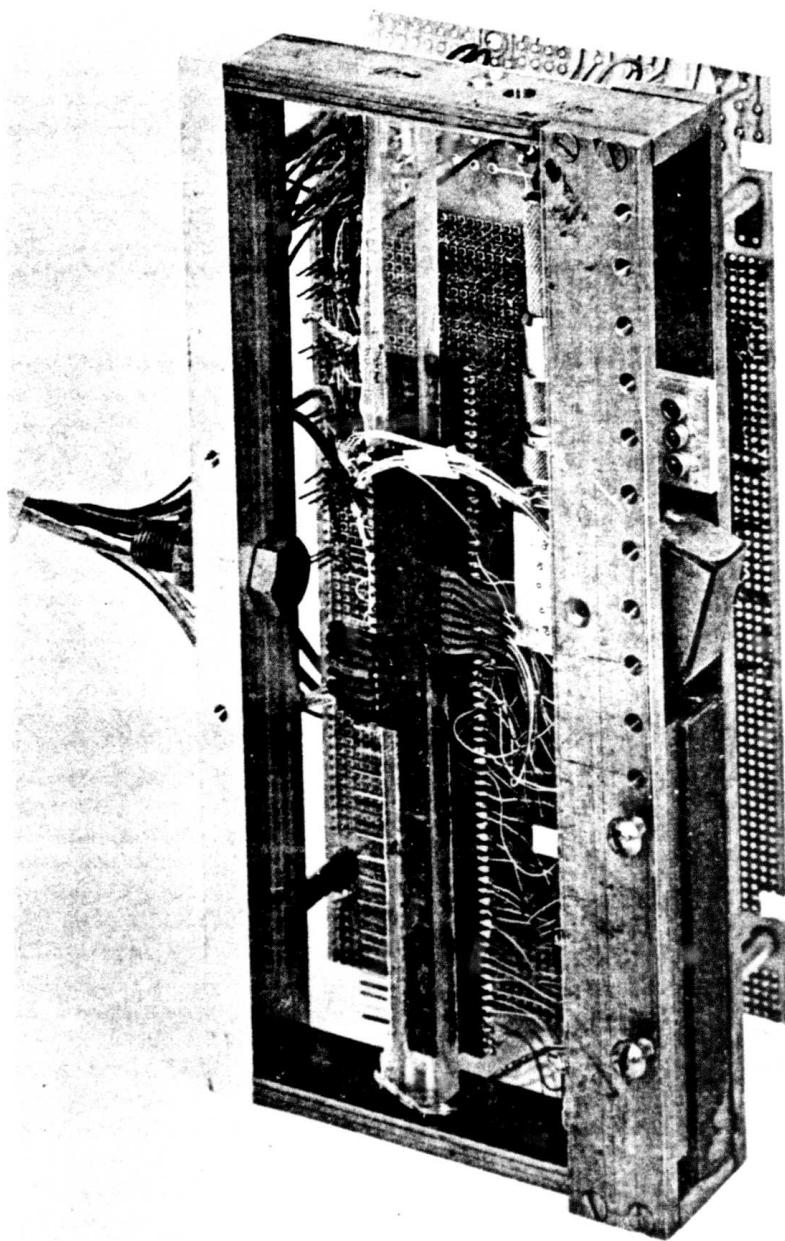
FIGURE 2.6: PHOTOGRAPH OF THE ARRAY HEAD INCLUDING THE RECEIVING ARRAY, THE OUTBOARD ARRAY AND GONIOMETER, AND THE ASSOCIATED ELECTRONICS

elements comprising the inboard array was determined by BNW by transmitting a broad-band pulse with a 20 MHz lithium sulfate transducer through a water path to each element. The maximum signal amplitude was measured for each receiver and normalized to the average value across the entire linear array section. The results of this experiment are summarized in Table 2.1 for each receiver. The normalized responses are reasonably consistent and do not exhibit wide deviations from the mean amplitude value.

A more stringent test of the array performance was conducted in which the recorded signals obtained at each receiver were digitized and analyzed. The procedure employed in this exercise is illustrated in Figure 2.7. A 2 MHz transducer was positioned at the bottom of the plastic water tank and was pulsed to transmit ultrasonic energy into the water toward the linear array. The array was successively positioned using the X-Y scanner so that each receiver element within the array was located on a direct path with the transmitter. The digitized waveforms at selected receiver locations are shown in Figure 2.8. These time-domain responses exhibit very consistent characteristics. A further check is shown in Figure 2.9, which illustrates the power spectra computed from the individual time waveforms. The spectra shown at receivers 44 and 45 indicate a slightly higher frequency content than the other array elements. This is probably related to the fact that these receivers are located near the end of the linear array, and could receive reverberations which superimpose with the directly arriving energy.

The results of these performance evaluations indicate that the individual elements comprising the inboard array exhibit consistent time-domain responses. This observation is important, since the analysis of these recordings can

TABLE 2.1: NORMALIZED RESPONSE OF LINEAR ARRAY RECEIVERS

ELEMENT	RESPONSE	ELEMENT	RESPONSE	ELEMENT	RESPONSE	ELEMENT	RESPONSE
1	1.04	31	1.12	61	.99	91	.97
2	1.04	32	1.08	62	1.00	92	.98
3	.97	33	.98	63	1.01	93	.98
4	.99	34	.99	64	1.02	94	.92
5	.97	35	.06	65	.98	95	.97
6	.96	36	1.02	66	.96	96	.92
7	.94	37	1.00	67	.96	97	.94
8	1.01	38	1.01	68	.94	98	.99
9	1.02	39	1.02	69	1.00	99	1.00
10	1.04	40	.99	70	.95	100	.94
11	1.07	41	1.00	71	.93	101	.91
12	1.09	42	1.02	72	.94	102	.95
13	1.07	43	1.02	73	.96	103	.92
14	1.97	44	1.00	74	.92	104	.91
15	1.05	45	1.01	75	.91	105	.94
16	1.05	46	.98	76	.92	106	.96
17	1.03	47	1.00	77	.94	107	.96
18	1.11	48	.99	78	.88	108	.94
19	1.13	49	1.06	79	.87	109	.93
20	1.09	50	1.08	80	.90	110	.93
21	1.10	51	1.08	81	1.06	111	.96
22	1.10	52	1.12	82	1.05	112	.97
23	1.09	53	1.05	83	1.07	113	1.01
24	1.08	54	1.02	84	.99	114	.91
25	1.06	55	.92	85	1.05		
26	1.09	56	.93	86	.96		
27	1.11	57	.93	87	.95		
28	1.14	58	.93	88	.93		
29	1.13	59	.95	89	.99		
30	1.15	60	.97	90	.99		
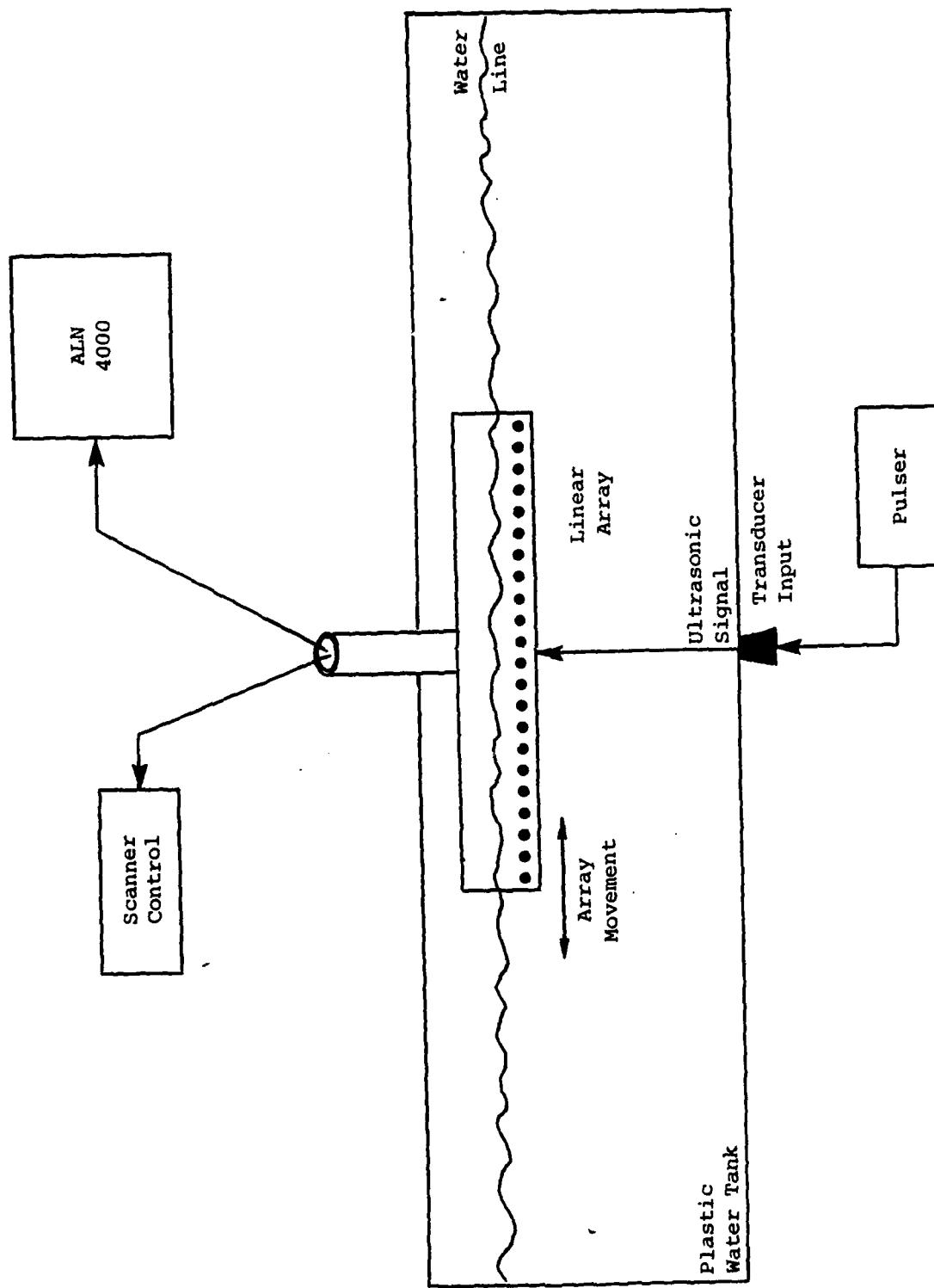
FIGURE 2.7: DESCRIPTION OF EXPERIMENT SET UP TO TEST THE RESPONSE OF THE LINEAR ARRAY
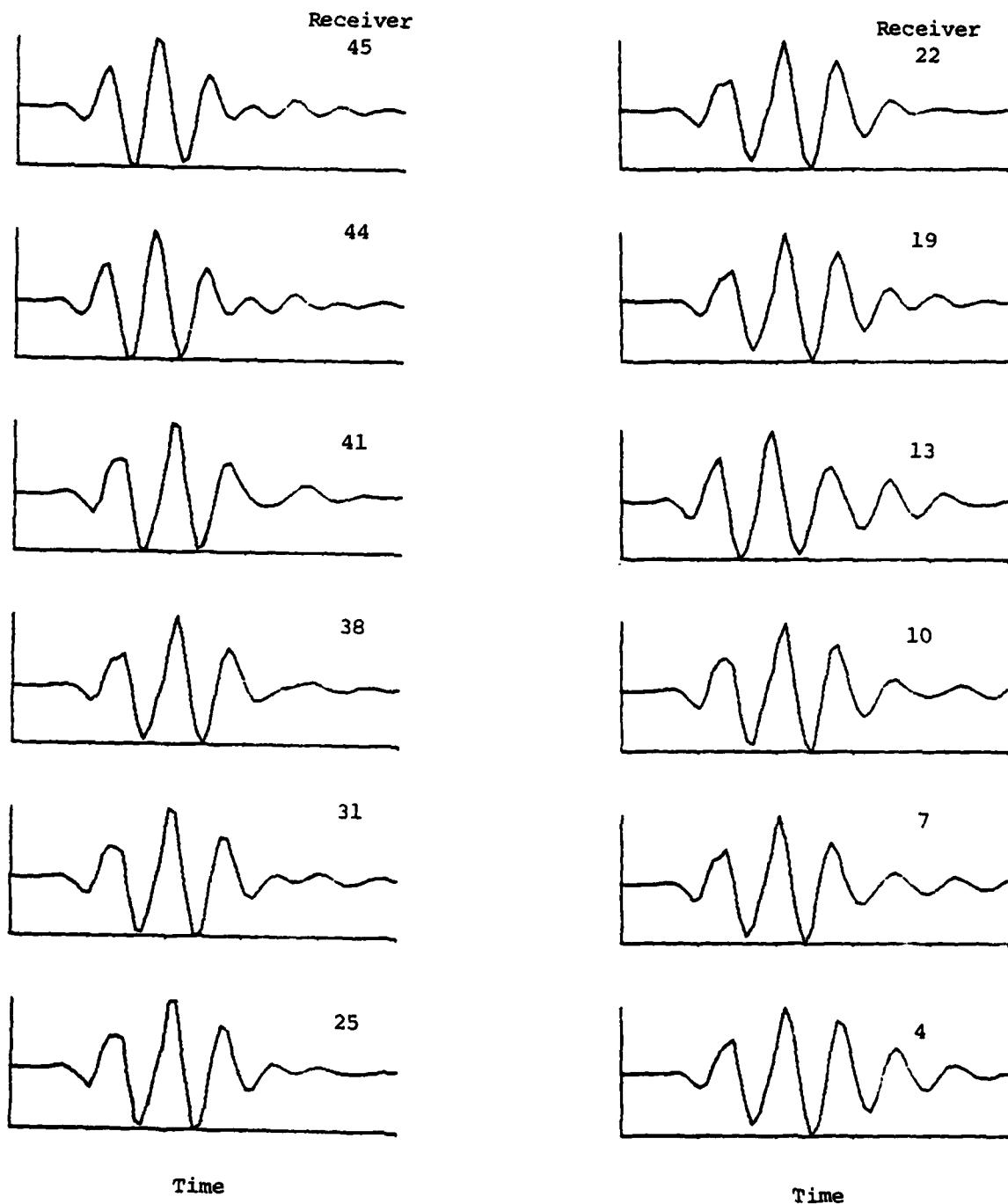
FIGURE 2.8: WAVEFORMS RECORDED AT VARIOUS RECEIVERS DURING THE
ARRAY RESPONSE TESTS (Amplitudes are all normalized
to unity)
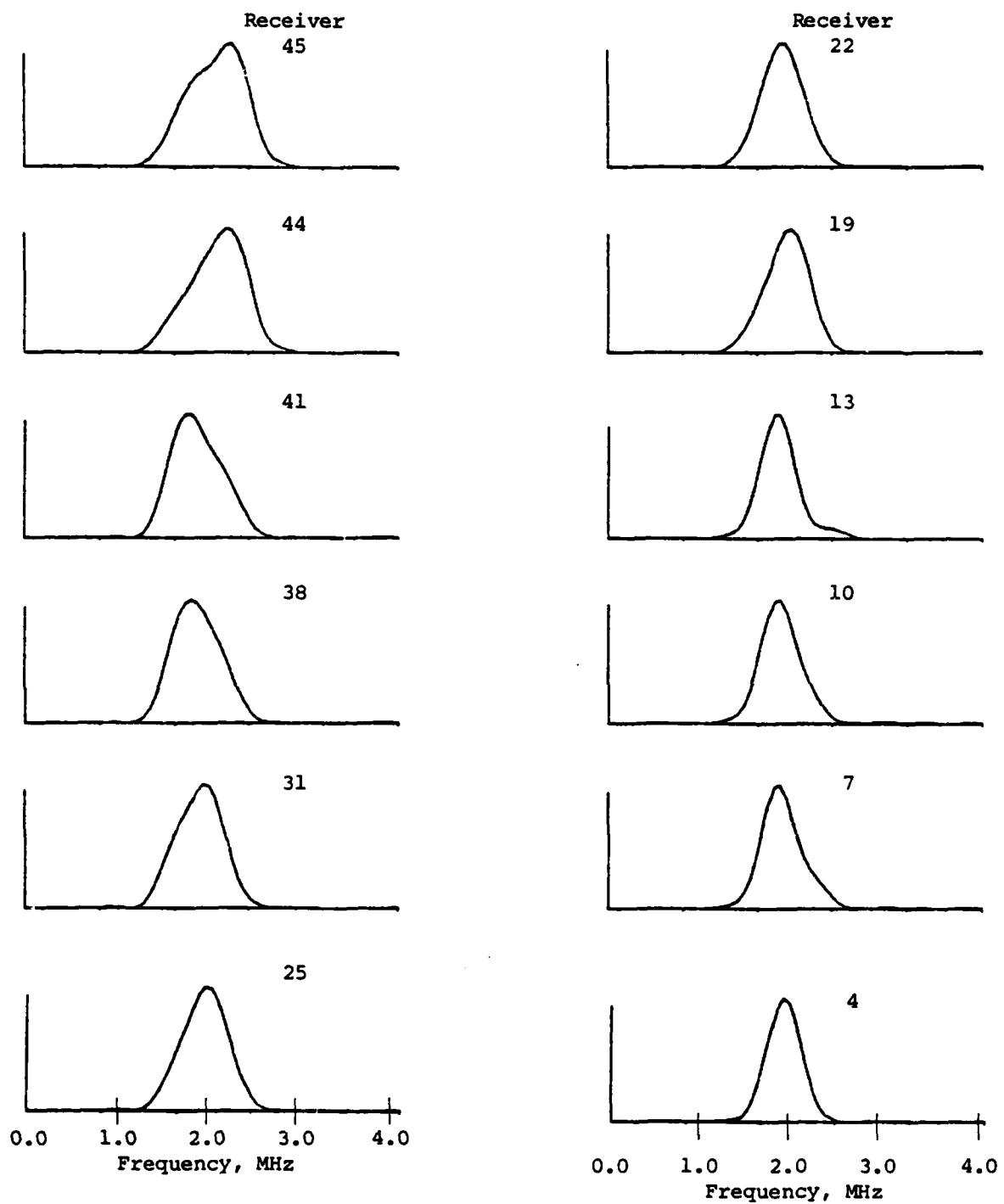
FIGURE 2.9: POWER SPECTRA CALCULATED FROM WAVEFORMS RECORDED DURING THE ARRAY RESPONSE TESTS (Spectra are all normalized to unity)

2-14

proceed knowing that the receivers are uniform and, therefore, differences in the recorded waveforms can be attributed principally to physical processes rather than to differing receiver characteristics.

2.4 ARRAY CONTROLLER

A custom controller interface was designed and fabricated by BNW to provide programmable control over the array package. This controller is linked to the ALN 4000 system by means of a serial RS-232 data port. Commands are sent over this link by the ALN 4000 to the controller and echoed back for confirmation. These commands serve to select the array, attenuator settings, and pulser. The controller accepts ASCII-coded data, reformats the code into binary form, and sends the command to the appropriate subfunction for interpretation. Initialization of the array is accomplished by an 8-bit command used to select one of the possible 47 receivers.

The receive decoder is composed of four identical 1-of-16 subdecoders which are each linked to 16 individual elements. All four subdecoders have inhibit features which guarantee that only one receiver is operational at any given time.   The 1-to-47 decoder is used to control an RF mechanical relay which couples the selected array receive element to an onboard, low-noise preamplifier.   The preamplifier is broadband (1-10 MHz) and has a gain of approximately 50 volts.

The array controller also provides a means for connecting the high-voltage spike transmit pulse to either the inboard or outboard array.   The received

ultrasonic signal is then preamplified and input to a programmable attenuator. This feature is required to prevent saturation of the analog-to-digital conversion in the ALN 4000. This attenuator can be set in 1-dB steps over the range from 1 to 31 dB.

The received signal is sent from the attenuator to the S-80 Reflectoscope system which is used for postamplification and signal display. The RF waveform is then transmitted to the ALN 4000. A photograph of the array controller and array package is shown in Figure 2.10.

2.5 ALN 4000

The ALN 4000 Multi Purpose Processing System designed and fabricated by Adaptronics is a programmable transient data acquisition and analysis instrument which can obtain digital data in either laboratory or field environments. Dual microprocessor electronics are provided with an 8-bit analog-to-digital converter having software-selectable sampling, with up to 4096 samples per transient being recorded at rates between 156 kHz and 20 MHz. The ALN 4000 includes separate microprocessor units for control of data acquisition and for high-speed data processing. A powerful processing architecture is used to eliminate recordings of unneeded data and preserve only significant events for later recall. A hand-held keyboard with alphanumeric display (or other ASCII terminal) allows easy interaction between the user and the ALN 4000 system. A built-in 18-column alphanumeric printer is used for instruction verification and data tabulation. Data are stored on dual digital tape cartridges with a capacity of 150 kilobytes per tape. These tape cartridges can be read locally
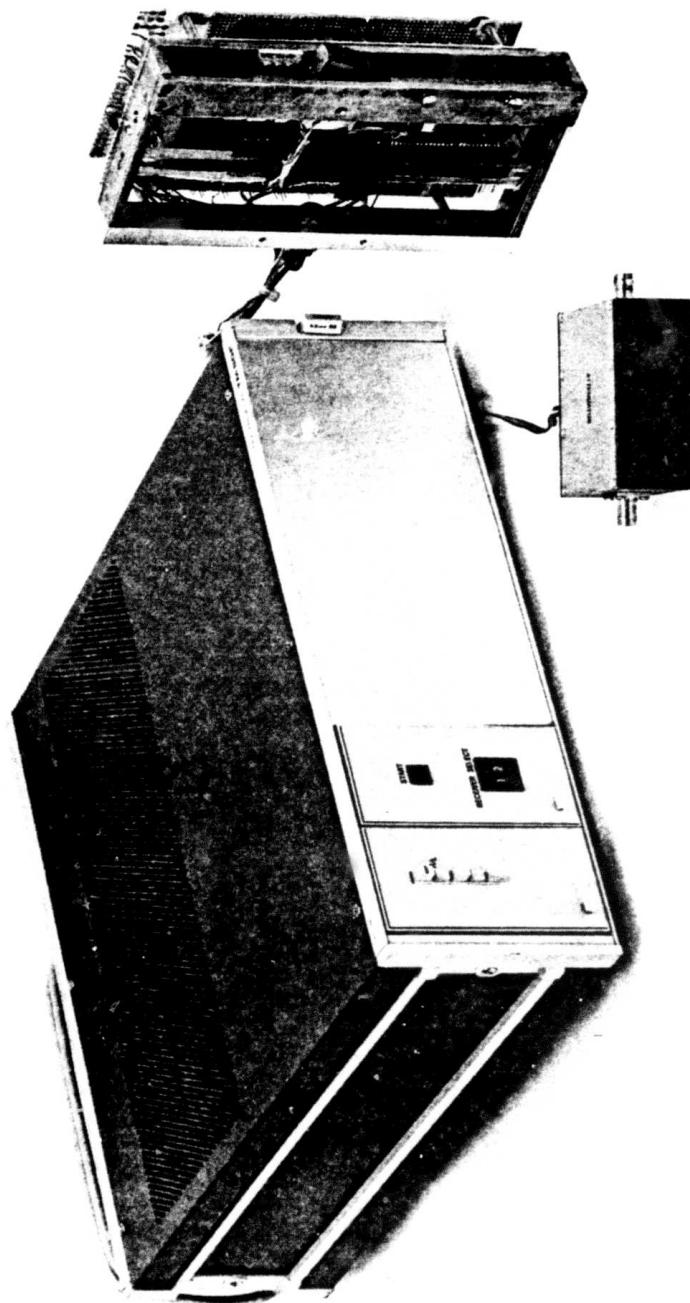
FIGURE 2.10: PHOTOGRAPH OF THE MICROPROCESSOR CONTROLLER, THE PROGRAMMABLE ATTENUATOR, AND THE ARRAY HEAD

or transferred to other computer systems by means of an RS-232C communications link. The ALN 4000 is a portable instrument and is contained in two enclosures as shown in Figure 2.11.

The ALN 4000 used in this program provided the overall supervisory function for the entire data collection process. Communication between the ALN 4000 and other subsystem components was accomplished through microprocessor software routines resident in the ALN 4000. Special-purpose software for signal detection, temporal beamforming, and other signal processing algorithms were programmed and installed in the ALN 4000 to assist the data analysis and interpretation phases of this program. These software algorithms will be described in subsequent sections of this report.

The chapter which follows presents a detailed description of how the ALN 4000 was used to collect ultrasonic signals from various defect types, sizes, and orientations.
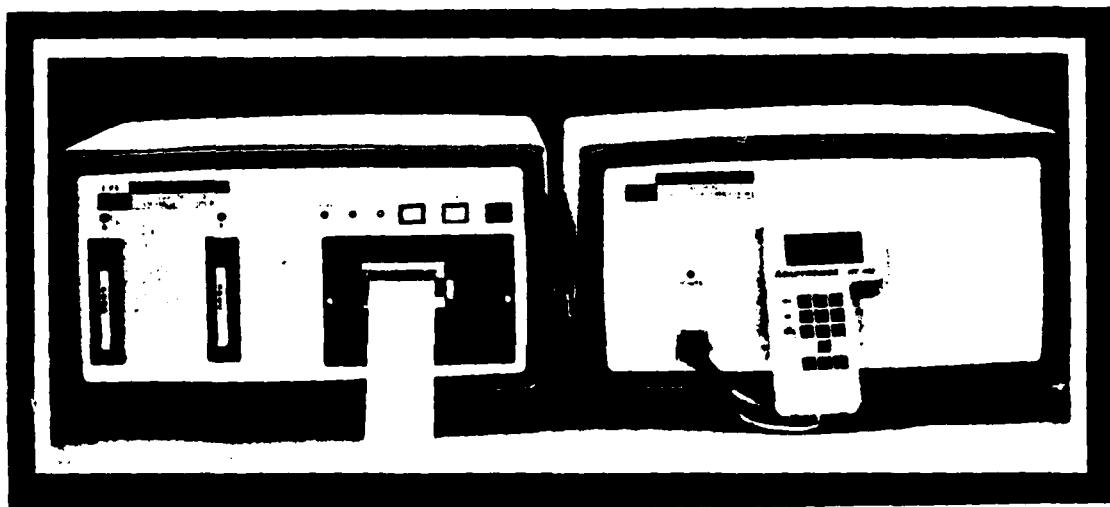
FIGURE 2.11: PHOTOGRAPH OF THE ALN 4000 SYSTEM

3. DATA COLLECTION PROCESS

3.1 INTRODUCTION

The data acquisition system described in the previous chapter was used to collect ultrasonic signals from a set of fabricated defect specimens. The characteristics of these defects as well as the procedures employed in the data collection exercises are described in this chapter.

3.2 DEFECT CHARACTERISTICS

Three types of machined defects were selected for analysis in this study: EDM notches, flat-bottom holes, and round-bottom holes. These categories were chosen because they were felt to be representative of real flaws encountered in actual field applications. A total of 16 different sizes and two angular orientations were fabricated for each flaw grouping.

The characteristics of the flat-bottom hole specimens are presented in Table 3.1. Each hole was drilled from the back of the metal block to a depth of approximately 0.5 inch. The diameters of the flat-bottom holes listed in this table represent the nominal sizes of the drills used in the fabrication process. The actual diameters determined from rubber replications deviate from these design values by a few mils. The diameters considered in this investigation range from 1/64 inch to 16/64 inch at 1/64 inch increments. The artificial flaws were drilled at orientations of 0° and 30° with respect to the vertical. A schematic diagram of the defect locations and sizes is shown in Figure 3.1 for the 0° flat-bottom holes and in Figure 3.2 for the 30° specimens.

TABLE 3.1: CHARACTERISTICS OF THE FLAT-BOTTOM HOLE DEFECTS

	Flaw #	FBH Diameter	Angle		Flaw #	FBH Diameter	Angle
Block 2A	1	.016 inch	0°	Block 3A	17	.016 inch	30°
	2	.031	0		18	.031	30
	3	.047	0		19	.047	30
	4	.063	0		20	.063	30
	5	.078	0		21	.078	30
	6	.094	0		22	.094	30
	7	.109	0		23	.109	30
	8	.125	0		24	.125	30

	Flaw #	FBH Diameter	Angle		Flaw #	FBH Diameter	Angle
Block 2B	9	.141 inch	0°	Block 3B	25	.141 inch	30°
	10	.156	0		26	.156	30
	11	.172	0		27	.172	30
	12	.188	0		28	.188	30
	13	.203	0		29	.203	30
	14	.219	0		30	.219	30
	15	.234	0		31	.234	30
	16	.250	0		32	.250	30
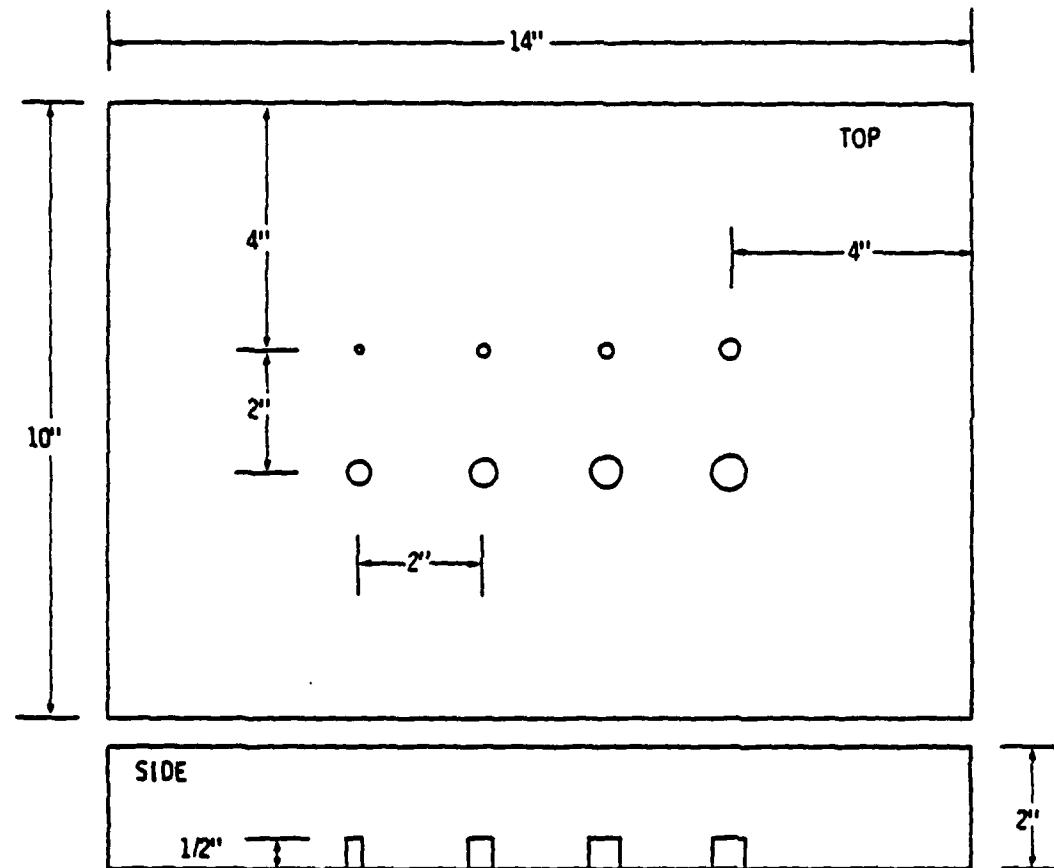
BLOCKS 2A, 2B

FLAT BOTTOM HOLES, NORMAL TO SURFACE

HOLE DIAMETERS IN 1/64":

BLOCK 2A: 1, 2, 3, 4, 5, 6, 7, 8
BLOCK 2B: 9, 10, 11, 12, 13, 14, 15, 16

FIGURE 3.1:   DIAGRAM OF TEST BLOCKS 2A and 2B CONTAINING 0° FLAT-
BOTTOM HOLES
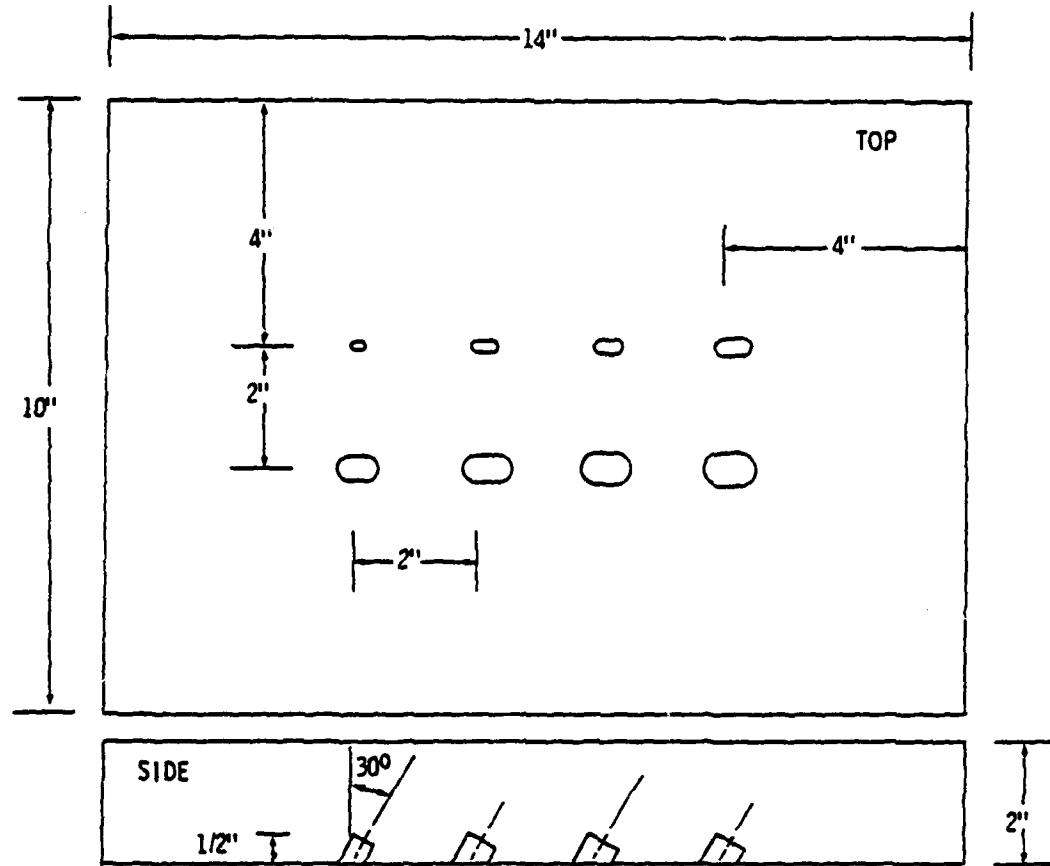
BLOCKS 3A, 3B

FLAT BOTTOM HOLES 30° FROM NORMAL TO THE SURFACE

HOLE DIAMETERS IN 1/64":

BLOCK 3A: 1, 2, 3, 4, 5, 6, 7, 8
BLOCK 3B: 9, 10, 11, 12, 13, 14, 15, 16

FIGURE 3.2: DIAGRAM OF TEST BLOCKS 3A and 3B CONTAINING 30° FLAT-BOTTOM HOLES

The characteristics of the round-bottom hole samples are summarized in Table 3.2. The range in size is the same as that discussed for the flat-bottom holes. The process used in fabrication of the round-bottom hole flaws involved the use of spheroidal dental burrs to obtain hemispherical reflectors. The actual diameters measured from rubber replications indicate a variation of a few mils from the nominal values listed in Table 3.2. It should also be noted that the dental burrs used in the fabrication process did not provide a smooth hemispherical surface, especially for the smaller diameter holes. The round-bottom holes were drilled at angles of 0° and 30° from the normal to the surface. Diagrams of the 0° holes are presented in Figure 3.3 and in Figure 3.4 for the 30° holes.

The lengths and depths of the EDM notch samples are identified in Table 3.3. In the case of the notch defects, two length-to-depth ratios were obtained (3:1 and 5:1). The depth values vary from 10 mils to 80 mils at 10 mil increments. The actual dimensions obtained from the replicas differ from the specified values by ±2 mils in depth and ±5 mils in length. The actual widths of the EDM notch specimens are on the order of a few mils. The schematic representations of the 0° notches and the 30° notches are shown in Figures 3.5 and 3.6, respectively.

Each of the 96 defects described above was machined in test blocks of aircraft quality 4340 steel plate. C-scan images were obtained from each of the 12 test blocks to determine the level of acoustic background reflectors. These tests were performed using a 5 MHz transducer with a focal length on the order of four inches. A 3/64 inch flat-bottom hole ASTM test block was used as a

TABLE 3.2: CHARACTERISTICS OF THE ROUND-BOTTOM HOLE DEFECTS

	Flaw #	RBH Diameter	Angle		Flaw #	RBH Diameter	Angle
Block 4A	33	.016 inch	0°	Block 5A	49	.016 inch	30°
	34	.031	0		50	.031	30
	35	.047	0		51	.047	30
	36	.063	0		52	.063	30
	37	.083	0		53	.083	30
	38	.098	0		54	.098	30
	39	.109	0		55	.109	30
	40	.128	0		56	.128	30

	Flaw #	RBH Diameter	Angle		Flaw #	RBH Diameter	Angle
Block 4B	41	.142 inch	0°	Block 5B	57	.150 inch	30°
	42	.158	0		58	.158	30
	43	.177	0		59	.177	30
	44	.189	0		60	.187	30
	45	.202	0		61	.206	30
	46	.224	0		62	.224	30
	47	.239	0		63	.234	30
	48	.287	0		64	.287	30
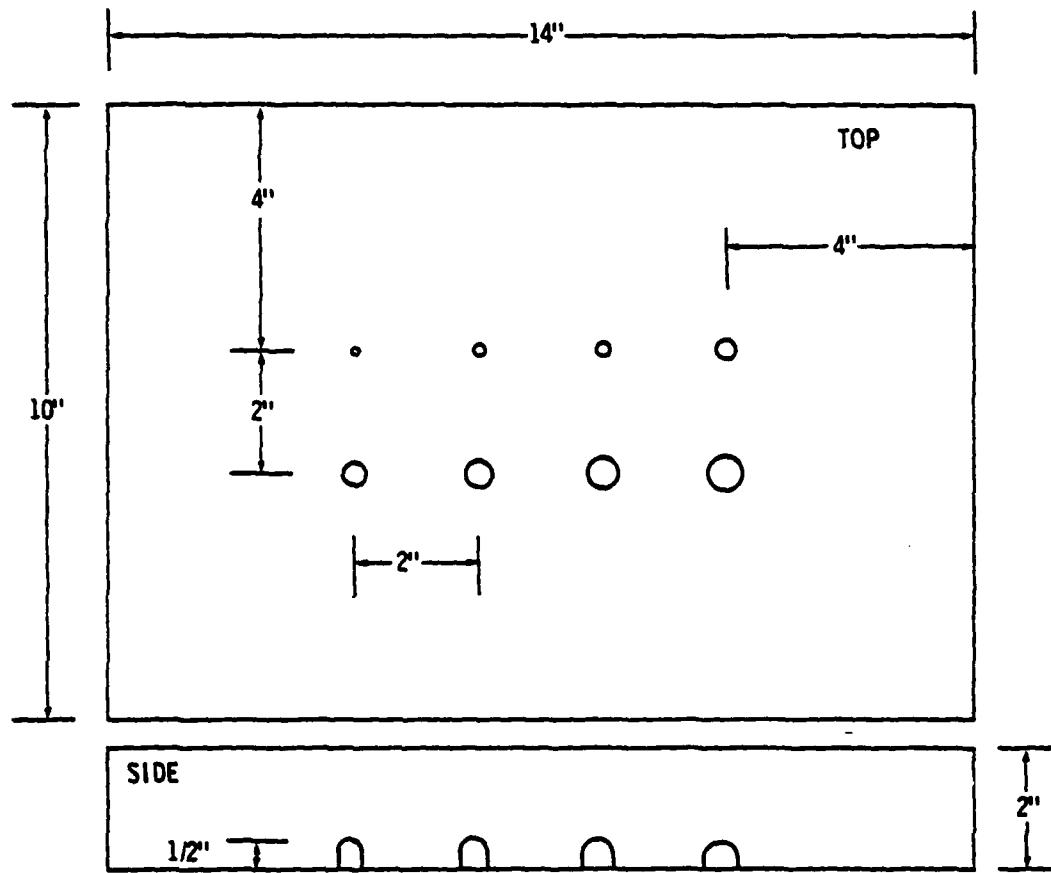
BLOCKS 4A, 4B

ROUND BOTTOM HOLES, NORMAL TO THE SURFACE

HOLE DIAMETERS IN 1/64":

BLOCK 4A: 1, 2, 3, 4, 5, 6, 7, 8
BLOCK 4B: 9, 10, 11, 12, 13, 14, 15, 16

FIGURE 3.3: DIAGRAM OF TEST BLOCKS 4A and 4B CONTAINING 0° ROUND-BOTTOM HOLES
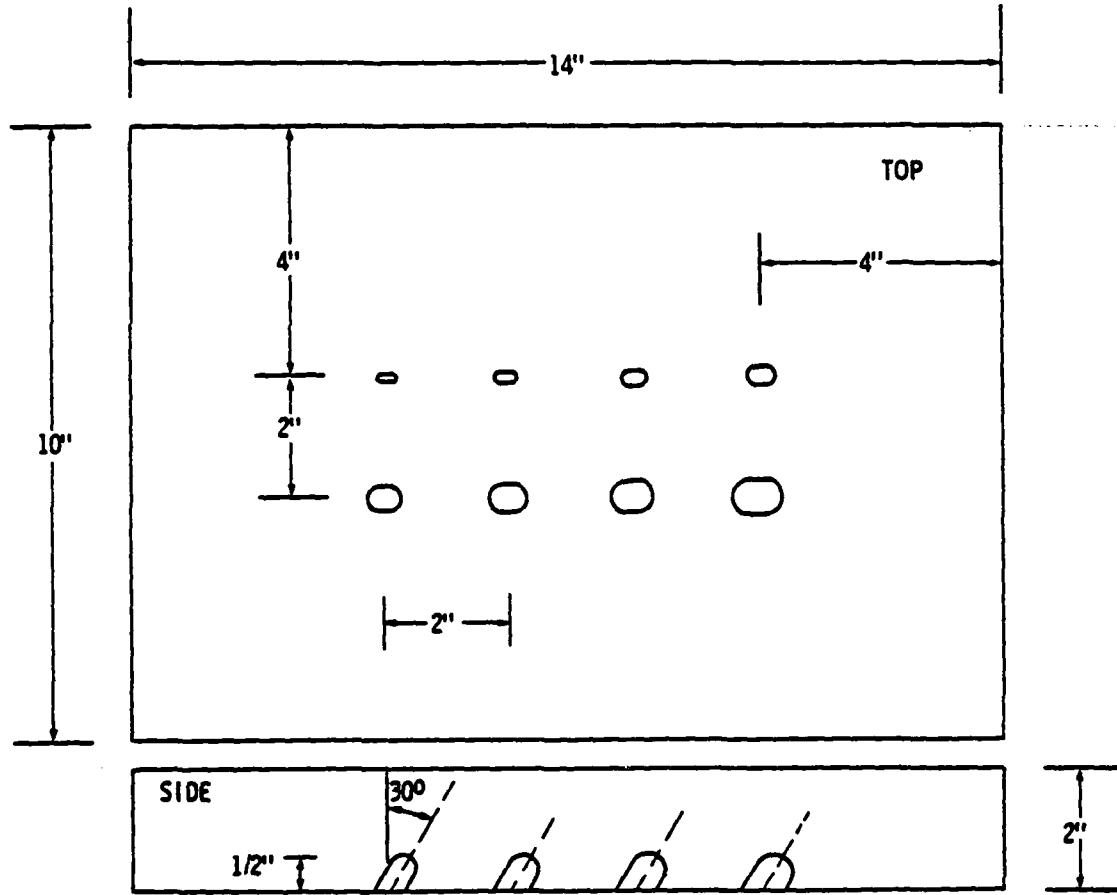
BLOCKS 5A, 5B

ROUND BOTTOM HOLES, 30° FROM NORMAL TO THE SURFACE

HOLE DIAMETERS IN 1/64":

BLOCK 5A: 1, 2, 3, 4, 5, 6, 7, 8
BLOCK 5B: 9, 10, 11, 12, 13, 14, 15, 16

FIGURE 3.4: DIAGRAM OF TEST BLOCKS 5A and 5B CONTAINING 30° ROUND-BOTTOM HOLES

TABLE 3.3: CHARACTERISTICS OF THE EDM NOTCH DEFECTS

	Flaw #	Angle	EDM Dimension*		Flaw #	Angle	EDM Dimension*
Block 6A	65	0°	10 x 30	Block 7A	81	30°	10 x 30
	66	0	20 x 60		82	30	20 x 60
	67	0	30 x 90		83	30	30 x 90
	68	0	40 x 120		84	30	40 x 120
	69	0	50 x 150		85	30	50 x 150
	70	0	60 x 180		86	30	60 x 180
	71	0	70 x 210		87	30	70 x 210
	72	0	80 x 240		88	30	80 x 240

	Flaw #	Angle	EDM Dimension*		Flaw #	Angle	EDM Dimension*
Block 6B	73	0°	10 x 50	Block 7B	89	30°	10 x 50
	74	0	20 x 100		90	30	20 x 100
	75	0	30 x 150		91	30	30 x 150
	76	0	40 x 200		92	30	40 x 200
	77	0	50 x 250		93	30	50 x 250
	78	0	60 x 300		94	30	60 x 300
	79	0	70 x 350		95	30	70 x 350
	80	0	80 x 400		96	30	80 x 400

*Dimensions represent DEPTH x LENGTH IN 10^{-3} INCHES.

BLOCKS 6A, 6B

EDM NOTCHES, NORMAL TO THE SURFACE, 0.010"WIDE

NOTCH DEPTHS:

0.010", 0.020", 0.030", 0.040", 0.050", 0.060", 0.070", 0.080

BLOCK 6A: LENGTH TO DEPTH RATIO IS 3:1
BLOCK 6B: LENGTH TO DEPTH RATIO IS 5:1
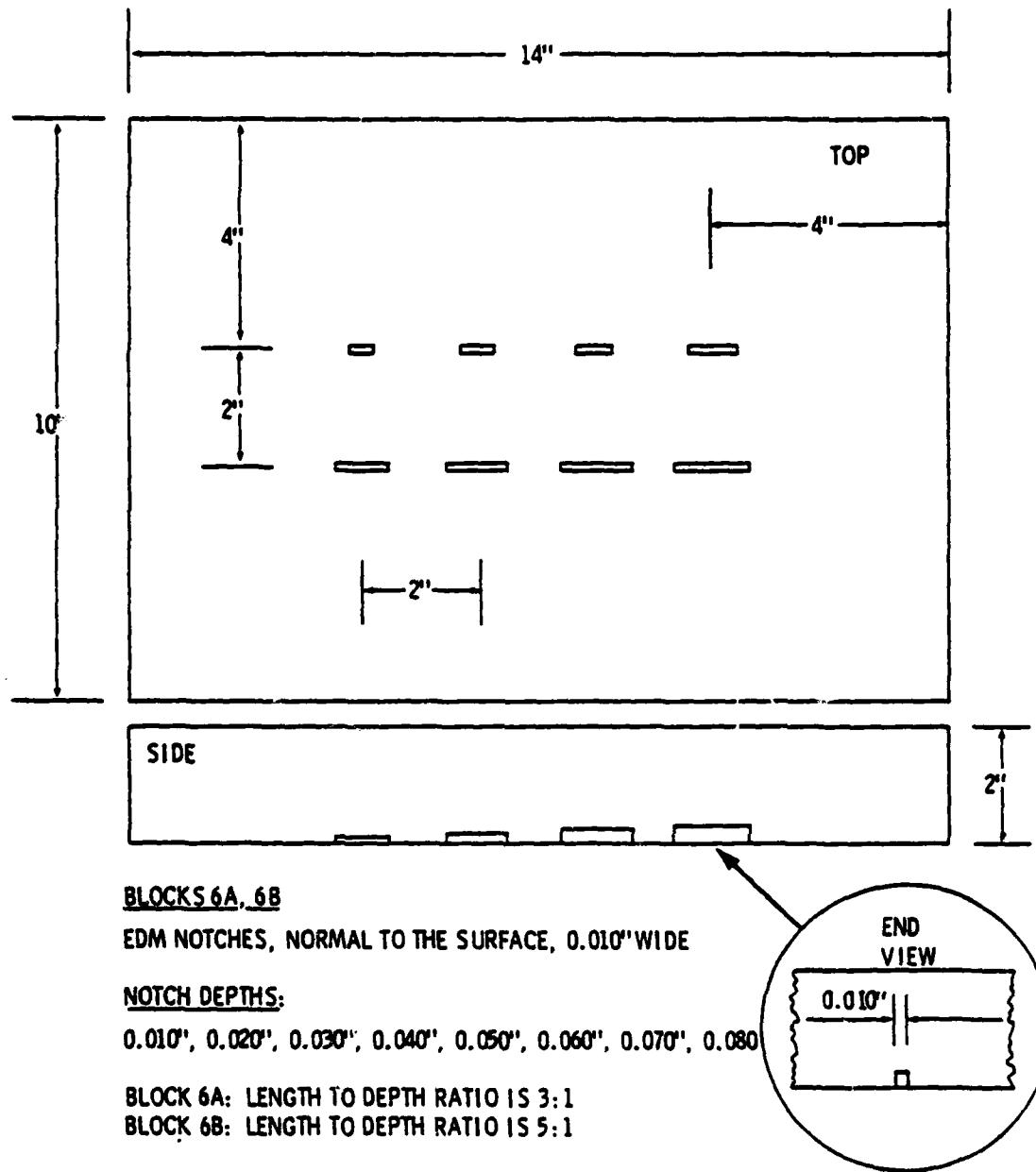
FIGURE 3.5: DIAGRAM OF TEST BLOCKS 6A and 6B CONTAINING 0° EDM
            NOTCHES

3-10
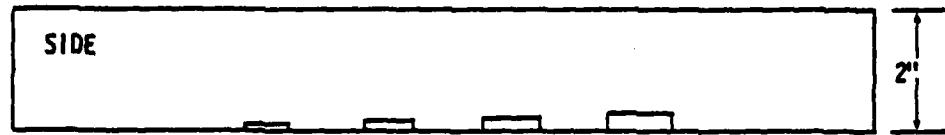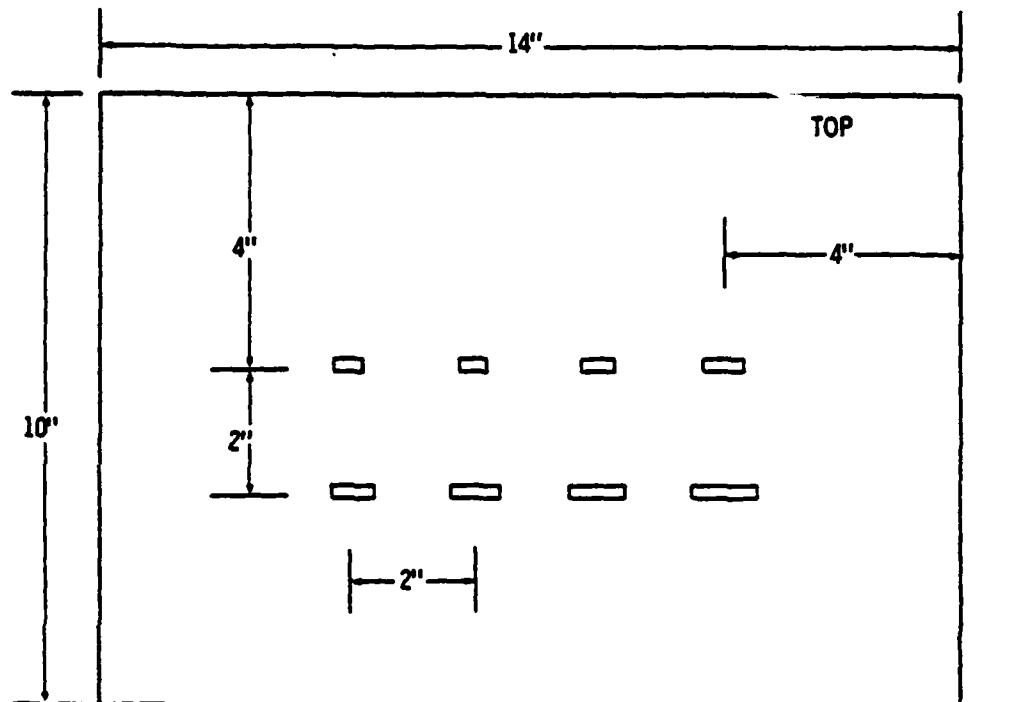
BLOCKS 7A, 7B

EDM NOTCHES, $30°$ FROM NORMAL TO THE SURFACE, 0.010" WIDE.

NOTCH DEPTHS:

0.010", 0.020", 0.030", 0.040", 0.050", 0.060", 0.070", 0.080"

BLOCK 7A: LENGTH TO DEPTH RATIO IS 3:1
BLOCK 7B: LENGTH TO DEPTH RATIO IS 5:1
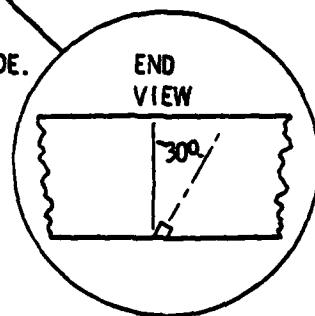
FIGURE 3.6: DIAGRAM OF TEST BLOCKS 7A and 7B CONTAINING 30°
EDM NOTCHES

reference reflector. The majority of the 4340 test blocks have nondefect-related reflectors that are generally below the amplitude level obtained from the reference 3/64 inch diameter flat-bottom hole.

A typical C-scan display representing block 5B is shown in Figure 3.7. This block contains a set of 30° round-bottom hole defects of diameters from 9/64 inch to 16/64 inch. It is obvious from this illustration that the intrinsic reflectors all lie well above the reference threshold. In addition, it can be seen that the C-scan image also correlates well with the actual round-bottom hole diameters.

However, in a few cases, the C-scan images presented a much more cluttered picture. An example is shown in Figure 3.8, which represents the scan of test block 4A (0° round-bottom holes of diameters 1/64 inch to 8/64 inch). The write level used in this illustration was set 3 dB below the amplitude of the 3/64 inch diameter round-bottom hole in the block. At this sensitivity, the background reflectors are clearly visible and mask the smaller diameter round-bottom hole reflectors. This observation is typical of the 4340 rolled plate steel and most likely represents precipitates of the alloying elements used to provide increased strength and hardness to the material.

Referring again to Figure 3.8, it should be noted that the round-bottom hole sizes inferred from the C-scan do not increase monotonically with actual diameter measurements. The reason for this anomaly is related to the observation made earlier concerning the roughness of the hemispherical shapes. Visual inspection of the replicas of this block indicates that small flat zones and other anomalies are present which tend to distort the acoustic echo
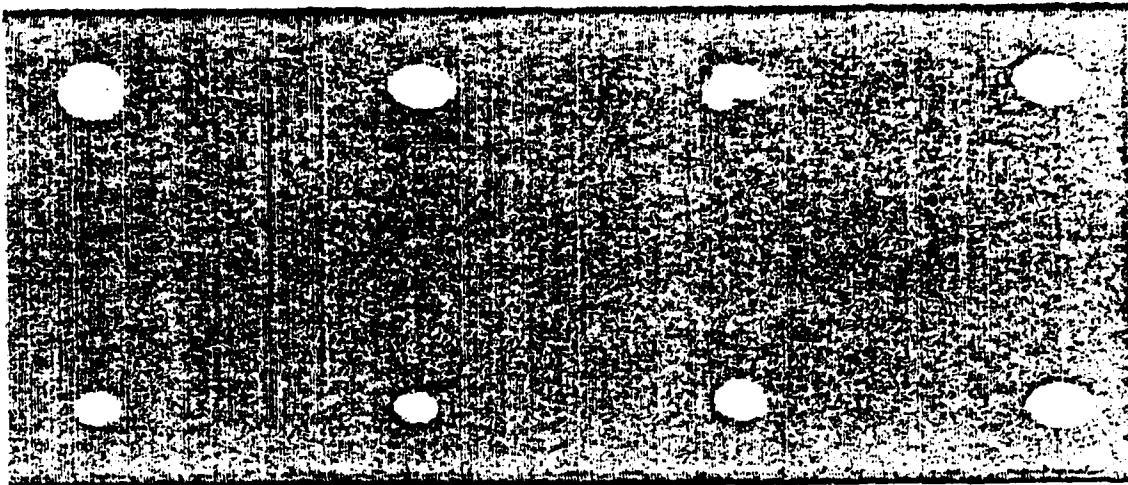
FIGURE 3.7: C-SCAN OF TEST BLOCK 5B (#9-16 RBH, 30° Orientation) USING A
5.0 MHz TRANSDUCER WITH A 4.0 INCH FOCAL LENGTH
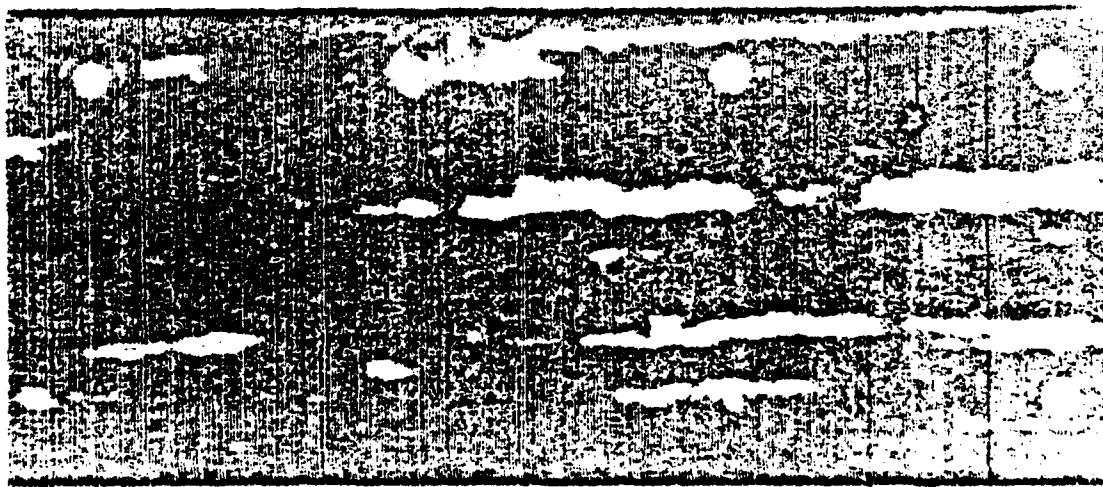
FIGURE 3.8: C-SCAN OF TEST BLOCK 4A, (#1-8 RBH, 0° Orientation) USING A
5.0 MHz, 2.0 INCH FOCAL LENGTH TRANSDUCER. WRITE LEVEL WAS
3 dB BELOW THE AMPLITUDE OF THE 3/64 INCH RBH REFLECTION

reflections. The implications of this observation are addressed in more detail in the signal analysis portions of this report.

The 12 test blocks containing the 96 defects described in this section were used in collecting ultrasonic waveforms that were subsequently analyzed for defect characterization purposes. The section which follows describes the procedures employed in collecting waveforms from these defect specimens.

3.3 DATA COLLECTION PROCEDURES

The data acquisition system discussed in Chapter 2 was used to collect ultrasonic signals from the defect specimens in the various test blocks. The key components of the system with regard to the data collection effort were the ultrasonic array, the transmitter/receiver controller, the scanner, and the ALN 4000. Each of these components has been previously described. In this section the use of these various subsystems in the actual data collection exercises is outlined and discussed.

The purpose of the linear ultrasonic array was to allow the reflected, diffracted, and mode-converted energy to be obtained over a wide aperture for use in the defect characterization tasks. To maintain this philosophy, two general methods were utilized in the data collection, depending on the type and orientation of the defect under study. The 0° flat-bottom and round-bottom holes were insonified using the inboard transmitter (TI). The ultrasonic signals recorded from the angled holes and both the 0° and 30° EDM notches were obtained using the outboard transmitter (TO). The reasoning

behind these procedures was mainly a result of the geometrical properties of the defects in question. A better physical description of the geometrical influence is illustrated schematically in Figure 3.9 for the 0° hole case and in Figure 3.10 for the 0° EDM notch case. Examination of the 0° hole representation of Figure 3.9 illustrates that the main back reflections are concentrated near the inboard transmitter while the diffracted energy is scattered to other regions in the linear array. The EDM notch example depicted in Figure 3.10 shows that the main reflections are directed back toward the outboard transmitter, because of the strong corner reflections generated by the back surface of the test block. The diffracted signals from the crack tip are scattered to other receivers located within the inboard linear array. It can also be shown that the angled hole and notch defects would exhibit radiation patterns similar to those presented in Figure 3.10. The consideration of these geometrical properties influenced the procedures used in collecting data on the ultrasonic fields radiated from the various defect types and orientations.

The first step in the data collection process involved selection of the appropriate transmitter for defect insonification. As noted above, this decision was made on the basis of the defect type and its angular orientation. For 0° hole defects, the inboard transmitter/receiver was selected. In all other cases, the outboard transmitter/receiver was used. After the appropriate transmitter/receiver had been designated, the operator proceeded to move the X-Y scanner around the flaw of interest and located the position at which the amplitude of the echo was a maximum. The pulse-echo recording was then digitized by the ALN 4000 and written to a tape cartridge along with other appropriate information (defect number, attenuator settings, etc.). The
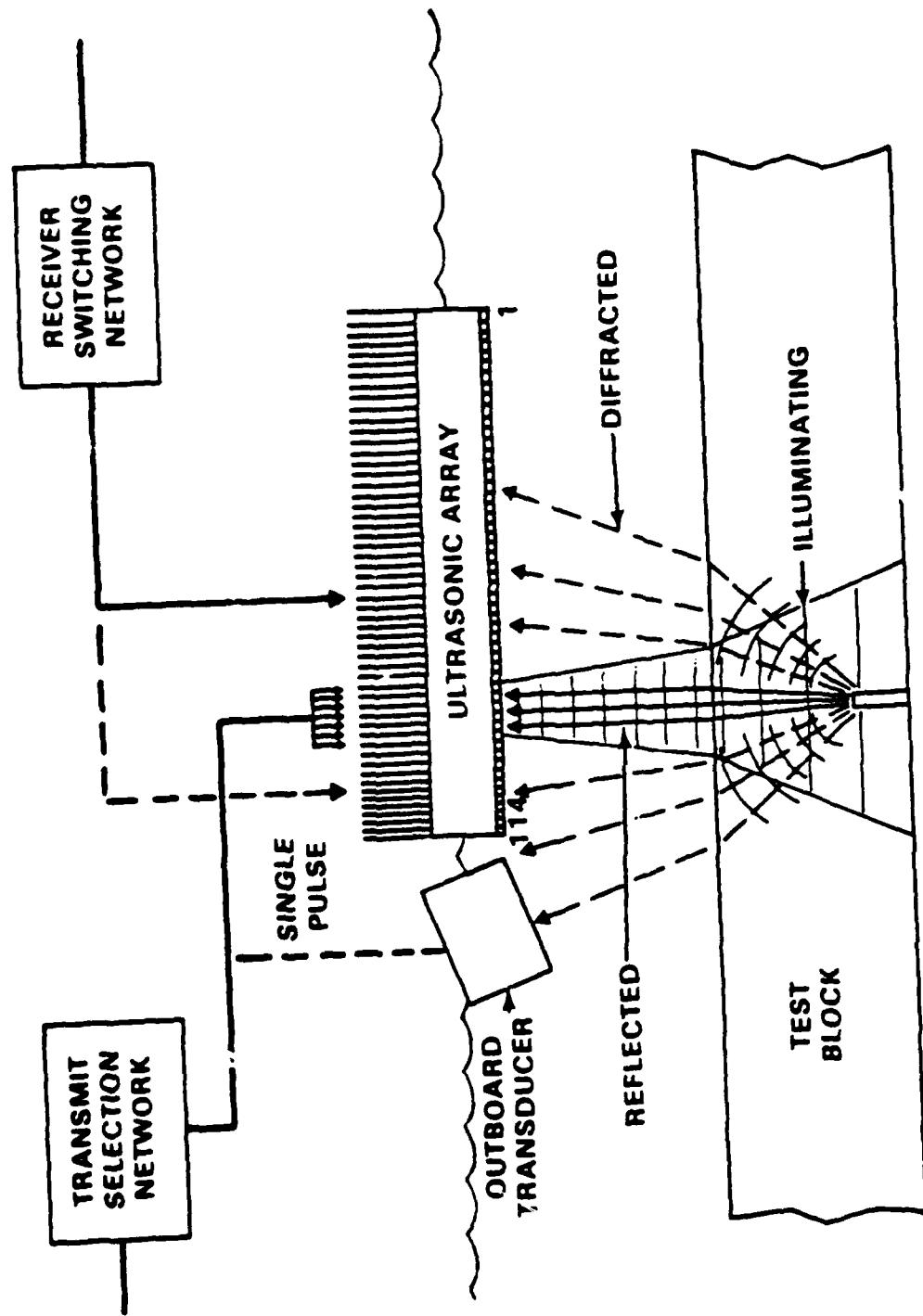
FIGURE 3.9: ILLUSTRATION OF NORMAL BEAM INSONIFICATION OF A FLAT-BOTTOM HOLE AND DETECTION OF REFLECTED AND DIFFRACTED ENERGY USING A LINEAR ARRAY
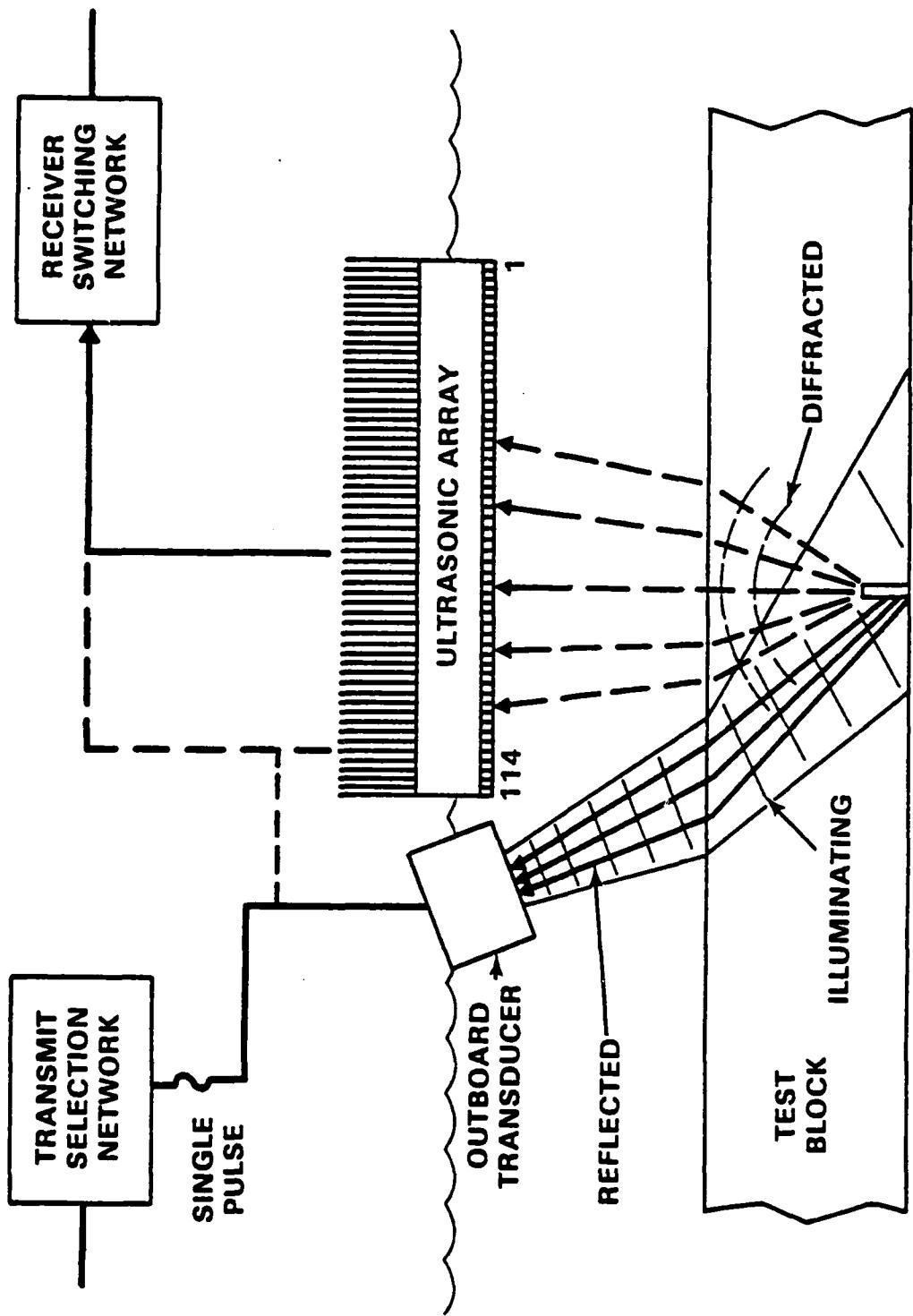
FIGURE 3.10: ILLUSTRATION OF AN ANGLE BEAM INSPECTION OF AN EDM NOTCH AND DETECTION OF THE REFLECTED AND DIFFRACTED ENERGY

operator could then request that recordings be obtained at other receiver positions within the array. At his command, these additional recordings were also digitized and written on the tape cartridges. The X-Y scanner was not repositioned during these operations, since any movement would alter the transmitter/receiver geometry and hence the diffracted field. At the completion of the data collection exercises, the tape cartridges were transferred to an off-line Data General Eclipse computer system, where the digital waveforms were decoded, reformatted, and written to a standard 9-track tape for further detailed analyses. A block diagram representation of the data collection process is shown in Figure 3.11, which identifies the decisions and procedures involved in this task. In general, a total of 20 waveforms was collected for each of the 96 individual defects considered in this study.

The individual waveforms were digitized at a rate of 20 points per microsecond to obtain a total recording of 1024 points, which represented a time duration of 51.2 microseconds. This digitization rate yielded approximately eight points per cycle at the center frequency of the transducer. The time duration was sufficient to allow the digitization to begin at the arrival of the front surface reflection from the test block and to continue until the defect response returned to the receiver location. Examples of ultrasonic data collected from the various defect types are presented and discussed in more detail in the chapter which follows.
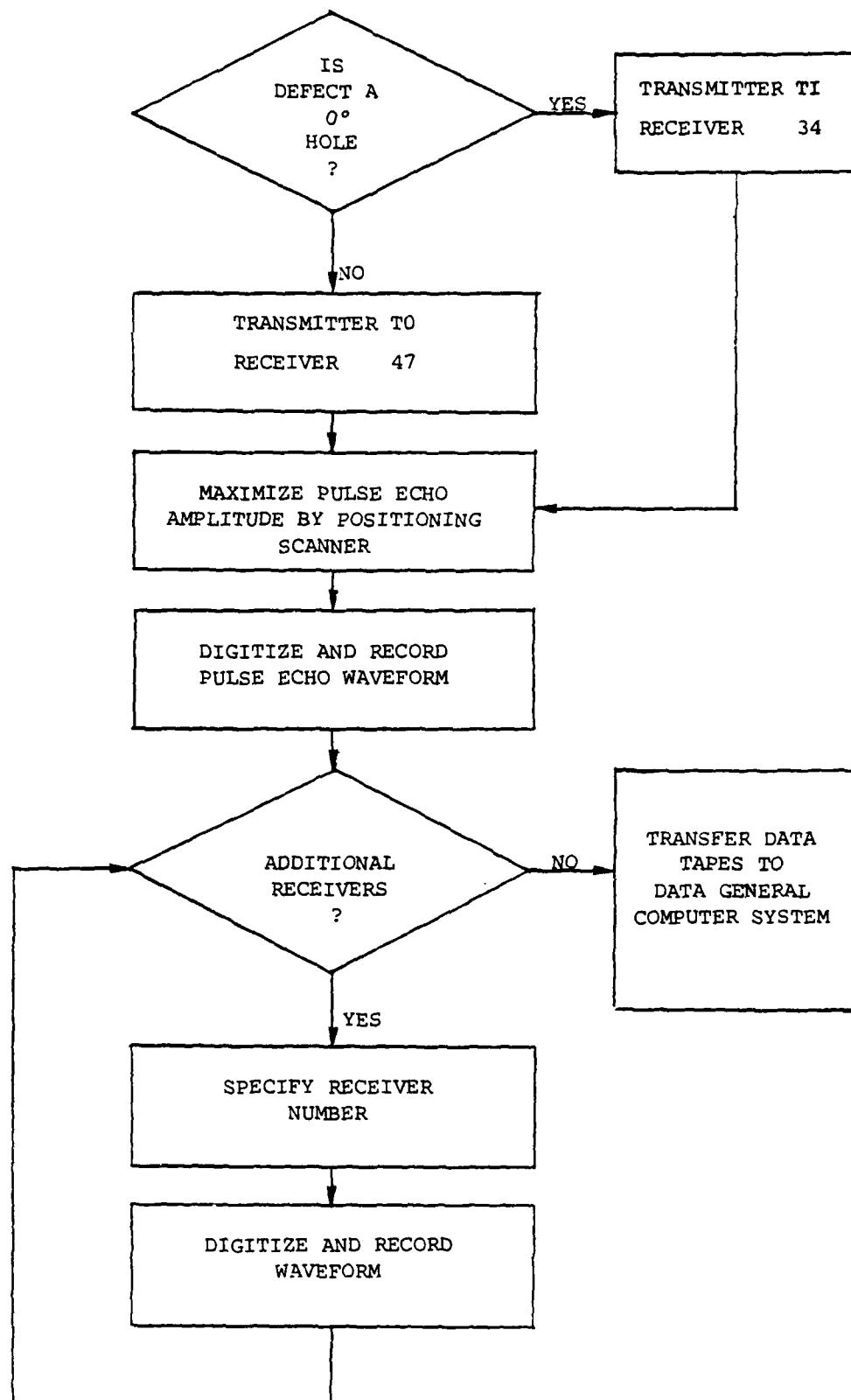
FIGURE 3.11: BLOCK DIAGRAM ILLUSTRATION OF DATA COLLECTION
PROCEDURES

3-19

4. DETECTION OF DEFECT RESPONSE SIGNALS

4.1 INTRODUCTION

The ultrasonic waveforms collected from various defect types, sizes, and orientations were subjected to a wide variety of signal processing algorithms during the course of this project. These algorithms can be divided into two main categories, those used for signal enhancement purposes and those used in extracting features from the defect-related responses. The purpose of this chapter is to describe the procedures and techniques used in detecting and isolating the portions of the digitized waveforms which were related to the machined defects. The first topic of discussion in this chapter is concerned with developing the procedures used in separating responses due to geometrical reflectors from those related to the actual defects. Subsequent sections discuss the techniques employed to increase the signal-to-noise ratio of the recorded waveforms as well as the algorithm used in the signal detection exercise.

4.2 GEOMETRICAL CONSIDE　˙ONS

In most ultrasonic data collection exercises, the analyst is faced with the challenge of overcoming two major problem areas. The first involves the detection of signals in the presence of background noise. The second concerns the assignment of these detections into one of two categories, those related

to the geometry of the specimen being inspected and those related to defects in the test object. This second problem area will be addressed in this section by describing the procedures employed in this study for making the distinction between geometrical and defect-related responses.

The detection approach selected for use in this study involved the identification of an echo or signal recorded in the pulse-echo mode in which the array element acted as both a transmitter and a receiver. The ultrasonic array constructed for this investigation consisted of two transmitter/receiver (T/R) pairs, an outboard (TO) and an inboard (TI) T/R. The geometrical considerations associated with each T/R pair are quite different and are discussed separately below.

A schematic illustration of the test block and the outboard T/R is shown in Figure 4.1. The outboard transmitter emitted a compressional wave into the water bath at an angle of 16°. This propagating energy was converted into a shear wave at the water/metal interface. This shear wave entered the metal specimen at an angle of 36° from the vertical and propagated through the block. During this process, the shear wave encountered numerous interfaces where the energy was reflected, refracted, and diffracted. The reflected signals were recorded at the outboard receiver and then analyzed to determine which, if any, of the reflections were defect-related.

Examples of pulse-echo recordings obtained from specific defect types using the outboard transmitter/receiver are shown in Figure 4.2. Several large amplitude reflections can be seen on each of these individual recordings. The first large amplitude arrival on each waveform corresponds to the front
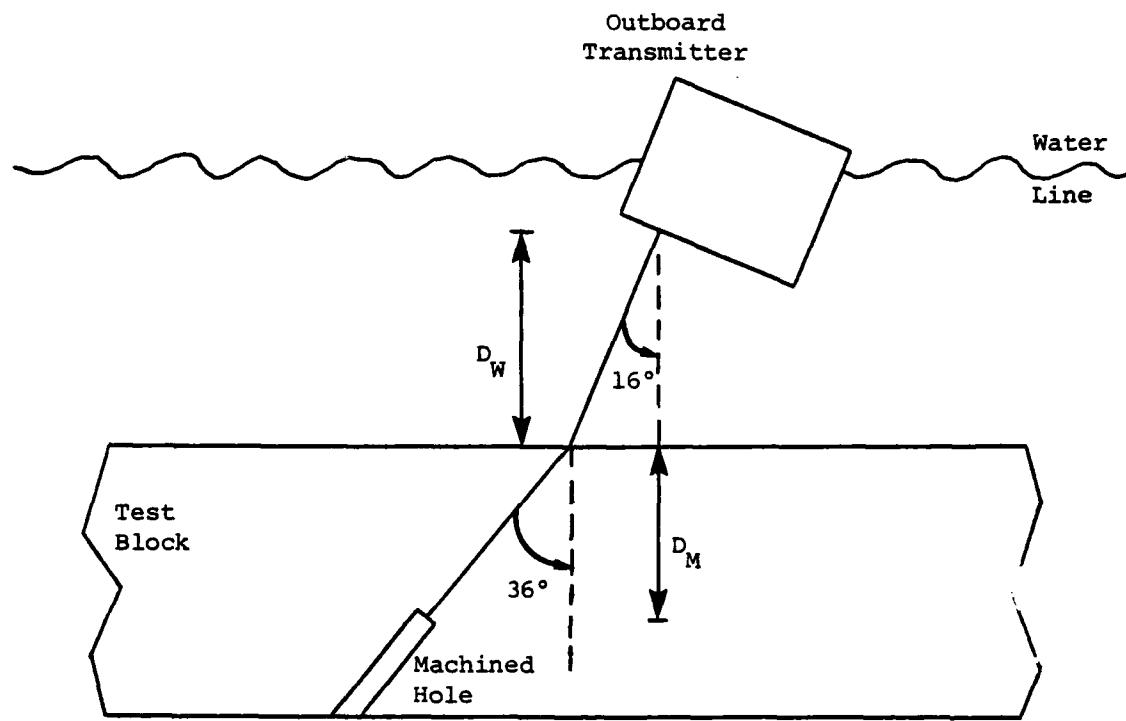
FIGURE 4.1: SCHEMATIC ILLUSTRATION OF THE OUTBOARD TRANSMITTER
AND TEST BLOCK GEOMETRY

30° FLAT-BOTTOM HOLE, 10/64"

FRONT SURFACE

DEFECT

30° ROUND-BOTTOM HOLE, 10/64"

30° EDM NOTCH 40x120 MILS

FRONT SURFACE

DEFECT

0° EDM NOTCH 80x240 MILS
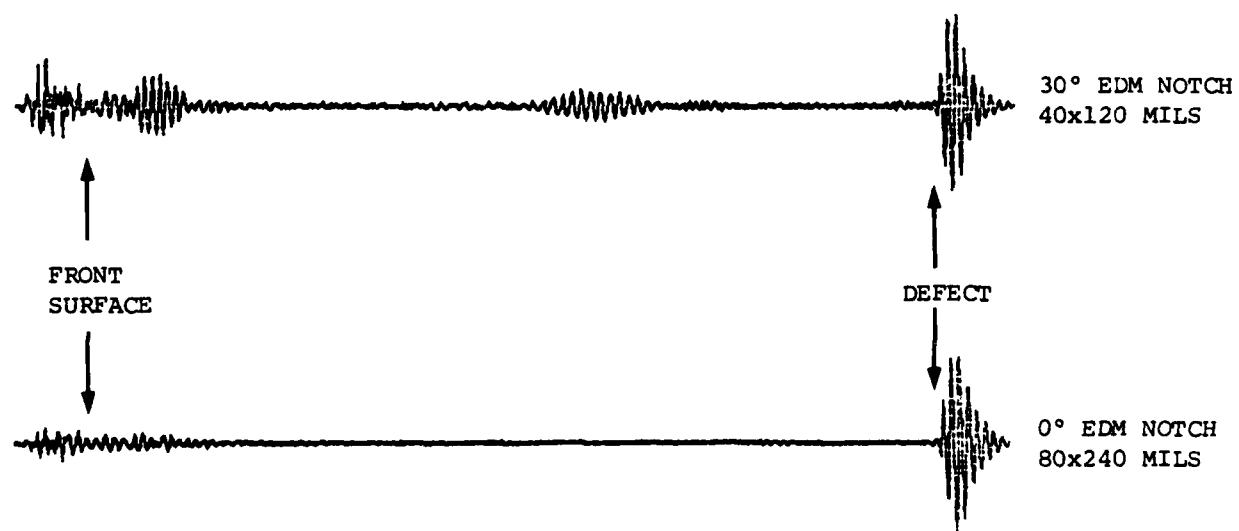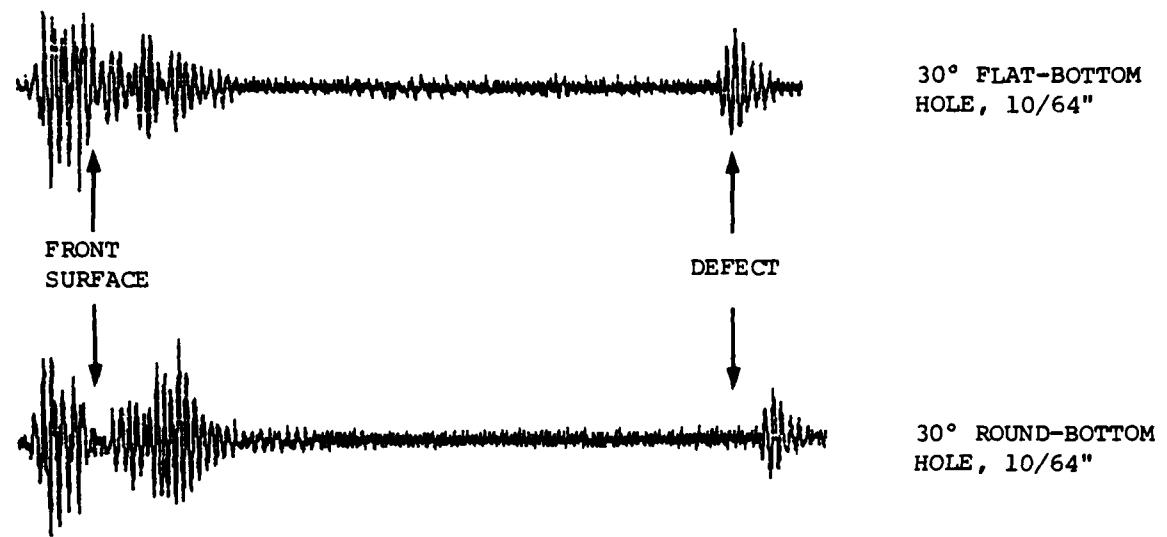
FIGURE 4.2:   EXAMPLES OF PULSE-ECHO RECORDINGS
OBTAINED FROM THE OUTBOARD ARRAY

surface reflection from the top of the test specimen. At first glance, it would appear that no direct reflection would be recorded because of the non-vertical incident angle of the transmitter; however, the angular response of the outboard transmitter shown in Figure 4.3 illustrates that a large amount of ultrasonic energy is emitted from the transducer which propagates vertically downward and is reflected directly back toward the transmitter. In fact, the detection of this first arrival allows the vertical distance between the transmitter and the top of the specimen to be calculated as:

$$D_W = \frac{T_W \cdot V_W}{2} \tag{4.1}$$

Where D_W is the vertical water depth, V_W is the velocity of sound in water (1.48 mm/μsec) and T_W is the arrival time of the front surface reflection relative to the transmit time. The other arrivals illustrated on the recordings shown in Figure 4.2 can be equated with a metal depth according to the relationship:

$$D_M = \frac{(T_M - T_W) \, V_M \cos \psi}{2} \tag{4.2}$$

where T_M is the time of the arrival in question, measured relative to the time the sound entered the metal, V_M is the shear wave velocity of sound in the metal (3.14 mm/μsec) and ψ is the angle of incidence (36°).

A direct comparison of the EDM notch arrival times with those of the angled hole specimens shown in Figure 4.2 indicates that the hole responses arrived earlier than those of the notch defects. This time difference is related to both the geometrical properties of the two reflector types and to the manner

4-5
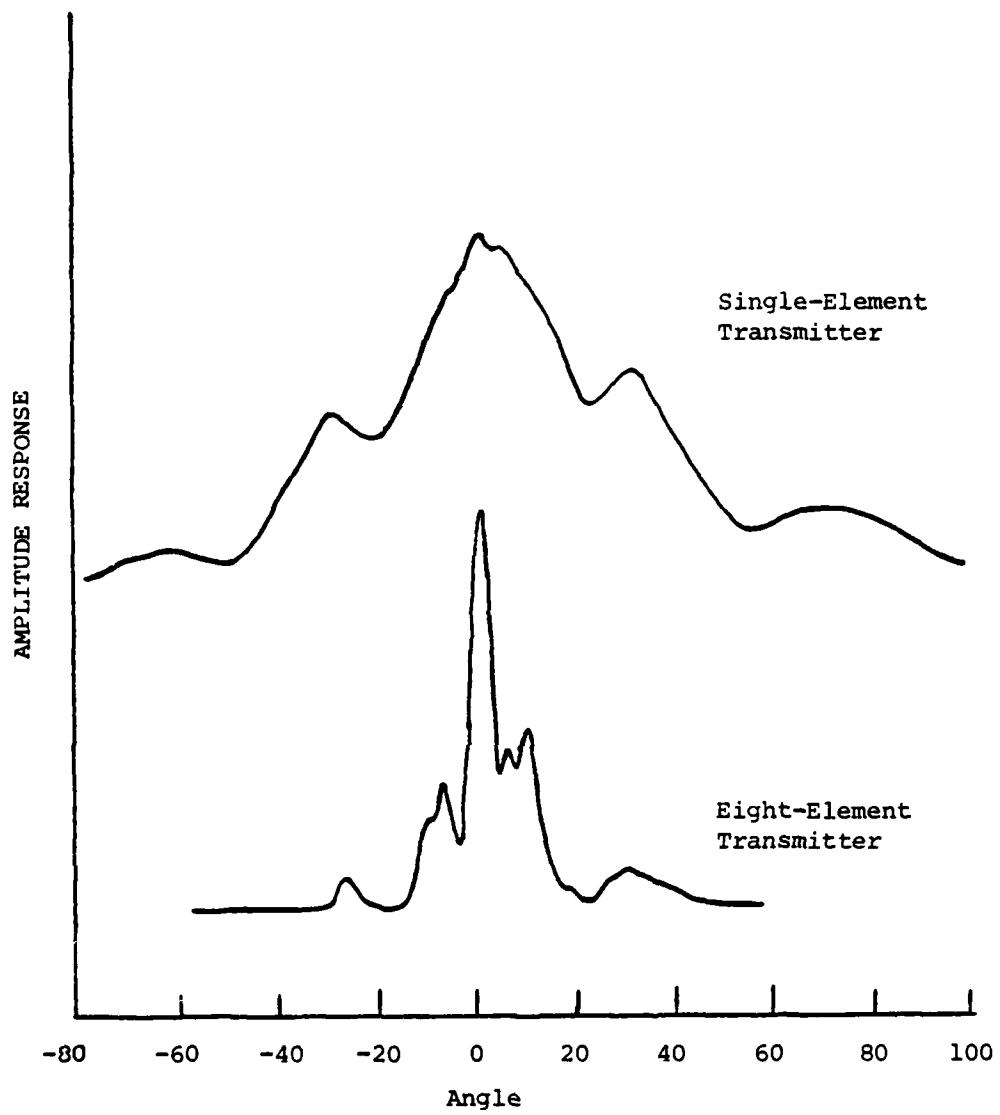
FIGURE 4.3: ARRAY SOUND FIELD DISTRIBUTION AS A
FUNCTION OF ANGULAR POSITION

in which the defect types were fabricated. The responses from the EDM notch samples arrived at times which corresponded to the block thickness; however, the hole samples were drilled to a depth of approximately 1/2 inch from the back surface of the block. Therefore, the ultrasonic returns from the tops of the hole defects arrived much earlier at the receiver because of the shorter travel paths in the metal specimen.

An analysis of the geometry of the data collection process for the outboard T/R can provide a bracket around the time at which an arrival can occur and be associated with a defect. In equation form, this can be stated as:

$$T_W \leq T_D \leq T_B + T_W \tag{4.3}$$

where T_B is the time corresponding to the block thickness and T_D is the time of the arrival in question. Arrivals occurring outside this time bracket can be excluded from consideration, while those within this time interval can be classified as potential defects.

The time criterion described in the above paragraphs is very helpful in removing several nondefect-related arrivals from consideration; however, in some specific situations, this single criterion is not sufficient. A good example of such a case is shown in Figure 4.4, which illustrates a recording in which a geometrical reflector generated an arrival which fell within the accepted time tolerances. The lower waveform depicted in this figure was obtained from a 0° EDM notch of size 20x60 mils. The front surface return occurred at approximately 53 μseconds and the defect response at approximately 95 μseconds. The arrival which occurred at 77 μseconds could be identified as
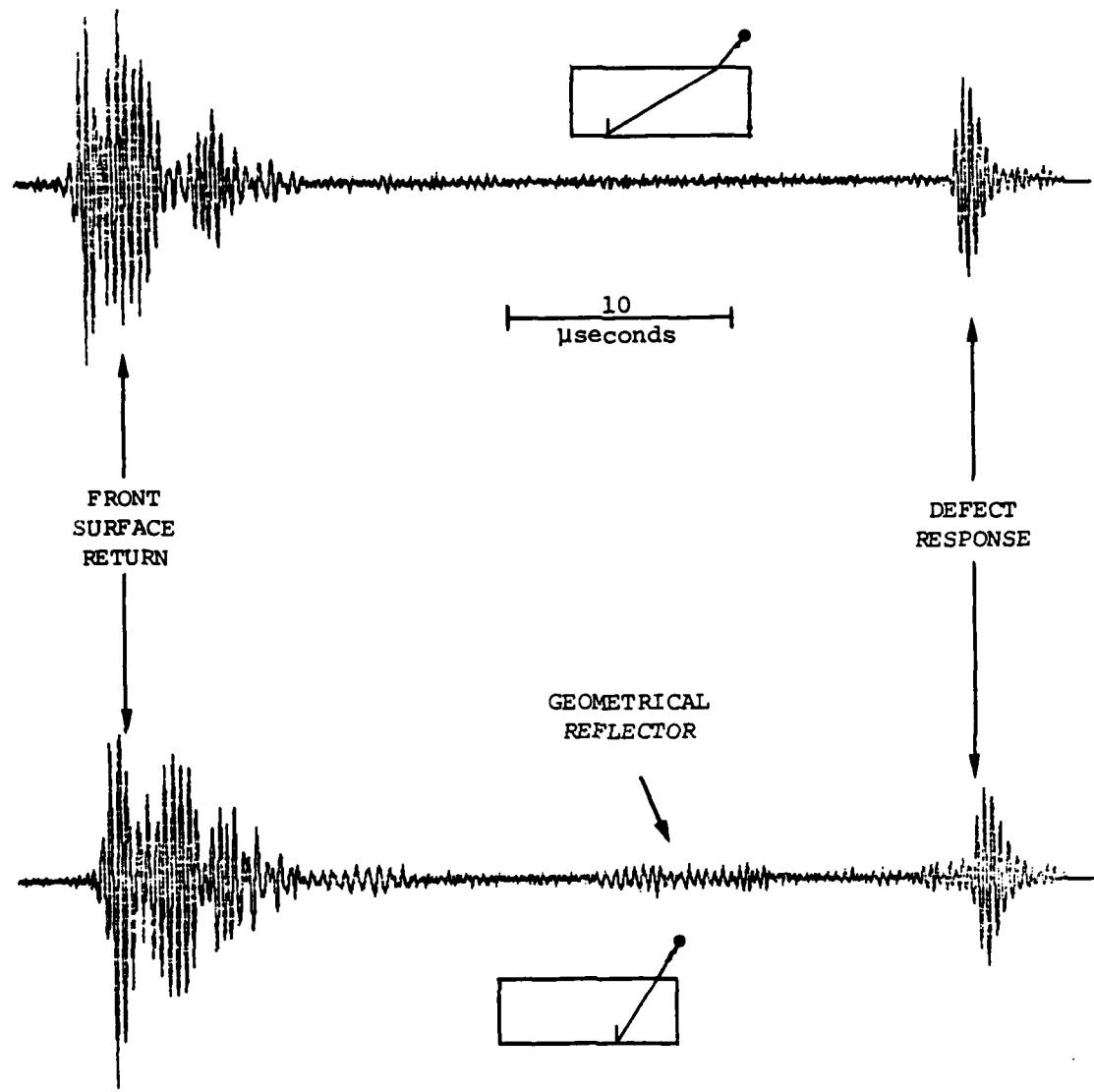
FIGURE 4.4: EXAMPLES OF PULSE-ECHO RECORDINGS OBTAINED FROM
THE SAME DEFECT ILLUSTRATING THE INFLUENCE OF
SPECIMEN GEOMETRY

4-8

a potential defect response; however, this arrival has been correlated with a return from the edge of the test block and is related to the wide angular response of the transmitter shown previously in Figure 4.3. The upper waveform shown in this figure was obtained from the same defect by rotating the test specimen 180°. The front surface and defect responses are nearly identical for both waveforms illustrated in this figure. The reflection which occurred at 77 μseconds in the lower signal was not present in the upper waveform. The schematic illustrations which accompany these two waveforms describe the transmitter and test specimen geometries for the two cases. The presence of the edge return is clearly depicted in these schematics and explains the difference in the two signals shown in the illustration.

A schematic diagram of the test specimen and the inboard T/R is shown in Figure 4.5. This situation was much simpler than that of the outboard T/R described above. A vertically traveling compressional wave was emitted from the transmitter into the water bath. This energy struck the front surface of the specimen, where part of the energy was reflected back toward the T/R and part was transmitted across the interface into the metal block. The compressional wave encountered several interfaces in the metal, which resulted in reflected, refracted, and diffracted signals. The reflections were sensed at the inboard receiver and then analyzed.

Examples of pulse-echo recordings obtained from a 0° flat-bottom and a round-bottom hole are shown in Figure 4.6. The large amplitude signals identified in these waveforms can be correlated with the front surface return, the defect response, the reflection from the backwall of the block, and various multiple reflections. Equations similar to those determined for the outboard T/R can

Inboard
Transmitter

Water
Line

D_W

Test
Block

D_M

Machined
Hole
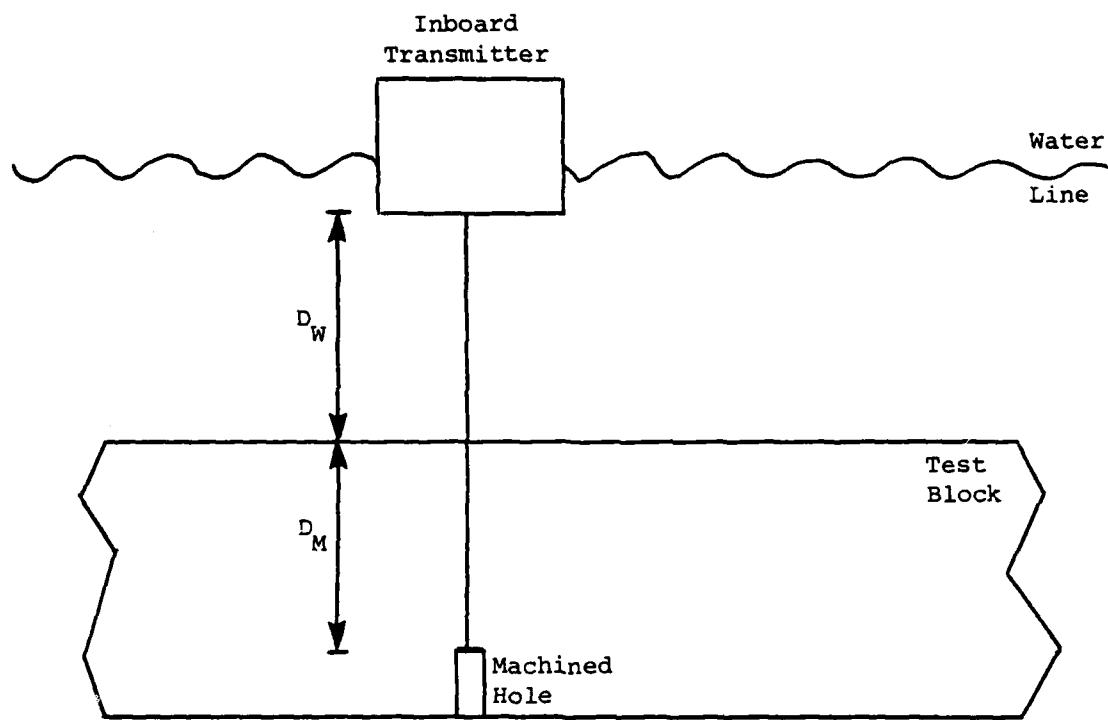
FIGURE 4.5: SCHEMATIC ILLUSTRATION OF ThE INBOARD TRANSMITTER
AND TEST BLOCK GEOMETRY

0° ROUND-BOTTOM HOLE
6/64" DIAMETER

10
μseconds

0° FLAT-BOTTOM HOLE
6/64" DIAMETER

FRONT
SURFACE   DEFECT   BACKWALL
RETURN   RETURN

0° ROUND-BOTTOM HOLE
12/64" DIAMETER

0° FLAT-BOTTOM HOLE
12/64" DIAMETER
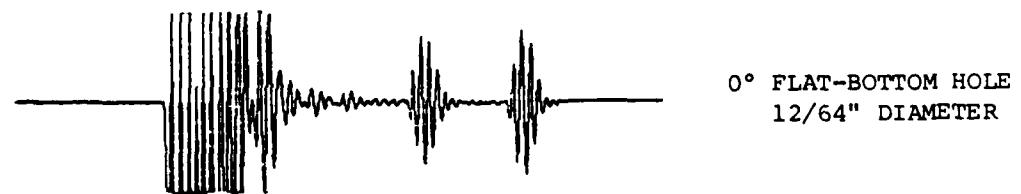
FIGURE 4.6:   EXAMPLES OF PULSE-ECHO RECORDINGS
              OBTAINED FROM THE INBOARD ARRAY

be derived to determine the water depth and metal depth estimates. The time constraints used to bracket the defect-related detections would also be similar to those discussed earlier.

The results obtained in this section have demonstrated that the geometry of the data collection exercise must be considered in the data analysis. Bracketing the time interval in which a detection can be correlated with a defect response has been shown to be very useful in removing many geometrical reflectors from consideration. However, special requirements are needed in certain situations to remove geometrical reflections which occur within the time tolerance limits. The sections which follow discuss the techniques used to improve the signal-to-noise ratios of the recorded waveforms to increase the detectability of the defect responses.

4.3 SIGNAL-TO-NOISE RATIO IMPROVEMENT

Previous analyses of ultrasonic signals have identified several viable approaches which have been used to improve the signal-to-noise ratios (SNR) of defect returns (Mucciardi, et al., 1980). Some of the more pertinent approaches with application to this study include bandpass filtering, matched filtering, temporal beamforming, and spatial beamforming. The bandpass filtering technique was tested and was found to be of limited usefulness to this work because the frequency domain characteristics of the background noise were quite similar to those of the defect returns and, therefore, could not be separated with a high degree of success. The matched filter technique was also evaluated during this program and was shown to be useful in certain

application areas. This approach involves convolving the recorded waveform with a reference signal which represents a particular defect response. The disadvantages of the matched filter algorithm include a large computational load for implementation because of the nature of the convolution filter and the fact that separate filters would be required for each defect type. The improvement in SNR offered by this technique was not sufficient to justify its incorporation into an automatic detection scheme. The two remaining SNR improvement algorithms, namely the temporal and spatial beamforming techniques, are easily implemented and have been proven to be extremely useful in suppressing background noise levels (O'Brien, et. al., 1980). The results obtained from these two signal processing tools are described below.

The temporal beamforming technique is a simple algorithm in which a number of waveforms are averaged to reduce background noise which occurs randomly in time. The approach involves positioning the transmitter and receiver at fixed spatial locations and repeating the data collection process a specified number of times. Under ideal circumstances, each successive waveform is identical to all others in the collection set. However, in the presence of random noise, each time-domain signal is different. In general, the defect response should be highly coherent and the noise segments should be relatively incoherent. A significant amount of the incoherent energy can be removed by averaging a set of waveforms according to the formula:

$$S(t) = \frac{1}{N} \sum_{i=1}^{N} s_i(t) \tag{4.4}$$

where $s_i(t)$ is the ith time waveform, N is the number of collected signals, and $S(t)$ represents the temporal beamforming output. An example of this

procedure is shown in Figure 4.7, where a set of ten individual waveforms and their corresponding temporal averages are presented. The reduction in the random background noise level is illustrated in this example. An investigation was conducted to determine the optimum number of waveforms to be collected in the averaging process. It was found that collecting a set of ten recordings offered maximum enhancement.

The main application of the temporal beamforming routine is to reduce the influence of background noise on the recording. The background noise in this case is mainly electronic system noise. In most ultrasonic applications, an additional noise source is related to the metal grain structure (Newhouse and Furgason, 1980). Temporal beamforming will not be effective in reducing grain noise because the grain reflections are coherent and will therefore be enhanced by the technique. Spatial beamforming has been shown to be a useful technique for removing grain noise in the waveforms. This approach is described in the following paragraphs.

A schematic illustration of the spatial beamforming technique is shown in Figure 4.8. In this diagram a set of six receivers (R_i) record the source energy. The distance from the source to each individual receiver is denoted as D_i. Under assumptions of plane wave propagation in a homogeneous medium and in the presence of no background noise, the waveforms recorded at each receiver, R_i, will be identical except for a time delay. This time delay is a function of the distance from the source to receiver and is given by:

$$\tau_i = \frac{D_R - D_i}{V} \tag{4.5}$$

INDIVIDUAL WAVEFORMS

10
μseconds
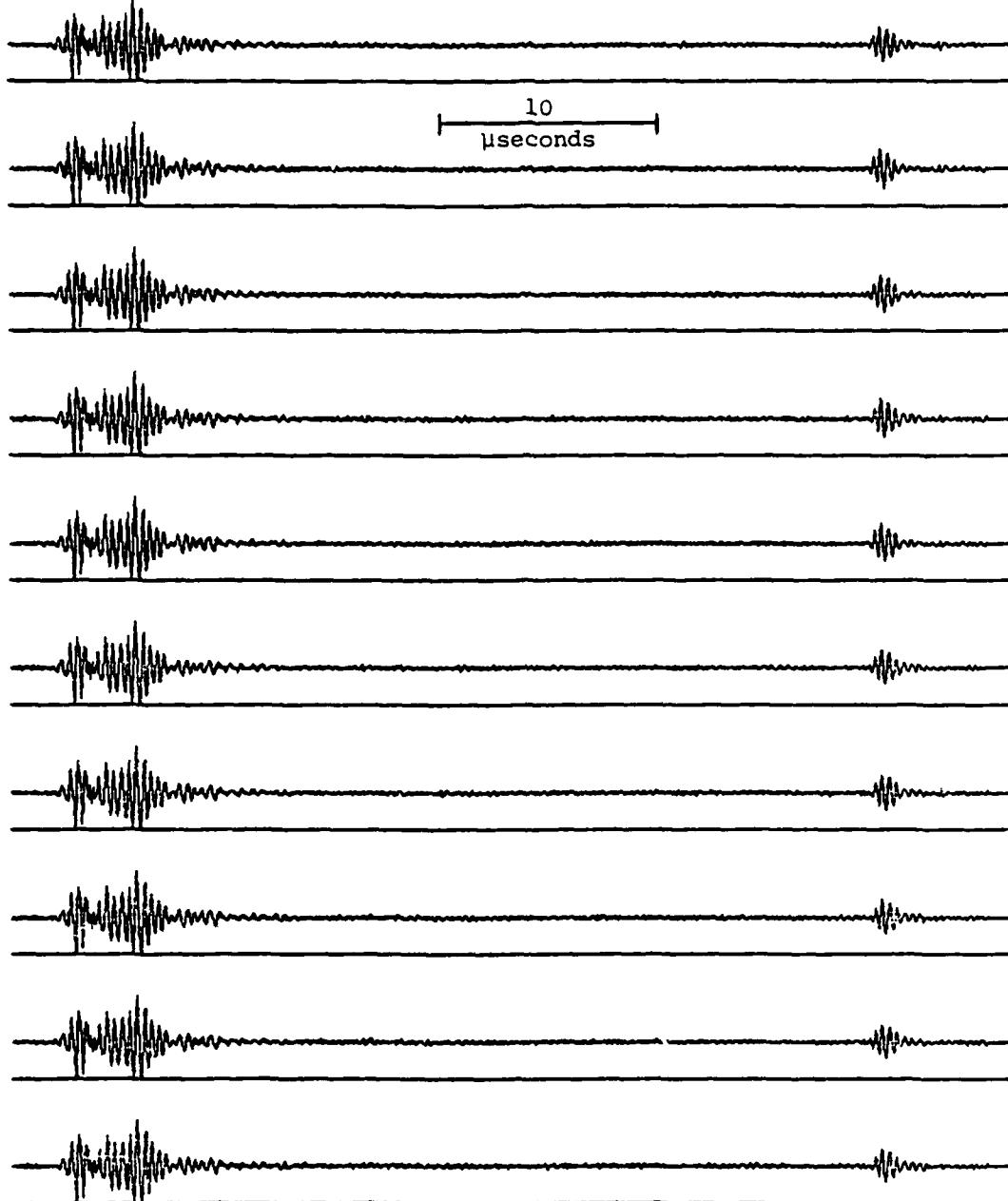
TEMPORAL AVERAGE
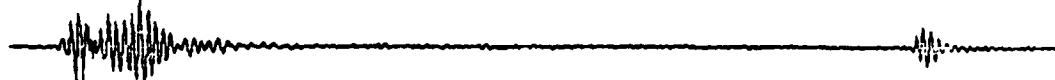
FIGURE 4.7: EXAMPLE OF TEMPORAL BEAMFORMING NOISE SUPPRESSION
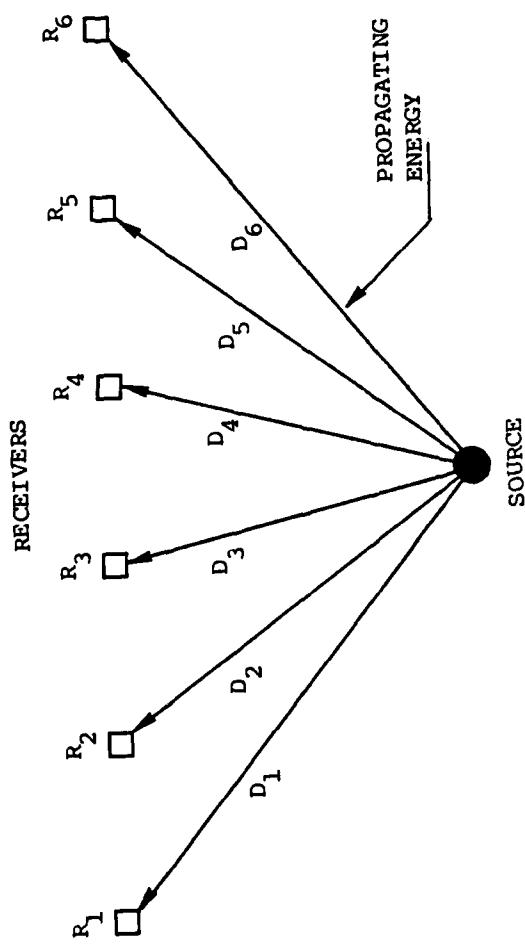
FIGURE 4.8: SCHEMATIC ILLUSTRATION OF THE SPATIAL BEAMFORMING APPROACH

where D_R is the distance to reference, D_i is the distance from the source to receiver i, and V represents the characteristic velocity of the medium. The beamformed output with respect to the reference receiver is then determined according to:

$$S(t) = \frac{1}{N} \sum_{i=1}^{N} s_i(t-\tau_i) \tag{4.6}$$

where the $s_i(t)$ is the recorded signal at receiver i, τ_i is the computed time delay, N is the number of receivers, and S(t) is the spatial beamforming output. Equation 4.6 is identical in form to the temporal beamforming result given in Equation 4.4, except for the incorporation of the time-delay factor. It is this difference between the two approaches which enables the grain noise to be suppressed, since the travel paths from source to receiver are all different and therefore encounter variable grain structures along their transmission paths.

An example of this approach is shown in Figure 4.9, where the response from a 30° EDM notch of size 70 x 350 mils at six receiver locations is presented. In this illustration the individual waveforms represent the average of ten successive recordings, so that the electronic noise has been effectively reduced. The defect responses are easily identified on each of these recordings and would not be a problem to detect using a very simple detector. The key observation to be made from this illustration concerns the consistency of the defect response at the individual receiver sites and the variability in the time waveforms outside the defect time windows. This variability is most likely related to the grain structure in the metal, but does not appear to influence the defect responses in a significant manner. In fact, this example
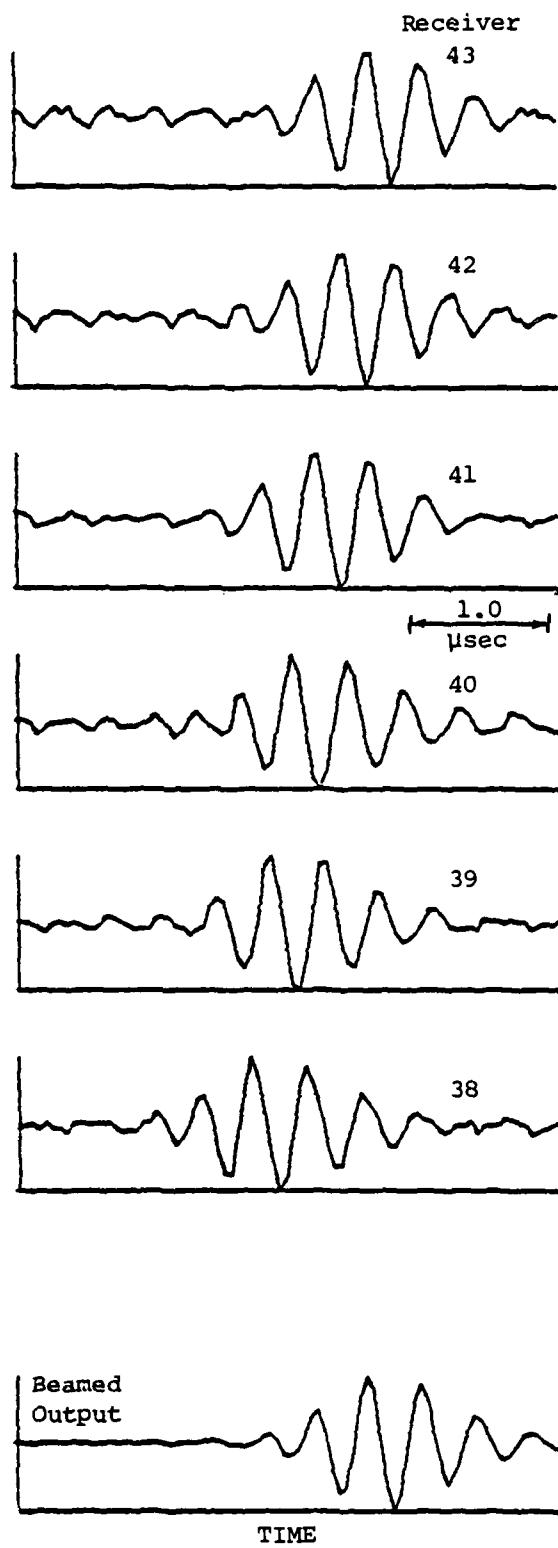
FIGURE 4.9: EXAMPLE OF SPATIAL BEAMFORMING APPLIED TO
SIX RECEIVERS (30° EDM Notch 70x350 mils)

provides a good opportunity for obtaining an experimental indication of what the true time delays within this receiver group should be. These experimental times were determined by cross correlating the recordings with a reference receiver (43). These time delays were then used to compute the spatial beam-formed response which is shown in the lower portion of Figure 4.9. The reduction in the noise level is significant, while the defect response is highly compatible with each of the individual observations.

A more dramatic example is shown for the same receiver grouping in Figure 4.10. These data were collected from a 30° EDM notch of size 20 x 100 mils. The defect response can be seen on receiver 43 but is virtually hidden by noise at the other five receiver locations. The same time delays determined from the experimental tests were applied to this receiver set to determine the beamed output shown in the lower portion of this figure. The results are extremely good in that the defect return is easily identifiable and is above the noise level of the beamed signal. It follows that the spatial beamforming technique is very useful in analyzing data recorded with the linear array.

Temporal and spatial beamforming techniques have been applied very success-fully to ultrasonic recordings obtained during this study. The reduction in electronic noise and metal grain noise are useful in detecting the presence of defect responses in the recorded waveforms. The detector selected for use in this application is described in the next section of this chapter.

Receiver
43

42

41

1.0
μsec

40

39

38

Beamed
Output

TIME
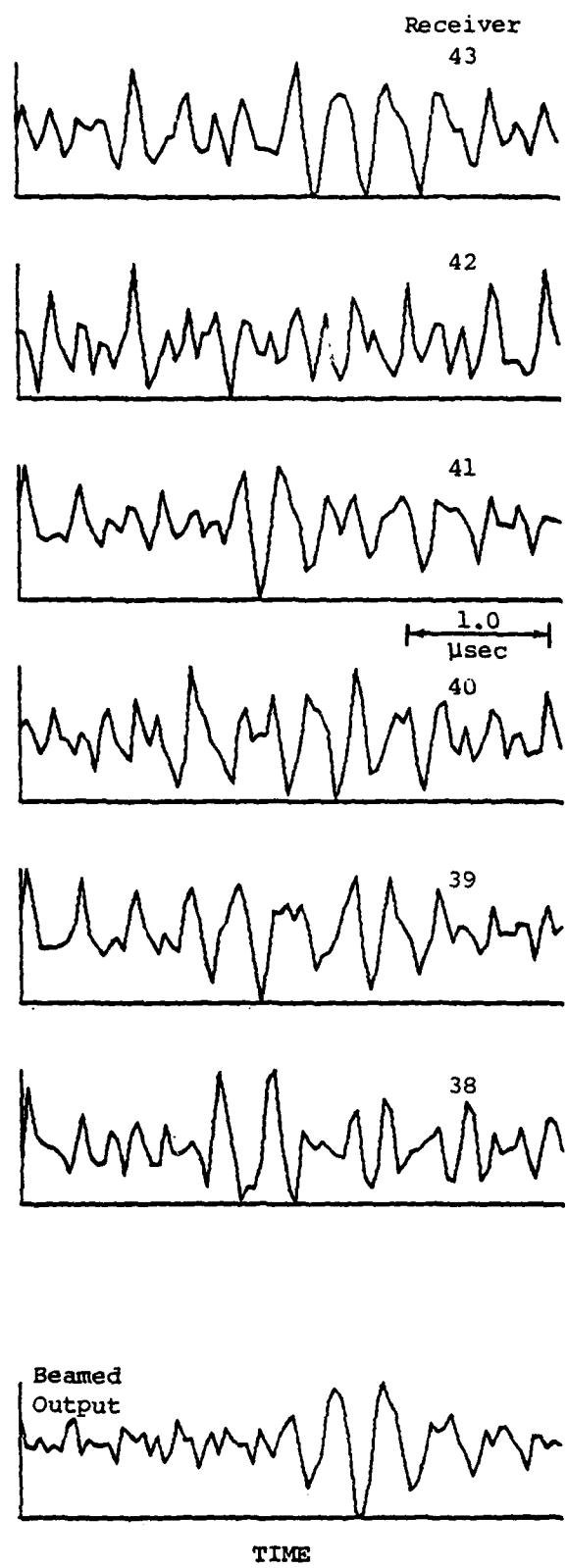
FIGURE 4.10:   EXAMPLE OF SPATIAL BEAMFORMING APPLIED TO
SIX RECEIVERS (30° EDM Notch 20x100 mils)

4-20

4.4 SIGNAL DETECTION

The signal processing techniques described previously in this chapter have been used as a preprocessing step to increase the signal-to-noise ratio of a collected waveform prior to inputting this waveform to a signal detection algorithm. The detection algorithm used in this program is a relatively sophisticated technique and is the main subject of discussion in this section.

The algorithm used in this study for detection purposes is essentially a power detector (Lane and Lemon, 1979) which computes a time-varying SNR ratio and compares this estimate with a preset threshold level. A detection is called when the SNR ratio exceeds the threshold level for a prescribed time duration. Before proceeding with a detailed discussion of the algorithm itself, a brief description of the parameters required as inputs to the detector will be given.

Two moving averages are required by the detection algorithm, a long-term average power (LTAP) and a short-term average power (STAP). The LTAP represents the estimate of _noise_ power and the STAP represents the estimate of _signal_ power. The lengths (LTAL and STAL) of these time windows are input constants used by the routine. A general rule is that STAL should approximate the time duration of a typical signal response, while LTAL should be about four times STAL. The detection threshold (THOLD) and update threshold (DHOLD) are further input constants used by the algorithm. DHOLD is generally less than the detection threshold and is used to freeze the updating of the LTAP in the simultaneous presence of signals and very high noise levels. Once the estimate of the signal-to-noise ratio (STAP/LTAP) exceeds THOLD, a detection

flag is turned on and must remain on for a prescribed number of points (NON) before a true detection is indicated. This feature enables the routine immediately to discard false detections which would be related to high-amplitude noise spikes and other short-duration artifacts.

The signal detector logic is shown in flow-chart form in Figure 4.11. Typical values of the LTAL, STAL, THOLD, DHOLD, and NON are identified on this figure. Experimentation was required to determine these optimum values so that all the defects of interest could be detected using constant values of these key parameters, thus making the detector independent of defect type.

The pulse-echo recording obtained at the outboard transmitter/receiver from a 0° EDM notch of size 20x60 mils is shown in the upper portion of Figure 4.12. The signal-to-noise ratio (STAP/LTAP) is shown in the lower half of this figure along with the threshold level indicated by the horizontal line. When the SNR exceeds the threshold level, a detection is signaled. The correspond-ing detections are illustrated along the time axis of the pulse-echo recording by arrows. The case presented in this figure is relatively simple, because only two clear detections are indicated. The first detection corresponds to the return from the front surface of the block and the second is related to the EDM notch defect. An example of a more complex situation is shown in Figure 4.13, which represents the pulse-echo waveform obtained from a 0° flat-bottom hole of diameter 10/64 inch. A number of detections are indicated in this example. The first detection is related to the front surface of the block and is followed by the response from the flat-bottom hole defect. The detection which follows the defect return corresponds to energy being reflected from the back wall of the test specimen and is not defect-related.
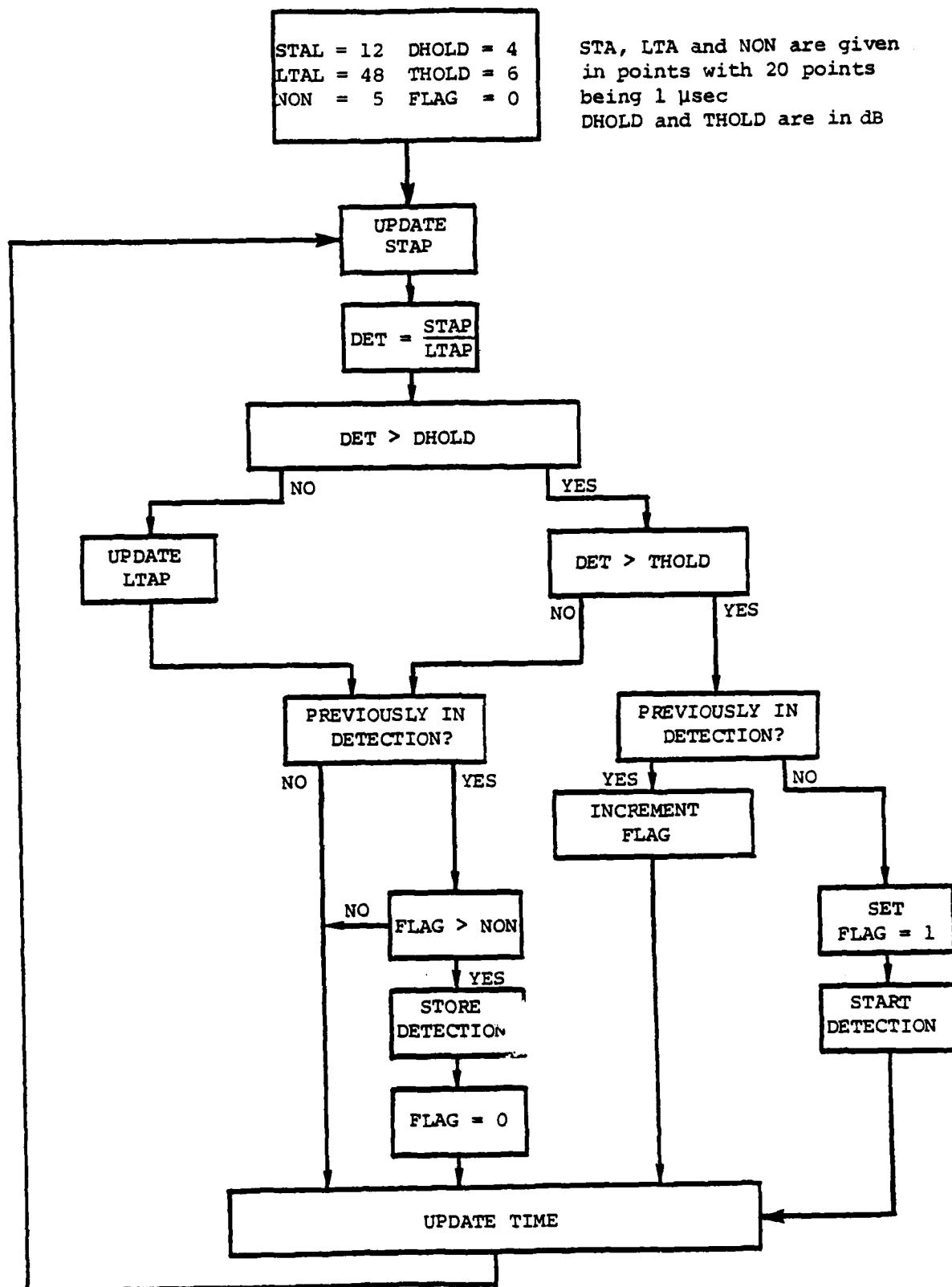
FIGURE 4.11:   FLOW DIAGRAM OF SIGNAL DETECTOR LOGIC

4-23
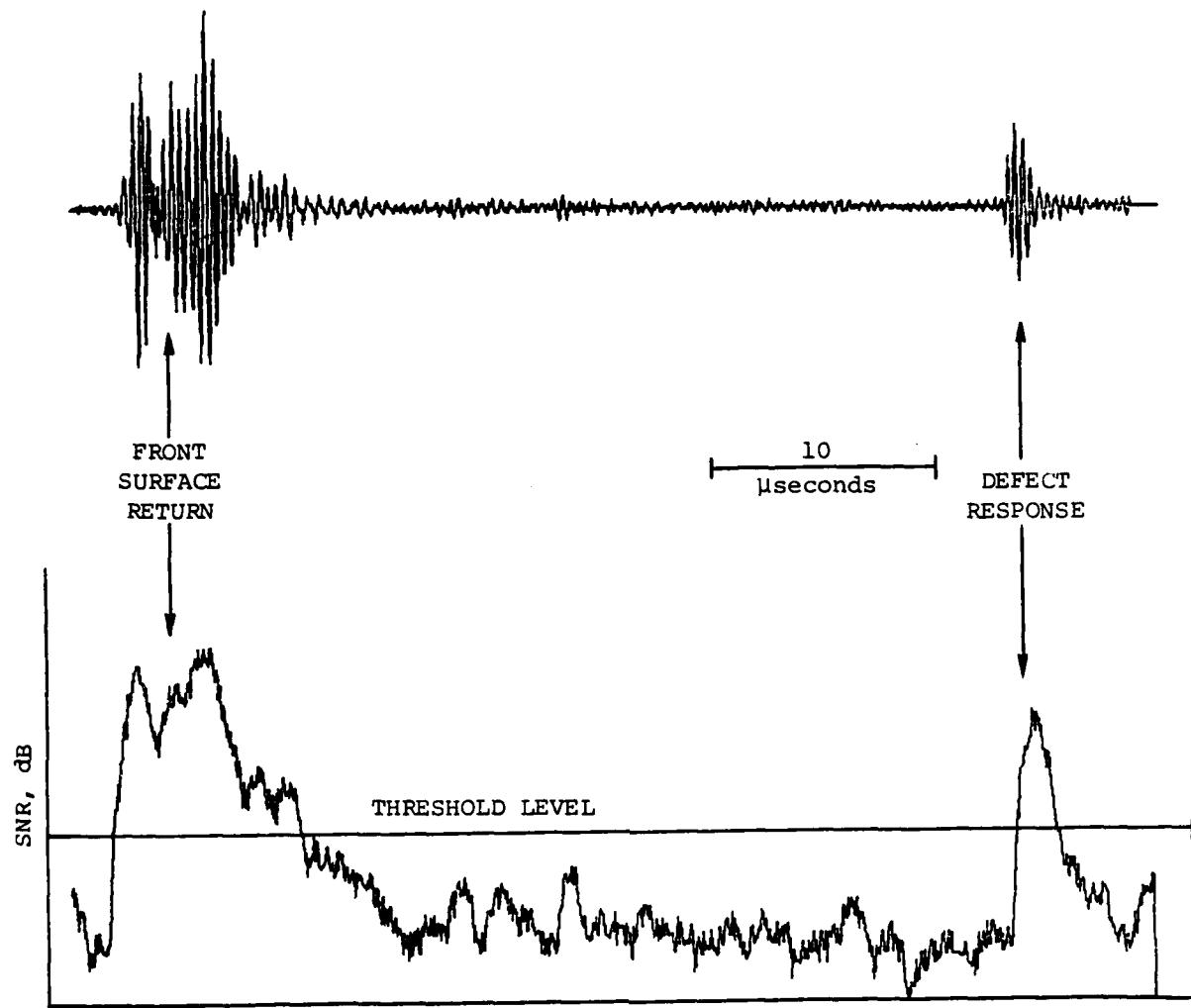
FIGURE 4.12: COMPARISON OF A PULSE-ECHO RECORDING WITH THE OUTPUT
SIGNAL-TO-NOISE RATIO PROVIDED BY THE SIGNAL DETECTOR
(0° EDM Notch 20x60 mils)
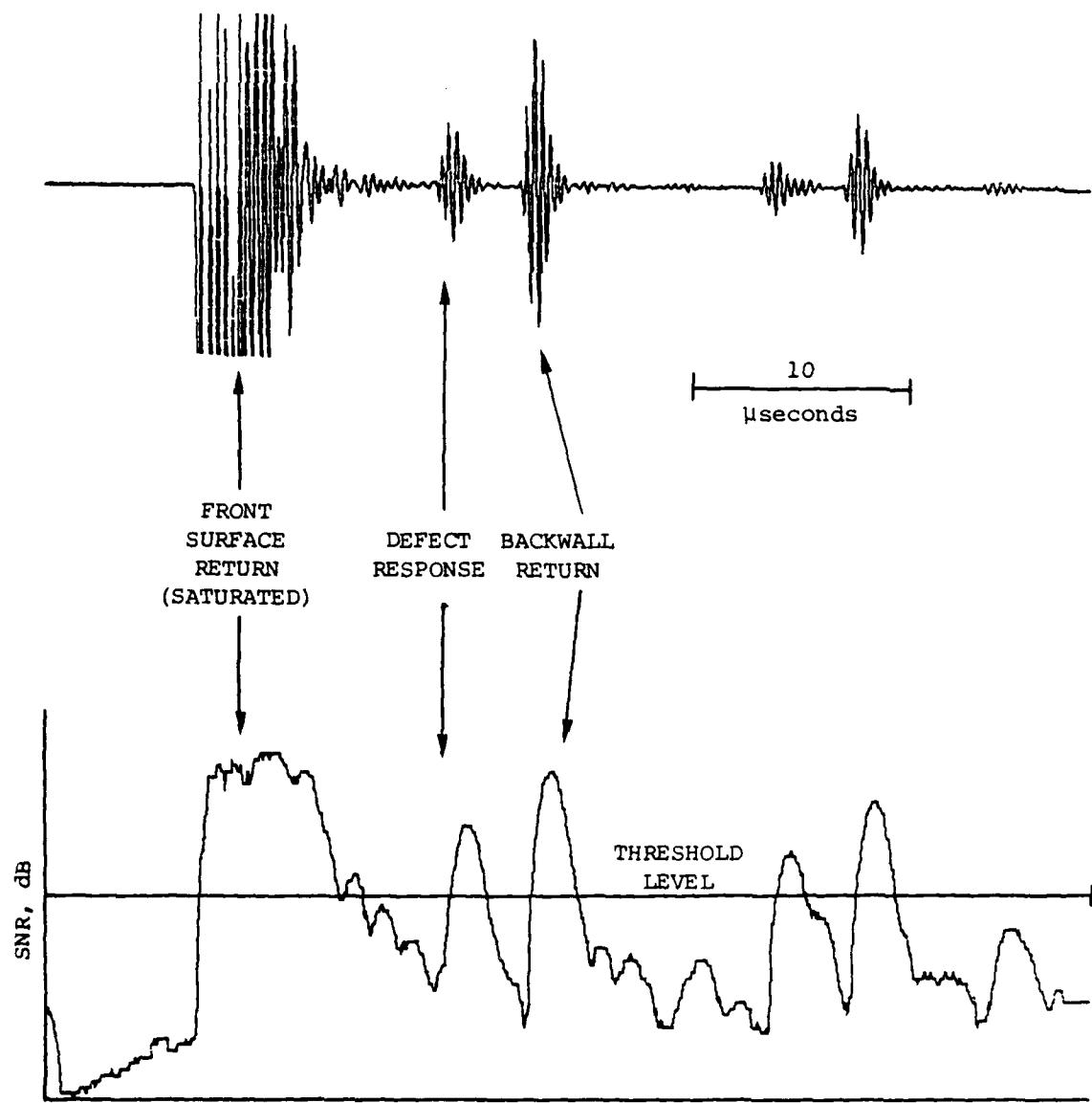
FIGURE 4.13: COMPARISON OF A PULSE-ECHO RECORDING WITH THE OUTPUT
SIGNAL-TO-NOISE RATIO PROVIDED BY THE SIGNAL DETECTOR
(0° Flat-Bottom Hole 8/64" Diameter)

The signal detector described in this section provides a summary of all signals which exceed the preset threshold value. The arrival times of these detections are then evaluated using procedures outlined in Section 4.2 to determine if any of the detections in the list are defect-related.

The signal detection and detection association algorithms have been implemented in microprocessor software in the ALN 4000. This process provides an automatic defect detection capability and has been shown to yield very consistent and accurate indications of the presence of flaws in metal specimens.

5. DEFECT CHARACTERIZATION

5.1 APPROACH

The ultrasonic data collected from the set of machined defects were subjected to a variety of analysis procedures to obtain measurements from the recorded waveforms which could be used for defect characterization purposes. The features most commonly used in these analyses consisted of both time-domain and frequency-domain representations of the defect signatures. The extracted features were then input to Adaptive Learning Network (ALN) models to identify the key signal features selected by the models as well as to obtain the structure of the relationships between the input and output variables.

The entire defect characterization process was composed of three individual operations. The first step involved classification of the defect into one of the three categories considered in this study, EDM notches, flat-bottom holes, and round-bottom holes. The second process was concerned with determining the angular orientation of the defect, and the third step involved estimating the size of the defect, i.e., length and depth for the notch samples and diameter for the hole specimens. The procedures employed in each of these character- ization steps are discussed in the subsequent sections of this chapter.

Although the specific features used as inputs to the ALN models depend upon the type and orientation of the defect, a set of relatively general operations can be defined which are appropriate for all defect categories. These general steps are shown in Figure 5.1.

```
           ┌─────────────────────┐
           │      ACQUIRE        │
           │   TIME WAVEFORMS    │
           └─────────────────────┘
                     │
                     ▼
           ┌─────────────────────┐
           │   FORM BEAMS OVER   │
           │   ARRAY ELEMENTS    │
           └─────────────────────┘
                     │
                     ▼
           ┌─────────────────────┐
           │   COMPUTE POWER     │
           │      SPECTRA        │
           └─────────────────────┘
                     │
                     ▼
           ┌─────────────────────┐
           │  PARTITION SPECTRA  │
           │     INTO FOUR       │
           │  FREQUENCY BANDS    │
           └─────────────────────┘
                     │
                     ▼
           ┌─────────────────────┐
           │   COMPUTE ARRAY     │
           │  CENTER OF GRAVITY  │
           │    FOR EACH BAND    │
           └─────────────────────┘
                     │
                     ▼
           ┌─────────────────────┐
           │   COMPUTE POWER     │
           │ DISTRIBUTIONS AND   │
           │   RATIOS ACROSS     │
           │      THE ARRAY      │
           └─────────────────────┘
                     │
                     ▼
           ┌─────────────────────┐
           │   INPUT FEATURES    │
           │   TO  ALN  MODELS   │
           └─────────────────────┘
                     │
                     ▼
           ┌─────────────────────┐
           │     SYNTHESIZE      │
           │     ALN MODELS      │
           └─────────────────────┘
```
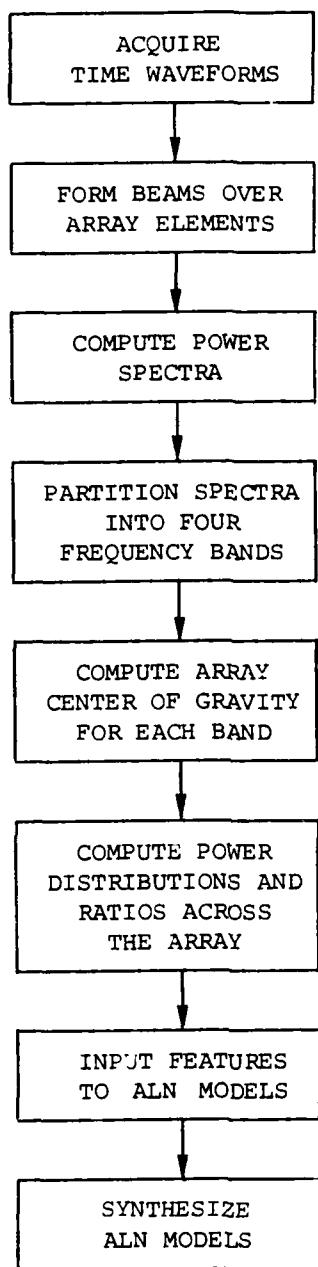
FIGURE 5.1: FEATURE EXTRACTION PROCEDURES

The first step requires that appropriate waveforms be collected using various transmitter and receiver protocols. In cases where several adjacent array elements are recorded, a spatial beamformed signal is calculated in an attempt to increase the defect response over the background and grain noise. These beamformed signals are then input to a Fast Fourier Transform (FFT) algorithm which converts the time-domain representation to its frequency-domain equivalent. The power spectrum is partitioned into four frequency bands of interest for further analysis. The receiver groupings used to form the beamed signals and the four frequency bands used in this study are identified in Table 5.1. Once these computations have been performed, the spectral data are then subjected to numerous feature extraction routines. These features include the center of gravity of the power distribution across the array for each frequency band and a number of power ratios involving various receiver combinations. Each of these feature categories has been shown to be extremely useful in previous investigations (Lane and Lemon, 1979; O'Brien, et al., 1980). These candidates are then input into ALN models to determine the most diagnostic set of parameters as well as the functional relationship between these key variables and the defect characteristic of interest. The specific features used for each defect category are identified in appropriate subsections of this chapter.

5.2 DEFECT CLASSIFICATION AND ORIENTATION

The defect classification scheme employed in this study incorporates geometrical, temporal, and spatial properties of the collected waveforms in the decision-making process. Two pulse-echo recordings are available for

TABLE 5.1: IDENTIFICATION OF REFERENCE BEAM NUMBERS AND FREQUENCY BANDS
USED IN FEATURE EXTRACTION EXERCISES

BEAM NUMBER	RECEIVER GROUPING
1	47
2	46, 45, 44
3	43, 42, 41
4	40, 39, 38
5	31, 30, 29
6	28, 27, 26
7	25, 24, 23
8	22, 21, 20
9	19, 18, 17

FREQUENCY BAND NUMBER	FREQUENCY INTERVAL
1	1.56 - 2.10 MHz
2	2.18 - 2.73 MHz
3	2.81 - 3.36 MHz
4	1.56 - 3.36 MHz

analysis, one from the 0° inboard T/R and one from the angled outboard T/R. Based on geometrical considerations, it is obvious that the 30° holes and the EDM notches are detected on the outboard T/R while the 0° holes are visible on the inboard T/R. Thus, the identity of the T/R which detects the presence of a defect response can be used as a classification tool by separating the defect types into two categories, with one group containing the 0° holes and the second group containing the 30° holes and the EDM notches. This second group can be split into its two components by considering the arrival time of the defect response. The notch returns appear at a time which corresponds to the back surface of the test specimen. The 30° hole flaws represent defects occurring in free space and are not connected to the back of the test block. Therefore, the 30° hole responses will arrive at an earlier time than the notch echoes because of the shorter travel paths.

The procedures outlined above can be used to separate the defect returns into one of three categories, EDM notches, 30° holes, and 0° holes. Classification of the hole defects into flat-bottom or round-bottom holes can be accomplished by activating other receiver elements within the array package to determine the amount of energy which has been scattered by the defect to these receiver positions. It was found that the ultrasonic energy scattered by the flat-bottom hole defects is considerably higher than that scattered from the round-bottom hole defects. In fact, the energy scattered in the pitch-catch mode could not be detected for the round-bottom hole flaws. This detection difficulty may, in fact, be related to the observation made earlier concerning the nonspherical tips of these round-bottom holes; however, the experimental observation made concerning the rapid decay of energy in the scattered field for the spherical defects is consistent with both theoretical (Domay, et al.,

1979) and previously-reported experimental results (Whalen, et al., 1979). The results observed for the flat-bottom holes are also supported in the literature (Achenbach, et al., 1979; Whalen, et al., 1979). It appears that this decay of ultrasonic energy in the scattered field can be used as a diagnostic feature to discriminate between the flat-bottom and round-bottom holes.

The defect classification scheme described above is presented as a logic diagram in Figure 5.2. It is interesting to note that this scheme has not only resulted in defect classification, but also has yielded the angular orientations of the hole defects. The notch orientations cannot be determined from this scheme and, therefore, require a more detailed analysis.

Examples of pulse-echo recordings obtained from a 50x150-mil and a 50x250-mil EDM notch at angular orientations of 0° and 30° are shown in Figure 5.3. A comparison of the 0° and 30° defect responses for the same size defect indicates that the time-domain responses are quite similar in shape but differ slightly in amplitude, with the 0° response having the higher value. However, this amplitude difference is not helpful in determining the defect orientation, because a 30° notch of larger size than a 0° notch could conceivably possess nearly identical amplitude values. A more diagnostic approach is illustrated in Figure 5.4, which presents a comparison of the diffracted ('SS') and mode-converted ('SP') energies obtained from 50x250-mil notches at the two angular orientations. Note that the mode-converted energy is much more prevalent for the 0° notch, while the diffracted energy recorded at receivers near the transmitter is more dominant for the 30° notch. The situation depicted here was found to be quite representative of the other EDM notch samples and was determined to be independent of the notch size.
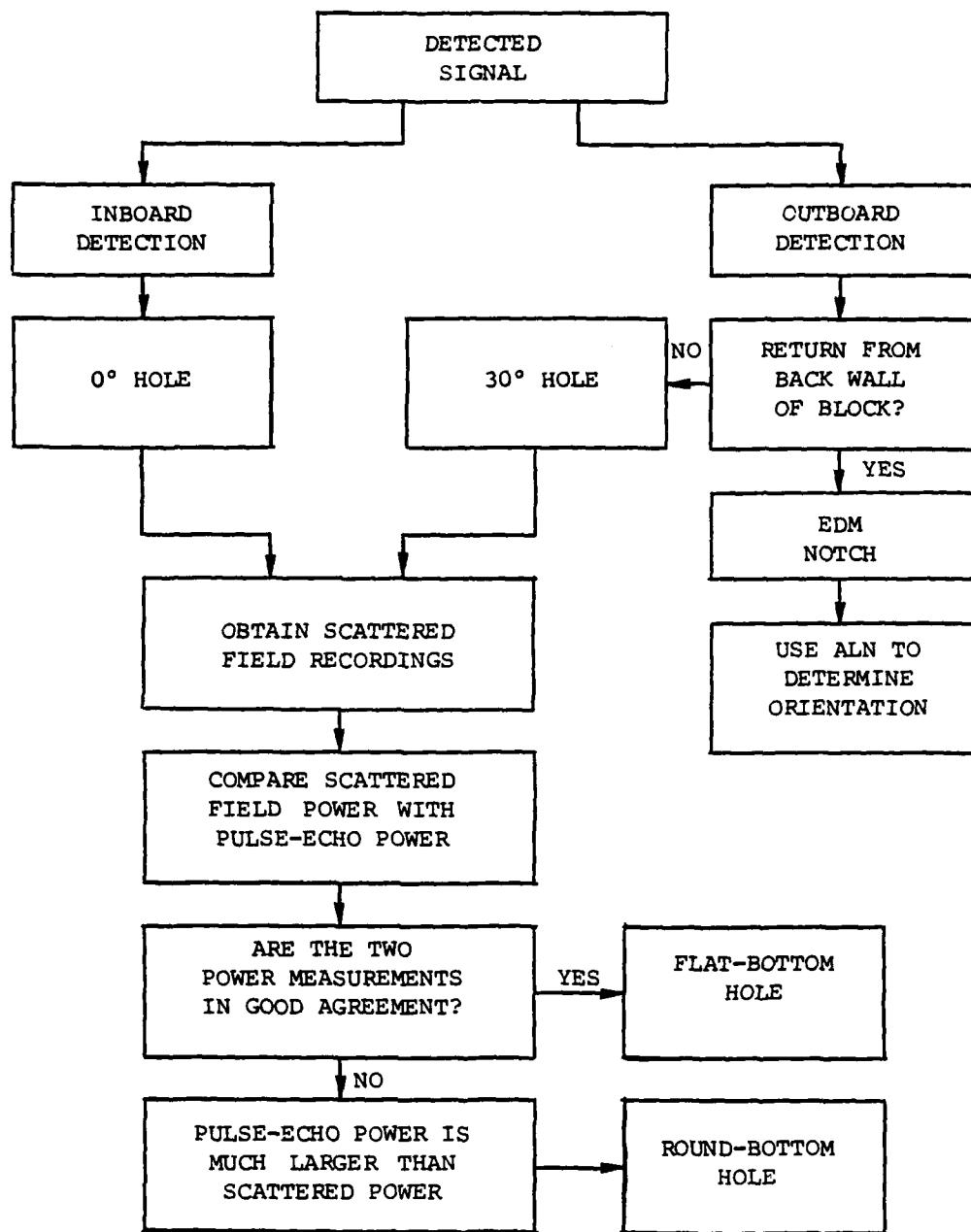
FIGURE 5.2: LOGIC DIAGRAM OF DEFECT CLASSIFICATION
AND ORIENTATION PROCESS

50 x 150 MIL EDM NOTCH

0° ORIENTATION

30° ORIENTATION
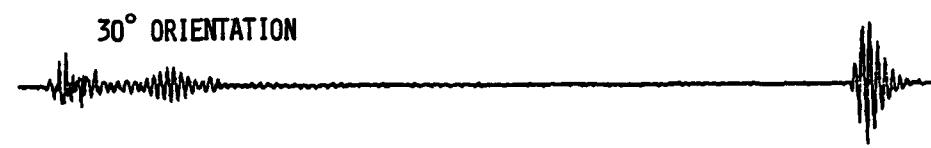
50 x 250 MIL EDM NOTCH

0° ORIENTATION

7
μSECONDS
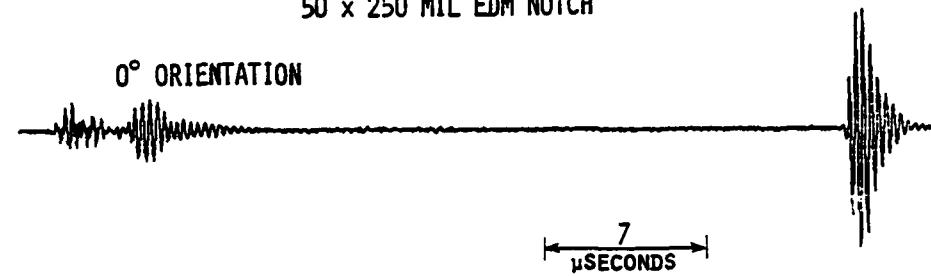
30° ORIENTATION
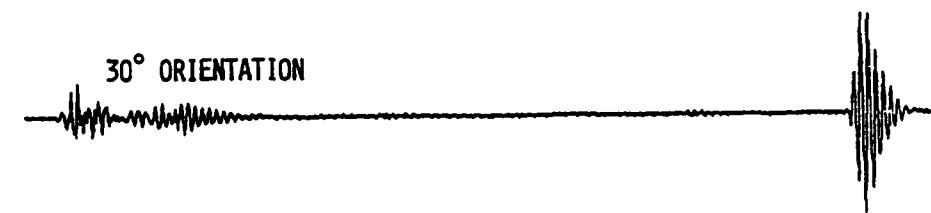
FIGURE 5.3: EXAMPLES OF PULSE-ECHO RECORDINGS FROM A
50x150- and 50x250-MIL EDM NOTCH ORIENTED
AT 0° AND 30°

RECEIVER

'SS'
SIGNAL

43   41   38

'SP'
SIGNAL

'SS'
SIGNAL

30

'SP'
SIGNAL

28

3
μSECONDS

22

20

0° ORIENTATION

30° ORIENTATION
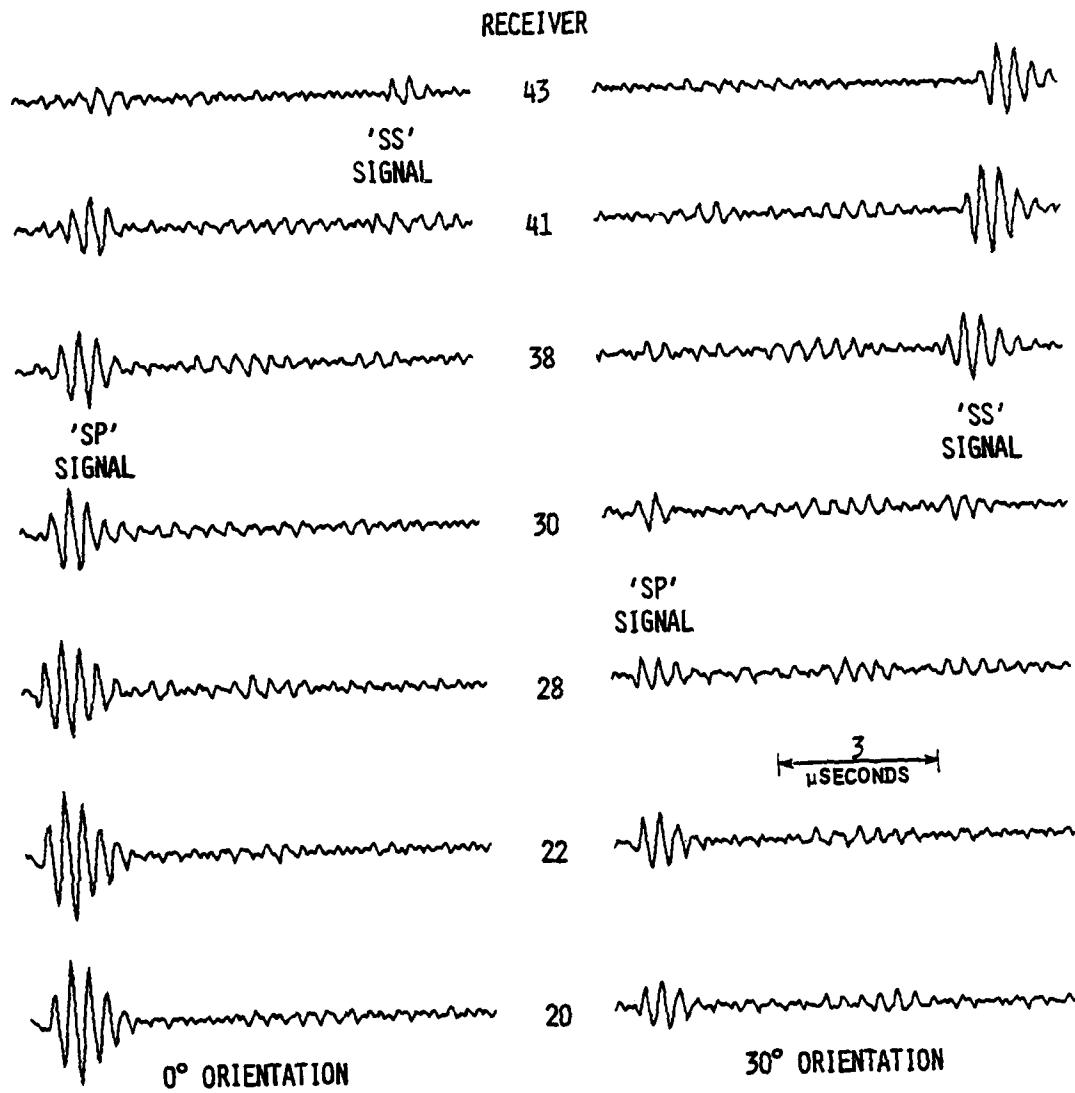
FIGURE 5.4:   EXAMPLES OF SCATTERED WAVEFORMS RECORDED AT VARIOUS
RECEIVER LOCATIONS FOR A 50x250-MIL NOTCH ORIENTED
AT 0° AND 30°

Both the pulse-echo and scattered field recordings were collected for each of the 32 EDM notches comprising the data base. The pulse-echo *waveforms were* detected in all cases; however, the scattered energy for six of the smallest notches could not be detected with a high degree of accuracy even though averages of ten successive recordings were computed to remove temporal noise variations. The remaining 26 observations were subjected to various feature extraction routines to acquire parameters for use in estimating the orientations of the notches.

Fourier power spectra were computed for the pulse-echo, the mode converted, and the diffracted waveforms. These power spectra were divided into three frequency intervals (1.56-2.10 MHz, 2.18-2.73 MHz, and 2.81-3.36 MHz), and ratios of these powers were taken over various receiver combinations. A tabulation of the candidate features input into the ALN model is given in Table 5.2. The resulting ALN model is shown in Figure 5.5; it uses two inputs: (1) the ratio of 'SS' power (diffracted energy) in the frequency band between 1.56 to 2.10 MHz, at receivers 41, 40, and 39, to the pulse-echo recording at receiver 47; and (2) the ratio of power in the same band at receivers 47, 46, and 45 to receivers 44, 43, and 42. The performance of the resulting model is illustrated in Figure 5.6, where the deviations between the true angle and estimated angle are plotted. The largest deviation of 12° observed in this sample resulted from the 20x100-mil 0° EDM notch specimen. The average residual was less than 5° for the entire sample. The predicted performance for unseen data is estimated to average approximately 8.5°. It is interesting to note from the residuals shown in Figure 5.6 that the deviations for the larger defects are not any less than those for the smaller notches, thus *indicating that the ALN model is independent of defect size.*

TABLE 5.2: LIST OF CANDIDATE FEATURES FOR THE EDM
NOTCH ANGLE ORIENTATIONS

Feature Number	Description	
X3	Center of gravity of power distribution across array	(Band 1)
X4	Center of gravity of power distribution across array	(Band 2)
X5	Center of gravity of power distribution across array	(Band 3)
X6	Center of gravity of power distribution across array	(Band 4)
X7	Sum of normalized power, Receivers 47, 46, 45	(Band 1)
X8	Sum of normalized power, Receivers 44, 43, 42	(Band 1)
X9	Sum of normalized power, Receivers 41, 40, 39	(Band 1)
X10	Ratio of total normalized power, Receivers 47, 46, 45 to 42, 43, 44	(Band 1)
X11	Ratio of total normalized power, Receivers 47, 46, 45 to 39, 40, 41	(Band 1)
X12	Ratio of total normalized power, Receivers 42, 43, 44 to 39, 40, 41	(Band 1)
X13-X18	Same as features X7-X12	(Band 2)
X19-X25	Same as features X7-X12	(Band 3)
X26-X32	Same as features X7-X12	(Band 4)

Power was normalized by the pulse-echo power (Receiver 47).

Receiver 47 is pulse-echo energy; Receivers 39 through 46 are diffracted energy ('SS').
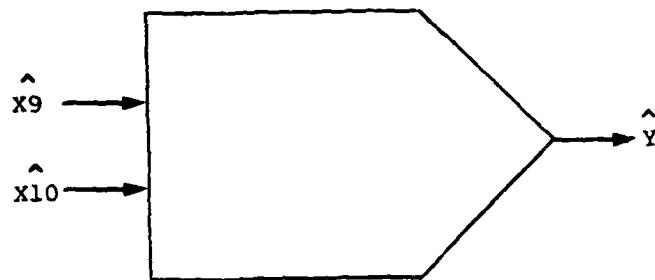
$$\hat{Y} = 0.64 + 1.50 \hat{X9} + 0.25 \hat{X10} - 0.64 \hat{X9}^2$$

Where:

$$\hat{X} = (X-\overline{X})/\sigma_X$$

$$Y = \hat{Y}\sigma_Y + \overline{Y}$$

With:

$\overline{X9}$ = 5.58		σ_{X9} = 5.04	
$\overline{X10}$ = 1.88		σ_{X10} = 1.26	
$\overline{Y}$ = 15.0		σ_Y = 15.0	
$\overline{E}$ = 4.8		$\overline{E}_p$ = 8.5	

FIGURE 5.5: ALN DETERMINED FOR ESTIMATING THE EDM NOTCH ORIENTATION
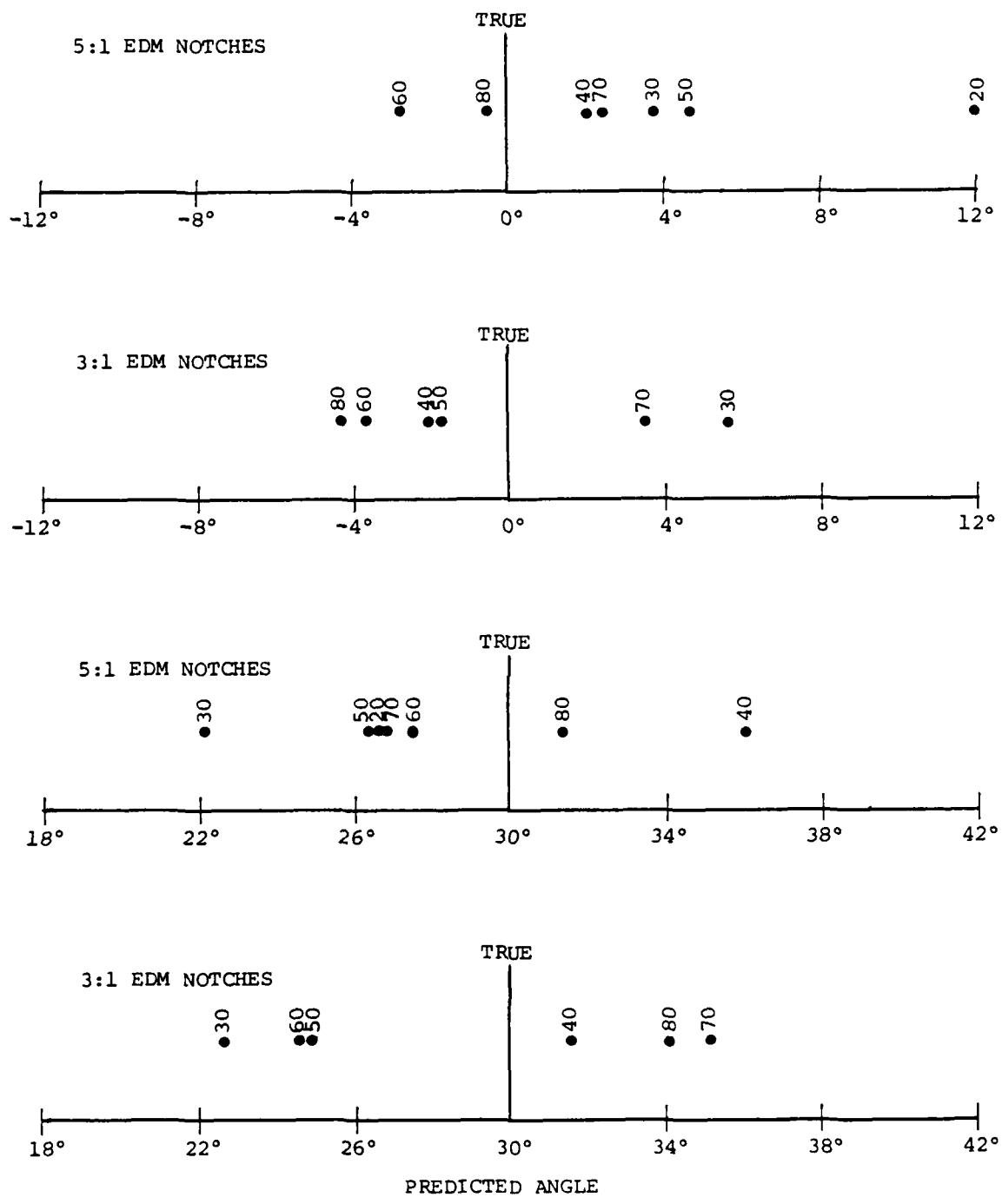
FIGURE 5.6: COMPARISON OF TRUE ANGLES WITH ALN PREDICTED ANGLES
FOR VARIOUS EDM NOTCH DEFECTS (Depths are indicated
in mils)

5.3 DEFECT SIZE ESTIMATION

The defect characteristics discussed up until this point have emphasized the classification and orientation of the flaws. In general, these parameters are required for total defect characterization purposes but are less crucial than estimates of the actual size of the flaw. Most judgments made concerning material integrity are based primarily on the size of the defect located in the critical component rather than on its type or orientation. Accurate and reliable defect size models are required to assist the analyst in his decision-making process. In this section, ALN models are obtained for defect size estimation using features extracted from the ultrasonic flaw responses. The performance of these models is then assessed in terms of prediction capability and reliability.

5.3.1 EDM Notch Size Estimation

To obtain complete size characterization for the EDM notch samples, two independent quantities must be modeled, the depth and length of the notch. The situation is further complicated by the fact that these estimates must be determined for a set of two angular orientations.

The differences in the scattered energy for these two orientations were discussed earlier in this chapter (see Figure 5.4) and will not be repeated here. Attempts were made earlier in this program to group the two angular classes into one set for size estimation; however, average errors on the order of 20% were obtained from the ALN models. This large error was not acceptable, and

the decision was made to model the defect size for each separate angle group. The models determined from this approach resulted in much smaller errors than the combined grouping and are discussed in detail in the following paragraphs.

Individual waveforms were acquired at receiver numbers 17 through 47 for all 0° EDM notches with the exception of the 10-mil-deep notches. Although the pulse-echo (receiver 47) response could be detected, the smaller amplitude signals from the 10-mil-deep defects could not be detected at other receiver locations within the array. A set of nine beamformed signals was computed from the various receiver groups. Power spectra were then calculated for the pulse-echo signal and for the mode-converted ('SP') waveforms and used to determine values for the features summarized in Table 5.3. These features were input to an ALN analysis for the purpose of estimating the depth of the 0° EDM notches.

The resulting model is shown in Figure 5.7. Two features were selected by the ALN model, (1) the ratio of power in Beams 3 through 7 to Beams 7 through 9 for frequencies between 1.56 and 2.10 MHz, and (2) the ratio of power in Beams 3 through 7 to the total power over the frequency range from 1.56 to 3.36 MHz. The average RMS error on the defect depth was 6.2 mils (12%), and the predicted error for unseen data was 12 mils. A comparison of observed and predicted depth values is shown in Figure 5.8. The results indicated in this figure are quite good and indicate that the model performs equally well over the entire depth range from 20 to 80 mils. The largest single deviation obtained was 12 mils for the 40x200-mil EDM notch. The majority of the deviations were on the order of 4 to 6 mils.

TABLE 5.3: LIST OF C. ...TGATE FEATURES FOR THE 0° EDM NOTCH DEFECTS

Feature Number	Description	
X3	Center of gravity of power distribution across array	(Band 1)
X4	Center of gravity of power distribution across array	(Band 2)
X5	Center of gravity of power distribution across array	(Band 3)
X6	Center of gravity of power distribution across array	(Band 4)
X7	Ratio of power in beams 7, 8, 9 to total power	(Band 1)
X8	Ratio of power in beams 5, 6, 7 to total power	(Band 1)
X9	Ratio of power in beams 3, 4 to total power	(Band 1)
X10	Ratio of power in beam 8 to total power	(Band 1)
X11	Ratio of power in beam 7 to total power	(Band 1)
X12	Ratio of power in beam 6 to total power	(Band 1)
X13	Ratio of power in beams 5, 6, 7, 8, 9 to total power	(Band 1)
X14	Ratio of power in beams 3, 4, 5, 6, 7 to total power	(Band 1)
X15	Ratio of power in beams 3, 4 to beams 7, 8, 9	(Band 1)
X16	Ratio of power in beams 3, 4, 5, 6, 7 to beams 7, 8, 9	(Band 1)
X17-X26	Same features as X7-X16	(Band 2)
X27-X36	Same features as X7-X16	(Band 3)
X37-X46	Same features as X7-X16	(Band 4)

Total power is defined as the sum of the individual powers represented in beams 1 through 9.

Beam 1 is pulse-echo energy; beams 2 through 9 are mode-converted energy ('SP').
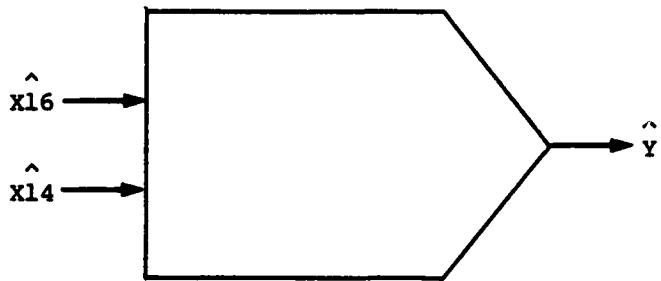
$$\hat{Y} = -0.45\hat{X16} - 0.64\hat{X14}$$

Where:

$$\hat{X} = (X-\overline{X})/\sigma_X$$

$$Y = \hat{Y}\sigma_Y + \overline{Y}$$

With (units in mils):

$\overline{X16}$ = 1.56		σ_{X16} = 0.56	
$\overline{X14}$ = 0.42		σ_{X14} = 0.06	
$\overline{Y}$ = 0.05		σ_Y = 0.05	
$\overline{E}$ = 0.006		$\overline{E}_P$ = 0.012	

Average Error = 12%

FIGURE 5.7: ALN DETERMINED FOR 0° EDM NOTCH DEPTH ESTIMATION
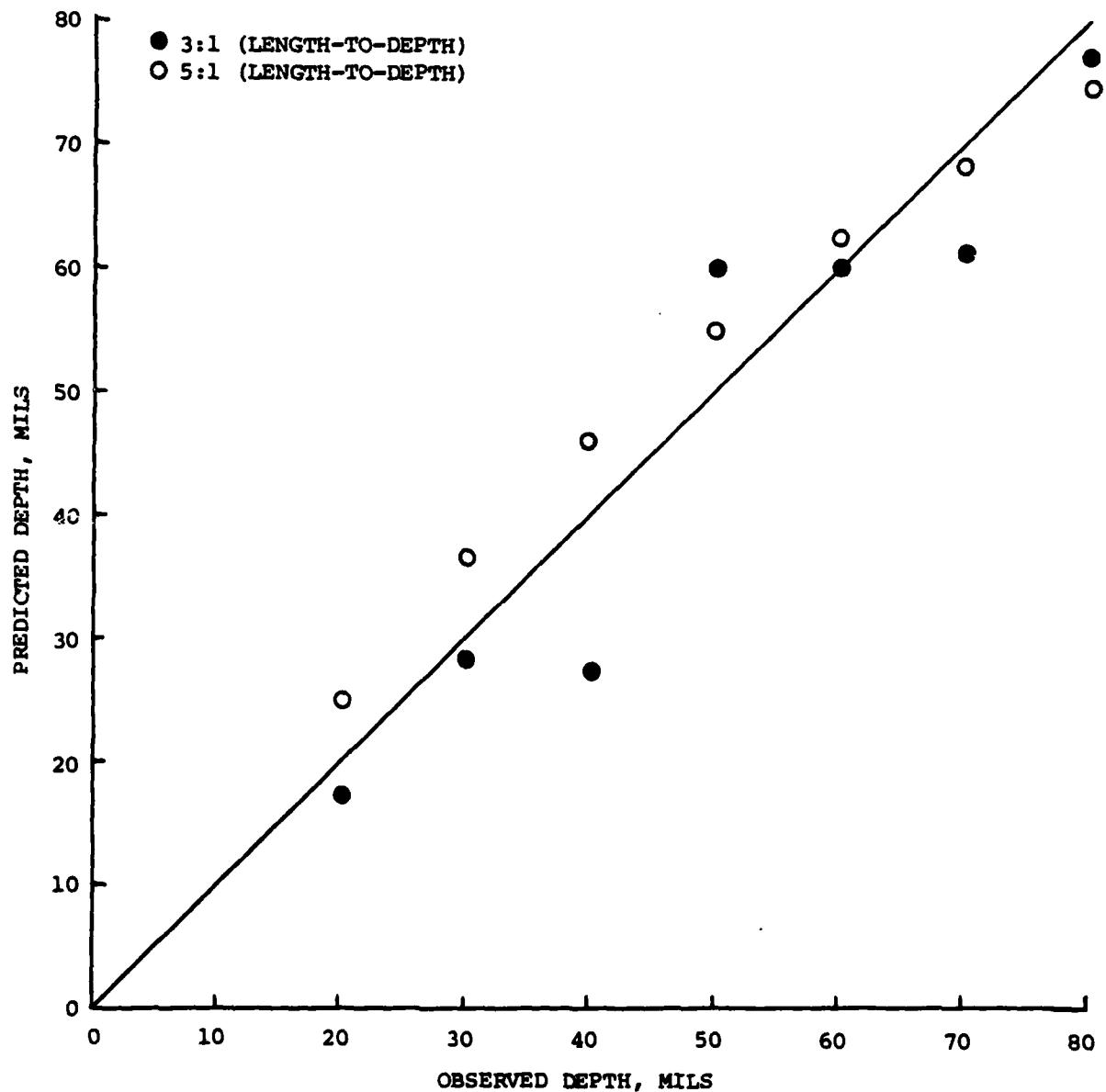
FIGURE 5.8:   COMPARISON OF OBSERVED AND PREDICTED DEPTHS,
0° EDM NOTCH DEFECTS

The same candidate feature set was used to determine the 0° EDM notch length model shown in Figure 5.9. The ALN model used two input variables, (1) the center of gravity of the power distribution over the array for the frequency band from 1.56 to 3.36 MHz, and (2) the ratio of power in Beams 3 through 7 to Beams 7 through 9 for the lowest frequency band. It is interesting to note that this second feature was also used in the ALN 0° depth model and was, therefore, an important sizing feature. The average RMS error on the length estimates was 36 mils (18%), with the predicted error on unseen data being 61 mils. A comparison of the observed and predicted lengths is provided in Figure 5.10 and again indicates very good agreement. In this case, the largest deviation of 88 mils corresponds to the 80x240-mil notch. The residuals for the remaining defects were generally between 20 to 30 mils.

The candidate features selected for the 30° EDM notch size characteristics are summarized in Table 5.4. Comparison of this feature list with that for the 0° notches reveals that the differences between the two feature sets are concerned with the type of defect response being parameterized. In the 0° case, the mode-converted ('SP') energy was used, while in the 30° notch case, the diffracted ('SS') response was used. This choice of energy type was consistent with the analyses performed earlier concerning the differences between the 0° and 30° EDM notch responses recorded in the linear array. The ALN model for predicting the depths of the 30° notches is shown in Figure 5.11. The input features for this model were both ratios of power observed in one beam to the total power: (1) beam 4 from 1.56 to 3.36 MHz, and (2) beam 3 from 2.81 to 3.36 MHz. The average RMS error was approximately 6 mils (12%) for the total sample. The predicted error for unseen observations was esti- mated to be 12 mils. These errors are quite consistent with those reported
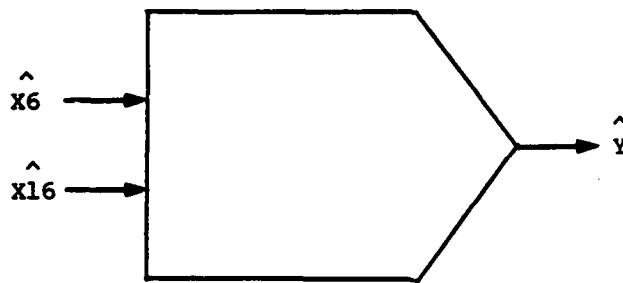
$$\hat{Y} = -0.64\hat{X6} - 0.52\hat{X16}$$

Where:

$$\hat{X} = (X - \overline{X})/\sigma_X$$

$$Y = \hat{Y}\sigma_Y + \overline{Y}$$

With (units in mils):

$\overline{X6}$ =	35.16	σ_{X6} =	3.79
$\overline{X16}$ =	1.56	σ_{X16} =	0.56
$\overline{Y}$ =	0.20	σ_Y =	0.096
$\overline{E}$ =	0.036	$\overline{E}_p$ =	0.061

Average Error = 18%

FIGURE 5.9: ALN DETERMINED FOR 0° EDM NOTCH LENGTH ESTIMATION
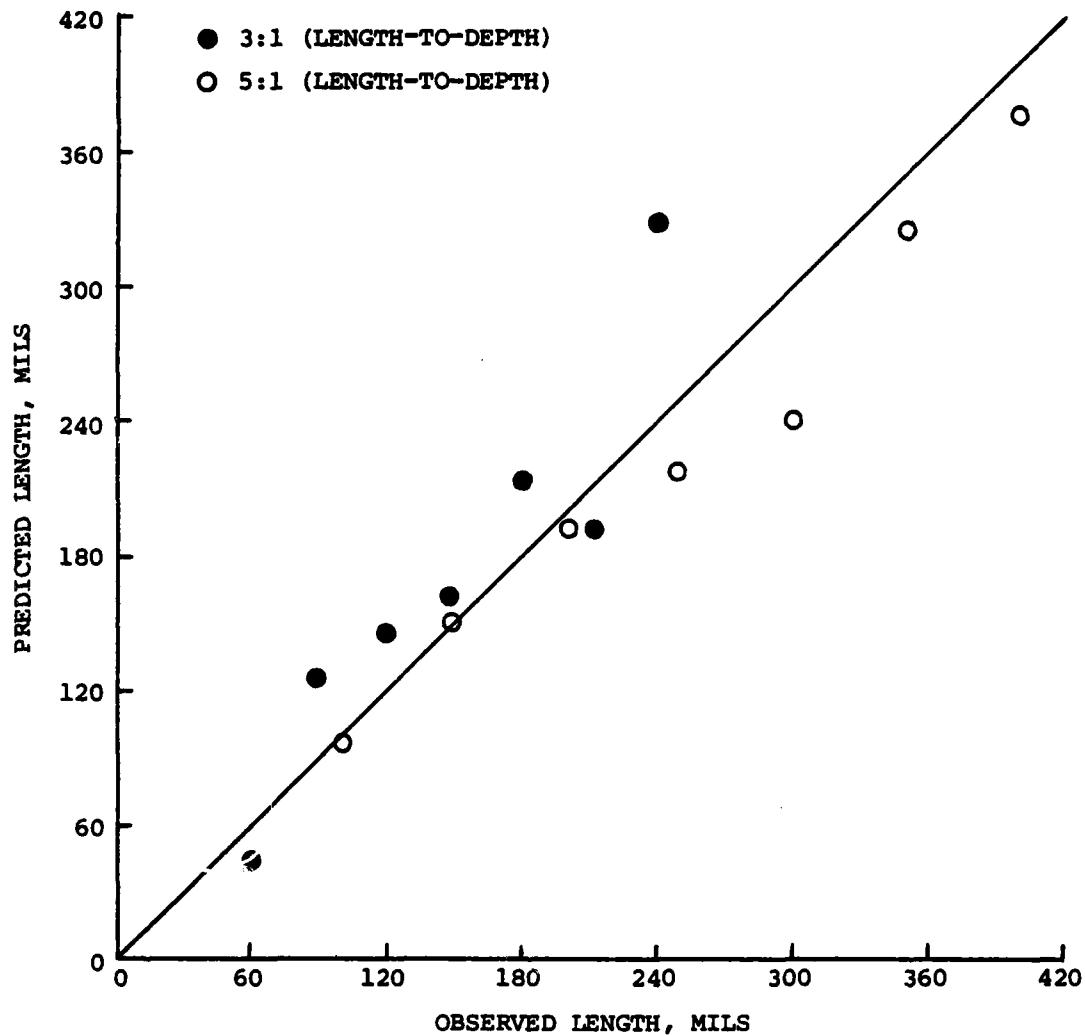
FIGURE 5.10: COMPARISON OF OBSERVED AND PREDICTED LENGTHS,
0° EDM NOTCH DEFECTS

TABLE 5.4: LIST OF CANDIDATE FEATURES FOR THE 30° EDM NOTCH DEFECTS

Feature Number	Description	
X3	Center of gravity of power distribution across array	(Band 1)
X4	Center of gravity of power distribution across array	(Band 2)
X5	Center of gravity of power distribution across array	(Band 3)
X6	Center of gravity of power distribution across array	(Band 4)
X7	Ratio of power in beams 2, 3, 4 to total power	(Band 1)
X8	Ratio of power in beams 3, 4, to total power	(Band 1)
X9	Ratio of power in beam 2 to total power	(Band 1)
X10	Ratio of power in beam 3 to total power	(Band 1)
X11	Ratio of power in beam 4 to total power	(Band 1)
X12	Ratio of power in beams 2, 3 to total power	(Band 1)
X13	Ratio of power in beams 1, 2 to beams 3, 4	(Band 1)
X14	Ratio of power in beams 2, 3 to beams 1, 2, 3	(Band 1)
X15	Ratio of power in beams 3, 4 to beams 1, 2, 3	(Band 1)
X16-X24	Same as features X7-X15	(Band 2)
X25-X33	Same as features X7-X15	(Band 3)
X34-X42	Same as features X7-X15	(Band 4)

Total power is defined as the sum of the individual power represented in beams 1 through 4.

Beam 1 is pulse-echo energy; beams 2 through 4 are diffracted energy ('SS').
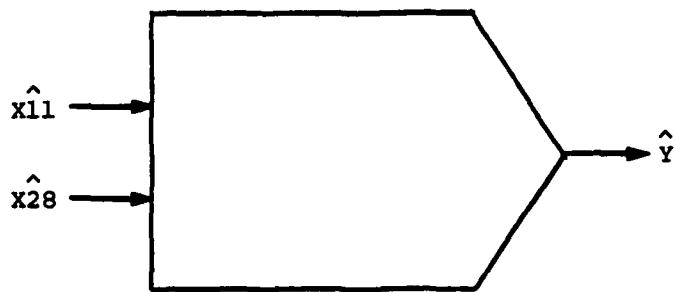
$$\hat{Y} = 0.58 X\hat{1}1 + 1.38 X\hat{2}8$$

Where:

$$\hat{X} = (X - \overline{X})/\sigma_X$$

$$Y = \hat{Y}\sigma_Y + \overline{Y}$$

With (units in mils):

$\overline{X11}$ = 0.18		σ_{X11} = 0.089	
$\overline{X28}$ = 0.18		σ_{X28} = 0.071	
$\overline{Y}$ = 0.05		σ_Y = 0.02	
$\overline{E}$ = 0.006		$\overline{E_P}$ = 0.012	

Average Error = 12%

FIGURE 5.11: ALN DETERMINED FOR 30° EDM NOTCH DEPTH ESTIMATION

earlier for the 0° EDM notches. A comparison of the observed and predicted depths for the 30° notch samples is shown in Figure 5.12. The deviations shown in this illustration are generally quite small.

The ALN model determined for the 30° EDM notch length estimate is shown in Figure 5.13 and used two input features: the ratio of the power in beams 3 and 4 to the total power in frequency band 2; and the ratio of beams 3 and 4 to beams 1, 2, and 3 for frequency band 3. The average RMS error in this case was 52 mils (26%) for the training data base. The larger errors reported in this case are probably related to the difficulty in obtaining a highly reliable indication of the scattered response at different array locations. Another possibility which deserves consideration is the exactness of the defect measurements, especially the orientation of the defect. A slight variation in the nominal 30° orientation could lead to significant changes in the scattered field, which may explain some of the deviations shown in the scatter plot, Figure 5.14.

5.3.2 Flat-Bottom Hole Size Estimation

The size estimation activities for the flat-bottom hole defects consisted of determining ALN models which could predict the diameter of the hole defect. The 0° and 30° orientations will be analyzed independently in this subsection.

The 0° FBH defects were inspected with the inboard transmitter, which emits a vertically-traveling compressional wave into the test block. Ultrasonic signals were recorded at receiver numbers 17 through 46, and a set of 8 beamed outputs was generated representing beam numbers 2 through 9, as shown in Table
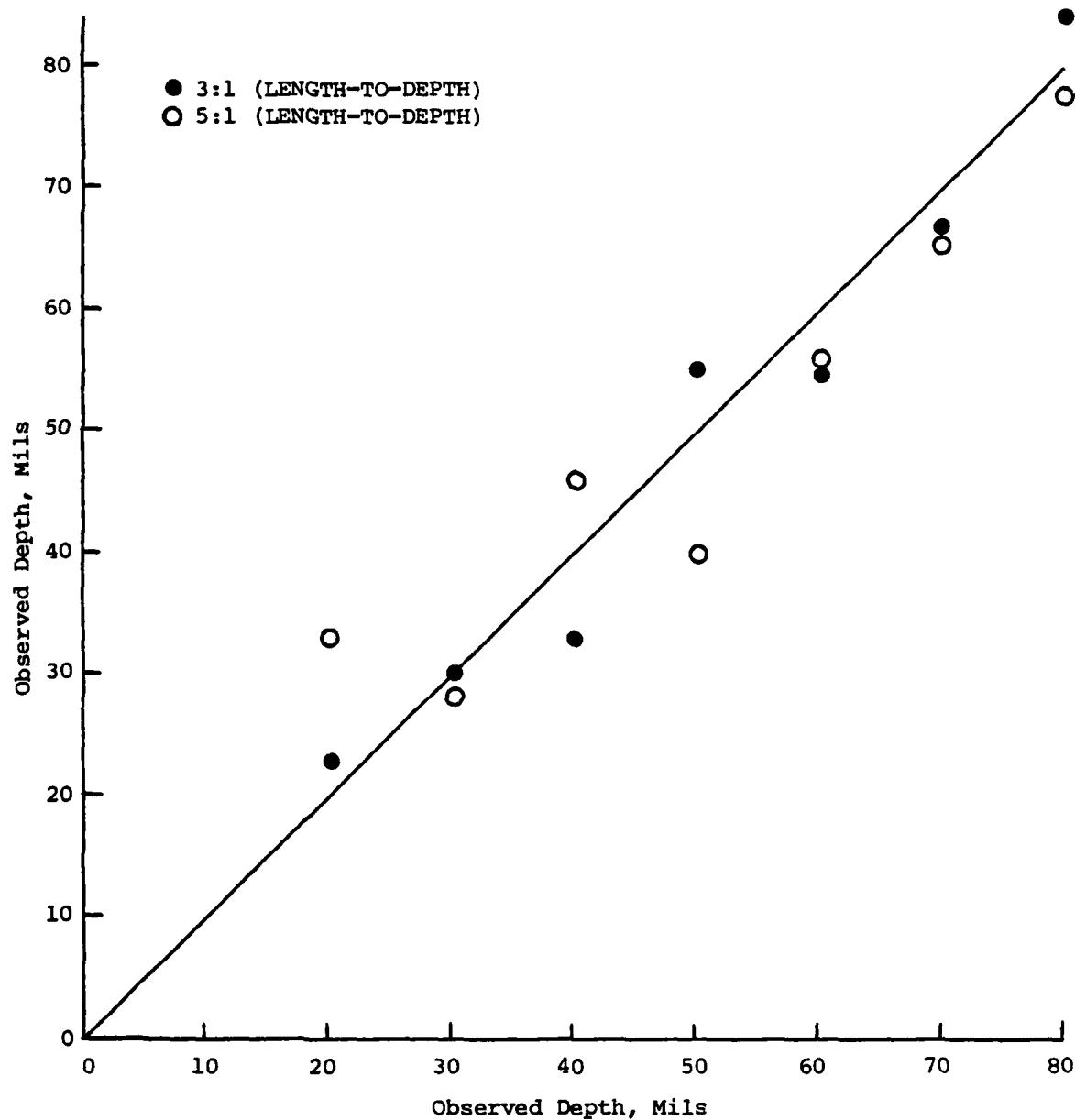
FIGURE 5.12: COMPARISON OF OBSERVED AND PREDICTED DEPTHS,
30° EDM NOTCH DEFECTS

5-25
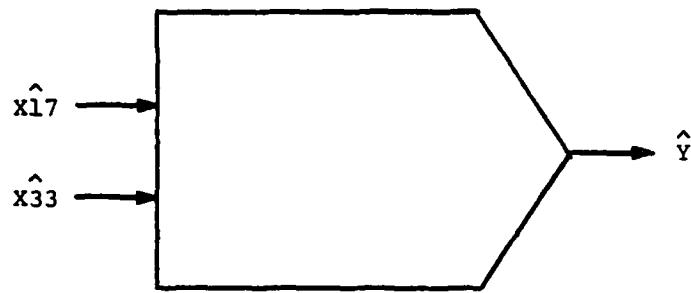
$$\hat{Y} = 1.45X\hat{1}7 - 0.95X\hat{3}3$$

Where:

$$\hat{X} = (X-\overline{X})/\sigma_X$$

$$Y = \hat{Y}\sigma_Y + \overline{Y}$$

With (units in mils):

$$\overline{X17} = 0.18 \qquad \sigma_{X17} = 0.063$$

$$\overline{X33} = 1.33 \qquad \sigma_{X33} = 0.86$$

$$\overline{Y} = 0.200 \qquad \sigma_Y = 0.096$$

$$\overline{E} = 0.052 \qquad \overline{E}_P = 0.071$$

Average Error = 26%

FIGURE 5.13: ALN DETERMINED FOR 30° EDM NOTCH LENGTH ESTIMATION
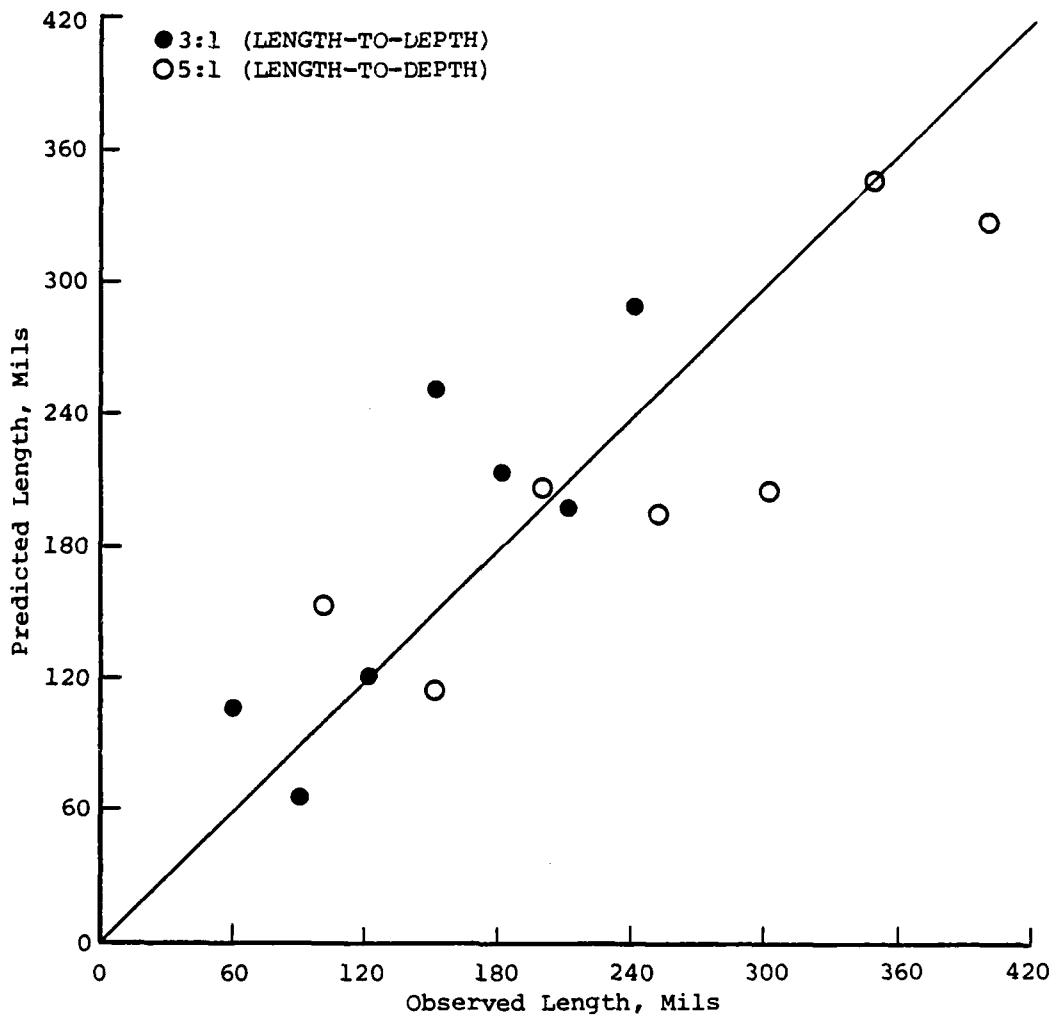
FIGURE 5.14: COMPARISON OF OBSERVED AND PREDICTED LENGTHS,
30° EDM NOTCH DEFECTS

5.1. A set of candidate features was extracted from these beamed waveforms and is shown in Table 5.5. It should be noted that the pulse-echo recording was not parameterized in this case because of the difficulty in separating the flaw-echo return from the front surface return of the test block. The ALN sizing model determined from this feature set is shown in Figure 5.15; it used features: the ratio of power in beams 5, 6, and 7 to the total power for the frequency band between 2.81 and 3.36 MHz; and the ratio of power in beams 7, 8, and 9 to the total power in the frequency band from 1.56 to 3.36 MHz. The size of the 0° flat-bottom hole diameters ranged from 3/64 inch to 16/64 inch. The two smaller defect echoes (1/64 inch and 2/64 inch) could not be reliably detected in this case and were not used in the modeling exercise. The average RMS error was less than 1/64 inch (9%) for the training data base and is predicted to be approximately 2/64 inch for unseen data. A scatter plot of the observed diameters and those predicted by the ALN model is shown in Figure 5.16; it indicates that the model performed well, with the deviations being quite small.

The 30° FBH defects were insonified with the outboard transmitter, and waveforms were recorded at receivers 23 through 47 within the linear array. A set of six beamformed composites was formed using these recordings, and features were measured from the beamformed signals. A list of the candidate features used in the ALN FBH diameter modeling exercise is shown in Table 5.6. The ALN model resulting from the training data base of 30° FBH defects, with diameters ranging from 3/64 inch to 16/64 inch, is presented in Figure 5.17. Two features were selected by the ALN: the ratio of power in beams 2, 3, and 4 to the total power for frequency band 1; and the same ratio for frequency band 2. The average RMS error in this model was approximately 1/64 inch (11%) and

TABLE 5.5:   LIST OF CANDIDATE FEATURES FOR THE 0°
FLAT-BOTTOM HOLE DEFECTS

Feature Number	Description	
X3	Center of gravity of power distribution across array	(Band 1)
X4	Center of gravity of power distribution across array	(Band 2)
X5	Center of gravity of power distribution across array	(Band 3)
X6	Center of gravity of power distribution across array	(Band 4)
X7	Ratio of power in beams 2, 3, 4 to total power	(Band 1)
X8	Ratio of power in beams 5, 6, 7 to total power	(Band 1)
X9	Ratio of power in beams 7, 8, 9 to total power	(Band 1)
X10	Ratio of power in beams 4, 5, 6 to total power	(Band 1)
X11	Ratio of power in beams 3, 4, 5 to total power	(Band 1)
X12	Ratio of power in beams 4, 5, 6 to beams 7, 8, 9	(Band 1)
X13	Ratio of power in beams 2, 3 to beams 3, 4	(Band 1)
X14-X20	Same as features X7-X13	(Band 2)
X21-X27	Same as features X7-X13	(Band 3)
X28-X34	Same as features X7-X13	(Band 4)

Total power is defined as the sum of the individual power represented in beams
2 through 9.

Beams 1 through 9 are diffracted energy ('PP').
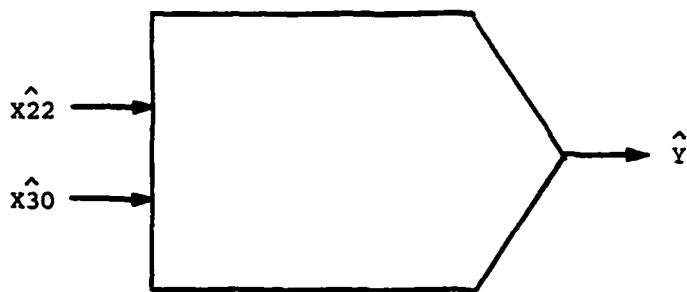
$$\hat{Y} = 0.32X\hat{2}2 - 0.93X\hat{3}0$$

Where:

$$\hat{X} = (X-\overline{X})/\sigma_X$$

$$Y = \hat{Y}\sigma_Y + \overline{Y}$$

With (units in 64th's of an inch):

$\overline{X22} = 0.52$ $\sigma_{X22} = 0.069$

$\overline{X30} = 0.20$ $\sigma_{X30} = 0.073$

$\overline{Y} = 9.50$ $\sigma_Y = 4.03$

$\overline{E} = 0.86$ $\overline{E_P} = 2.30$

Average Error = 9%

FIGURE 5.15: ALN DETERMINED FOR 0° FLAT-BOTTOM-HOLE DIAMETER ESTIMATION
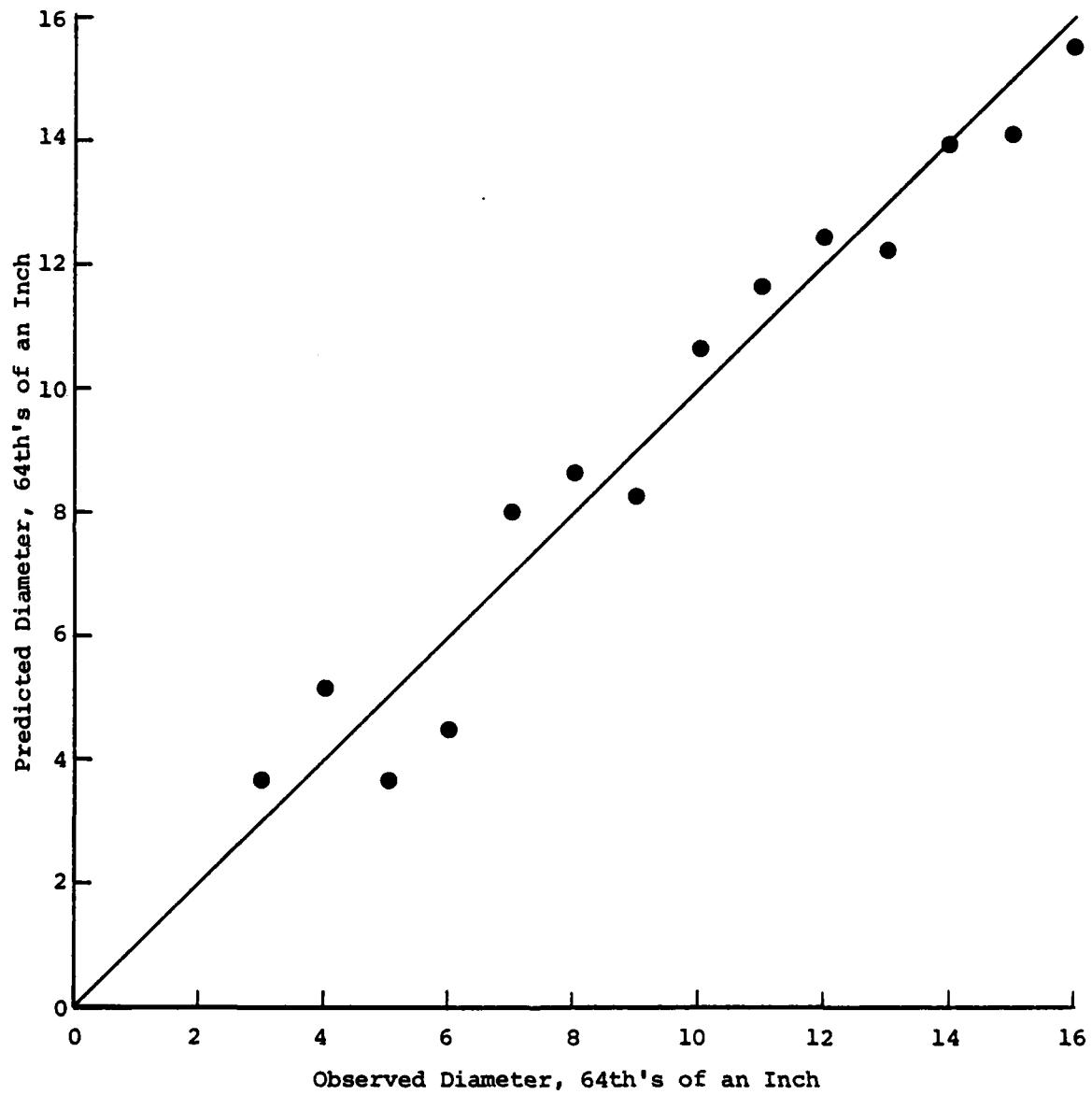
FIGURE 5.16: COMPARISON OF OBSERVED AND PREDICTED DIAMETERS, 0° FLAT-BOTTOM-HOLE DEFECTS

TABLE 5.6: LIST OF CANDIDATE FEATURES FOR THE 30°
FLAT-BOTTOM HOLE DEFECTS

Feature Number	Description	
X3	Center of gravity of power distribution across array	(Band 1)
X4	Center of gravity of power distribution across array	(Band 2)
X5	Center of gravity of power distribution across array	(Band 3)
X6	Center of gravity of power distribution across array	(Band 4)
X7	Ratio of power in beams 1, 2, 3 to total power	(Band 1)
X8	Ratio of power in beams 4, 5, 6 to total power	(Band 1)
X9	Ratio of power in beams 2, 3, 4 to total power	(Band 1)
X10	Ratio of power in beams 3, 4, 5 to total power	(Band 1)
X11	Ratio of power in beams 1, 2 to beams 5, 6	(Band 1)
X12	Ratio of power in beams 2, 3 to beams 5, 6	(Band 1)
X13	Ratio of power in beams 1, 2 to beams 3, 4	(Band 1)
X14-X20	Same as features X7-X13	(Band 2)
X21-X27	Same as features X7-X13	(Band 3)
X28-X34	Same as features X7-X13	(Band 4)

Total power is defined as the sum of the individual power represented in beams
1 through 6.

Beam 1 is pulse-echo energy; beams 2 through 6 are diffracted energy ('SS').
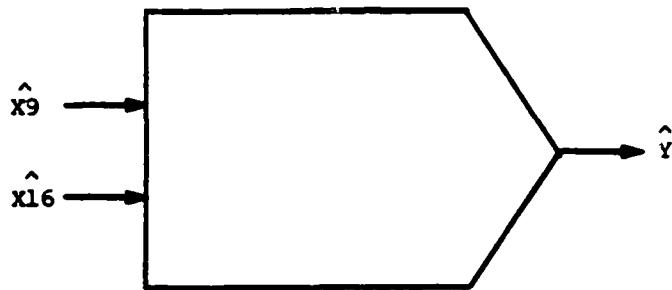
$$\hat{Y} = 0.42\hat{X9} + 0.66\hat{X16}$$

Where:

$$\hat{X} = (X - \overline{X})/\sigma_X$$

$$Y = \hat{Y}\sigma_Y + \overline{Y}$$

With (units in 64th's of an inch):

$\overline{X9}$ = 0.67		σ_{X9} = 0.098	
$\overline{X16}$ = 0.57		σ_{X16} = 0.077	
$\overline{Y}$ = 9.50		σ_Y = 4.03	
$\overline{E}$ = 1.09		$\overline{E_p}$ – 2.38	

Average Error = 11%

FIGURE 5.17: ALN DETERMINED FOR 30° FLAT-BOTTOM-HOLE DIAMETER ESTIMATION

agrees quite well with the error obtained from the 0° FBH defects. A comparison of the ALN predicted diameters and the true diameters is shown in Figure 5.18.

5.3.3 Round-Bottom Hole Size Estimation

The size estimation activities for the round-bottom-hole defects were handled in the same fashion as those presented earlier for the other defect categories; however, the amount of data which was recorded from the RBH defects was significantly less than that used in the previous exercises because of the difficulties associated with detecting any scattered energy. The waveforms obtained from these defects were obtained from both the inboard and outboard transmitters in the pulse-echo mode. Efforts to record scattered signals at other locations within the array were not successful even when a large number of temporal averages (100) was formed. This observation was also made by BNW in their initial efforts to collect data from these defects (Lemon, et al., 1980).

Two waveforms were collected for each defect, one from each of the T/R groups. Features were extracted from these recordings and are shown in Table 5.7. The ALN model for the 0° RBH defect diameter estimation is shown in Figure 5.19. Two input variables were used in this model, the total power in the frequency band from 1.56 to 2.10 MHz for the outboard recording and the frequency at which the 1/3 power level was attained at the inboard recording. The average RMS error for the model is 1.55/64 inch (16%). The comparison between the true and predicted 0° RBH diameter values is shown in Figure 5.20.
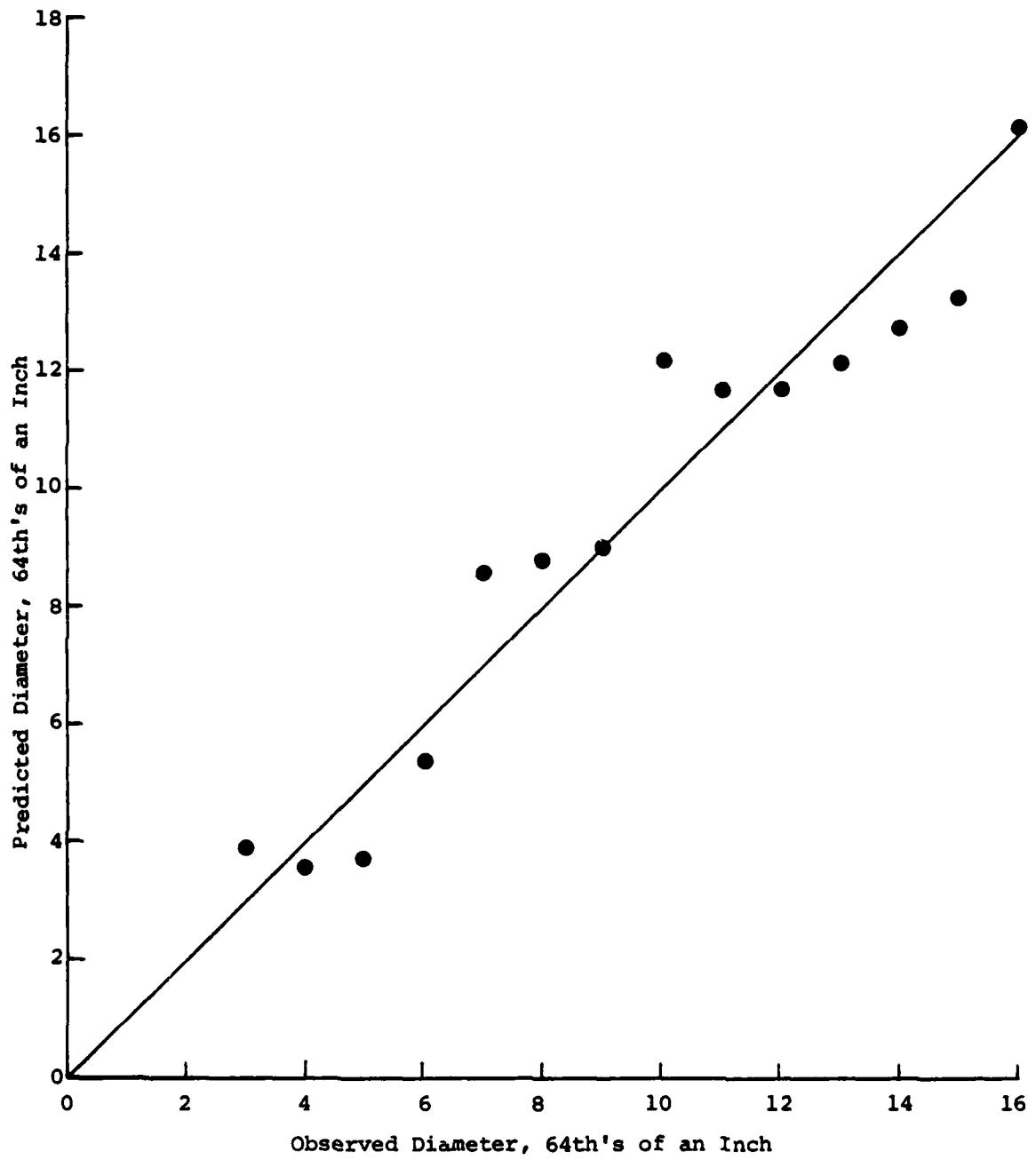
FIGURE 5.18:   COMPARISON OF OBSERVED AND PREDICTED DIAMETERS,
30° FLAT-BOTTOM-HOLE DEFECTS

TABLE 5.7: LIST OF CANDIDATE FEATURES FOR THE 0°
AND 30° ROUND-BOTTOM HOLE DEFECTS

Feature Number	Description	
X4	Ratio of power in band 1 to band 2	(Outboard T/R)
X5	Ratio of power in band 1 to band 3	(Outboard T/R)
X6	Ratio of power in band 2 to band 3	(Outboard T/R)
X7	Ratio of power in band 1 to band 2	(Inboard T/R)
X8	Ratio of power in band 1 to band 3	(Inboard T/R)
X9	Ratio of power in band 2 to band 3	(Inboard T/R)
X10	Ratio of inboard power to outboard power	(Band 1)
X11	Ratio of inboard power to outboard power	(Band 2)
X12	Ratio of inboard power to outboard power	(Band 3)
X13	Total power in band 1	(Outboard T/R)
X14	Total power in band 2	(Outboard T/R)
X15	Total power in band 3	(Outboard T/R)
X16	Total power in band 1	(Inboard T/R)
X17	Total power in band 2	(Inboard T/R)
X18	Total power in band 3	(Inboard T/R)
X19	Ratio of inboard power to outboard power	(Band 4)
X20	Frequency at which 1/3 power point is reached	(Outboard T/R)
X21	Frequency at which 1/3 power point is reached	(Inboard T/R)
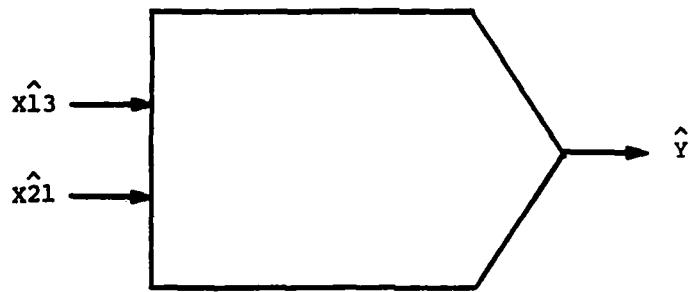
$$\hat{Y} = 0.45X\hat{1}3 + 1.13X\hat{2}1$$

Where:

$$\hat{X} = (X-\overline{X})/\sigma_X$$

$$Y = \hat{Y}\sigma_Y + \overline{Y}$$

With (units in 64th's of an inch):

$\overline{X13}$	= 0.024	σ_{X13}	= 0.016
$\overline{X21}$	= 29.93	σ_{X21}	= 2.55
$\overline{Y}$	= 9.50	σ_Y	= 4.03
$\overline{E}$	= 1.55	$\overline{E_p}$	= 2.59

Average Error = 16%

FIGURE 5.19: ALN DETERMINED FOR 0° ROUND-BOTTOM-HOLE DIAMETER ESTIMATION
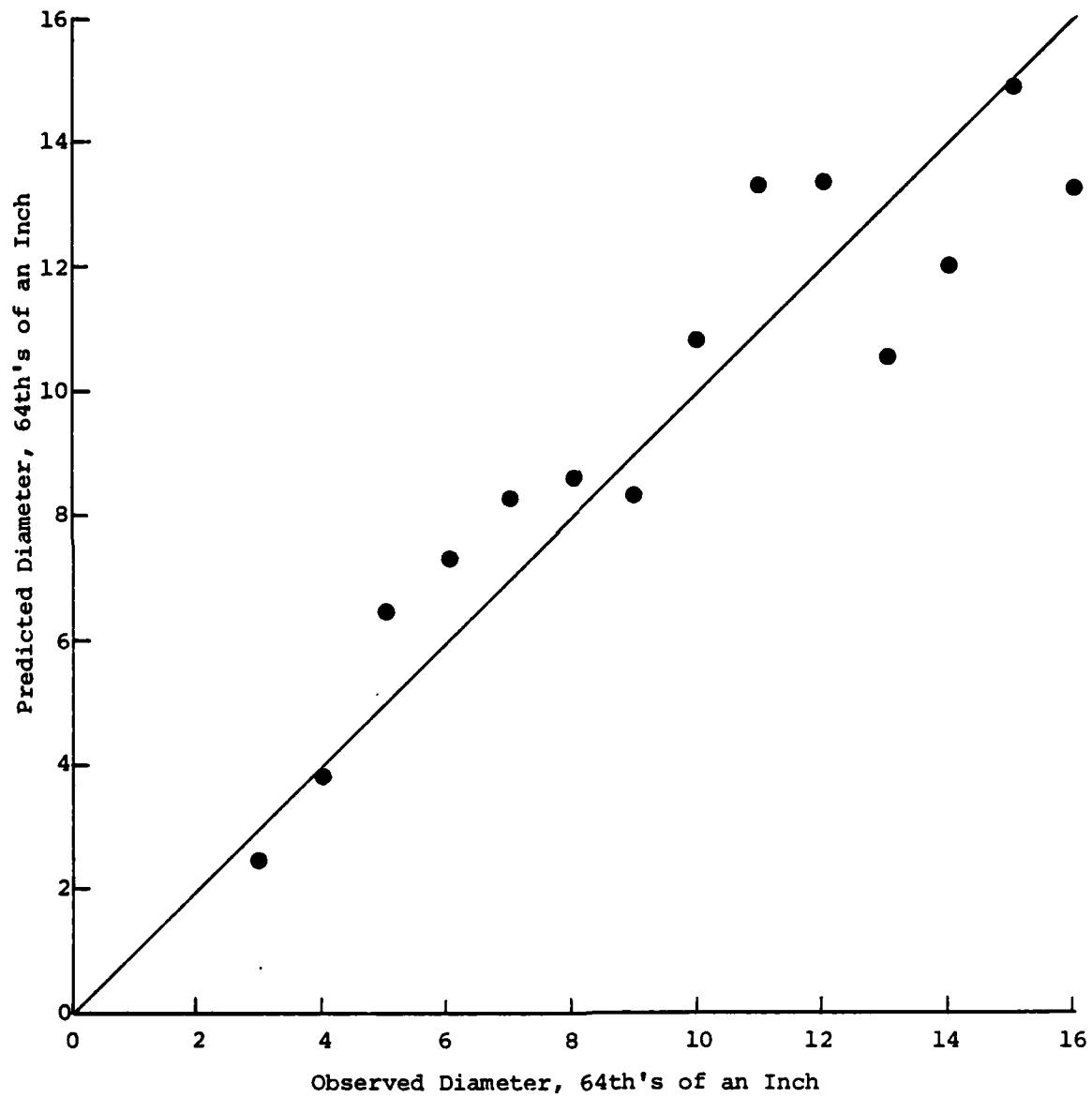
FIGURE 5.20: COMPARISON OF OBSERVED AND PREDICTED DIAMETERS,
0° ROUND-BOTTOM-HOLE DEFECTS

The same feature set shown in Table 5.7 was used to determine the ALN model for the 30° RBH diameters. This model is presented in Figure 5.21. It used two input features, the ratios of the inboard and outboard powers in band 2 and in band 4. The average RMS error for the 30° RBH defects is 1.31/64 inch (13%), which is quite comparable to that of the 0° RBH flaws. A scatter plot of the observed and predicted values is shown in Figure 5.22.

5.4 SUMMARY

The results presented in this chapter demonstrate that the characterization of a defect signal can be obtained through the use of signal processing and ALN modeling techniques. In general, the results are in good agreement with the known defect characteristics. The advantages offered by this approach will become more evident in the next chapter, where a series of conventional pulse-echo images is presented.
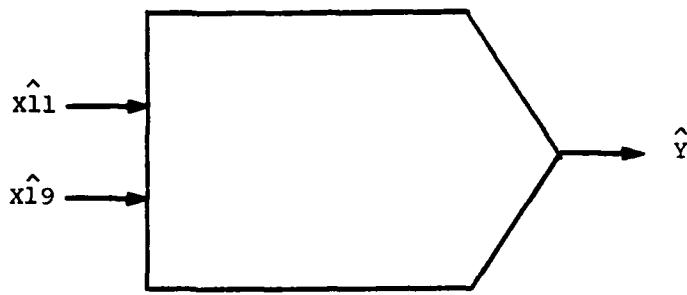
$$\hat{Y} = 0.11\hat{X11} - 1.03\hat{X25}$$

Where:

$$\hat{X} = (X-\overline{X})/\sigma_X$$

$$Y = \hat{Y}\sigma_Y + \overline{Y}$$

With (units in 64th's of an inch):

$\overline{X11}$	=	0.99	σ_{X11} =	0.12
$\overline{X19}$	=	24.0	σ_{X19} =	18.2
$\overline{Y}$	=	9.85	σ_Y =	3.98
$\overline{E}$	=	1.31	$\overline{E_p}$ =	2.52

Average Error = 13%

FIGURE 5.21: ALN DETERMINED FOR 30° ROUND-BOTTOM-HOLE DIAMETER ESTIMATION
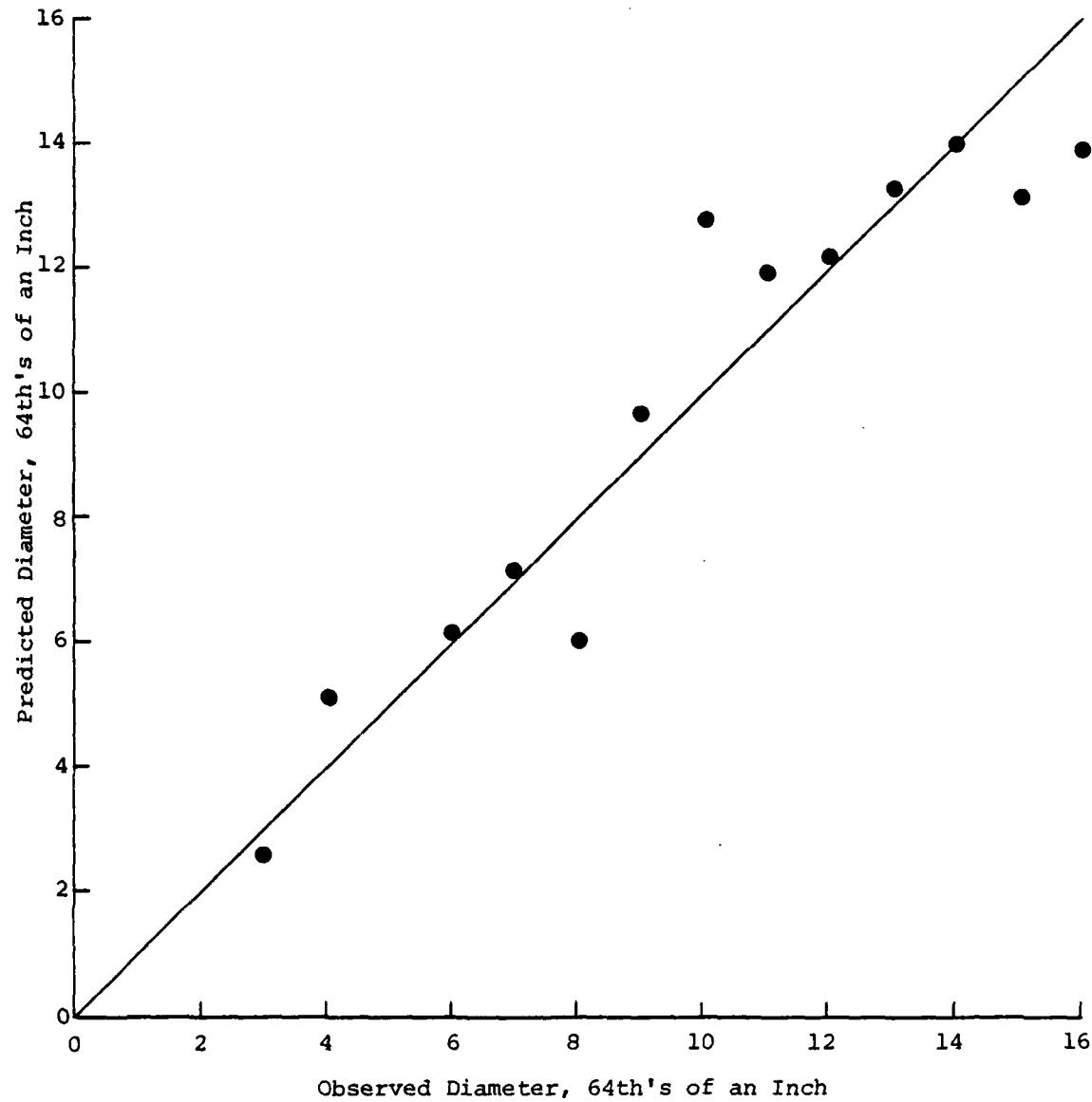
FIGURE 5.22:   COMPARISON OF OBSERVED AND PREDICTED DIAMETERS,
30° ROUND-BOTTOM-HOLE DEFECTS

6. ULTRASONIC IMAGING

6.1 CONVENTIONAL PULSE-ECHO IMAGING

Pulse-echo isometric images were made for each of the test blocks described in Chapter 3 by Battelle Pacific Northwest Laboratories using the ultrasonic imaging system developed for the Electric Power Research Institute (Becker, et al., 1979). The outboard transmitter/receiver was used to image the EDM notch defects and the 30° hole defects. The inboard transmitter/receiver was used to image the 0° hole defects.

The procedures used in forming these images involved the establishment of a reference echo amplitude, so that the amplitudes of the echoes obtained from the defects of interest in this study could be measured relative to this reference. A 3/64 inch diameter FBH located in a #3 Hitt block made of 4310 steel from an ASTM test block set was used as the reference reflector. A flat 3/8 inch x 3/8 inch, 2.25 MHz transducer was used in conjunction with a KB 6000 flaw detection system so that the relative measurements could be obtained directly in dB. The returned echo height was adjusted to correspond to 80% of the full screen height and was set as the 0 dB reference point. The echo from each defect in the data base was then obtained by maximizing the return using the scanning bridge. The maximum return was then adjusted until the echo was at 80% full screen height of the KB 6000 and the gain setting was recorded.

The results of these calculations are shown in Table 6.1. It is interesting to note that in many cases the defect could not be located using the

TABLE 6.1: RELATIVE ECHO AMPLITUDES FROM TEST BLOCK DEFECTS
Numbers are dB gain relative to the amplitude of
an ASTM 3/64 FBH

Defect diameter/depth	FBH 0° Blocks 2A & 2B	FBH 30° Blocks 3A & 3B	RBH 0° Blocks 4A & 4B	RBH 30° Blocks 5A & 5B	EDM 0°, 3:1 Block 6A	EDM 0°, 5:1 Block 6B	EDM 30°, 3:1 Block 7A	EDM 30°, 5:1 Block 7B
1.					+14			+11
2.	+ 7				+11	+13	+10	+ 9
3.	+ 4		+11		+ 6	+11	+ 6	+ 2
4.	- 2		+10		+ 6	+ 8	+ 4	- 2
5.	- 5		+ 5		+ 3	+ 6	0	- 4
6.	- 8		+ 7		0	+ 2	0	- 6
7.	-11		+ 6		- 2	0	- 3	- 7
8.	-13		+ 3		- 5	0	- 3	- 7
9.	-13	- 9	- 4	+ 2				
10.	-15	-10	- 2	+ 4				
11.	-16	-12	- 6	- 2				
12.	-17	-14	- 8	- 1				
13.	-15	-14	- 2	0				
14.	-18	-16	- 9	- 2				
15.	-19	-17	- 7	+ 4				
16.	-19	-18	- 7	- 1				

Hole diameter in 1/64 inches, or notch depth in 10 mil units.

procedures outlined above. Defects with effective echo amplitudes smaller (positive entries in Table 6.1) than the reference reflector amplitude could not be imaged because the acoustic noise inherent in the test blocks exceeded the write level of the imaging system. One point worth noting is the fact that the #3 FBH sample (3/64 inch diameter) echo is 4 dB below the reference standard, which is primarily due to the higher attenuation properties of the 4340 test blocks.

Isometric images of the 12 test blocks are shown in Figures 6.1 through 6.12. Images of the 30° FBH defects of diameter 1/64 inch to 8/64 inch and of the 0° and 30° RBH defects of diameters 1/64 inch to 8/64 inch could not be obtained because of reasons identified above. A detailed examination of these images reveals some rather interesting properties which will be discussed below.

A visual comparison of the 0° FBH images shown in Figures 6.1 and 6.2 does not appear to contain any information related to the relative size of the individual defects, even though the diameters of defects range from 4/64 inch to 16/64 inch. The area of the image pattern does not indicate any significant variation in size from defect to defect. This phenomenon is probably related to the beam spread of the transmitting mechanism, which distorts the effective area of the region being insonified. Another comparison between Figure 6.2 (0° FBH) and Figure 6.4 (30° FBH) appears to offer some distinctions which could be useful for orientation estimates, but no sizing information could be obtained in either illustration. The same general conclusions stated above for the FBH samples apply to the RBH images shown in Figures 6.5 through 6.8. The images shown for the EDM notch defects (Figures 6.9 through 6.12) are rather interesting in that the shapes of these reflectors are quite compatible
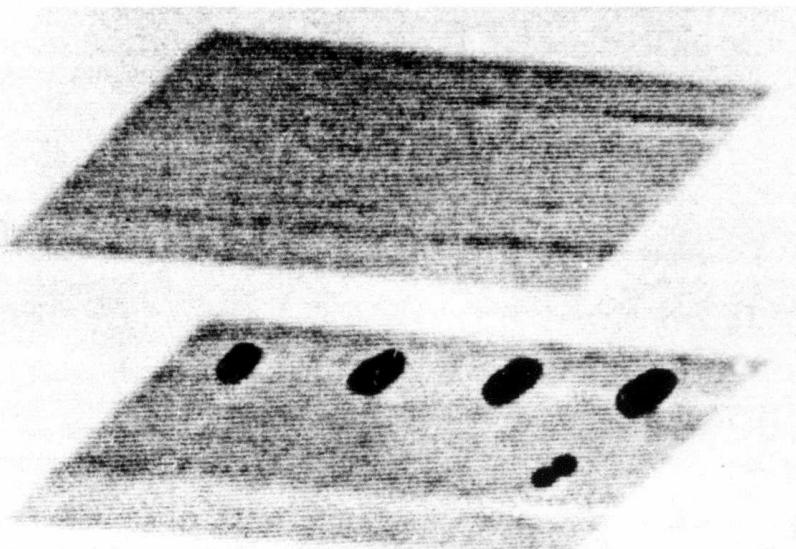
FIGURE 6.1: ISOMETRIC IMAGE OF BLOCK 2A, FLAT-BOTTOM HOLES, 0°, 1/64-8/64" DIAMETERS. Gain = 37 dB. At 37 dB gain, the 4/64" FBH is at the write-threshold of 40% full screen height.
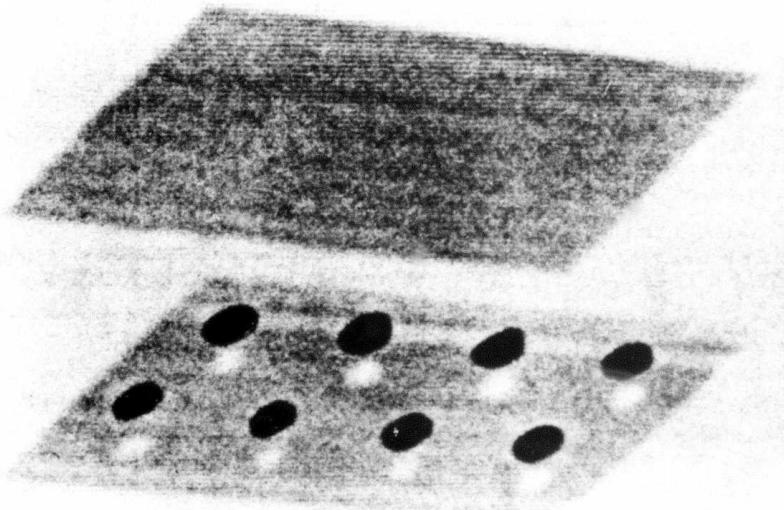

FIGURE 6.2: ISOMETRIC IMAGE OF BLOCK 2B, FLAT-BOTTOM HOLES, 0°, 10/64-16/64" DIAMETERS. Gain = 29 dB.
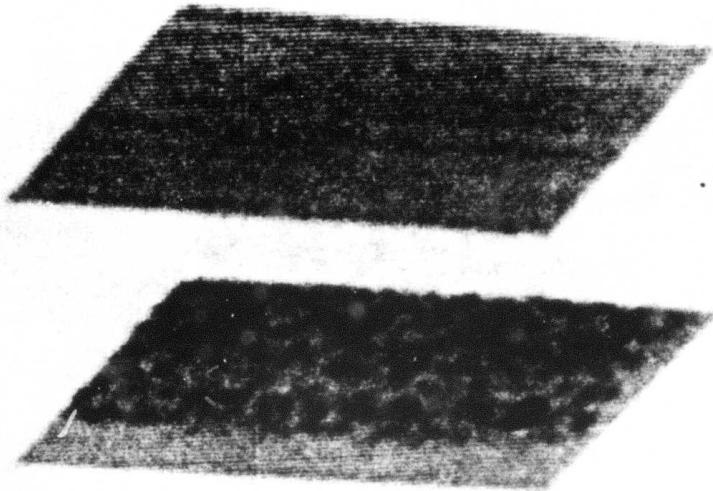
FIGURE 6.3: ISOMETRIC IMAGE OF BLOCK 3A, FLAT-BOTTOM HOLES, 30°, 1/64-8/64" DIAMETERS. Gain = 50 dB.
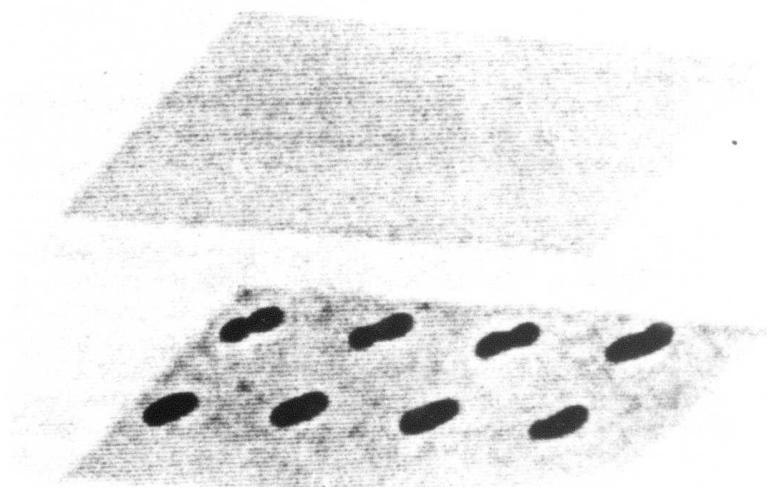
FIGURE 6.4: ISOMETRIC IMAGE OF BLOCK 3B, FLAT-BOTTOM HOLES, 30°, 9/64-16/64" DIAMETERS. Gain = 46 dB.

The level of intrinsic acoustic reflectors in this block was equal in magnitude to the reflections from the round-bottom holes. Consequently, an ultrasonic image could not be obtained.

FIGURE 6.5: TEST BLOCK 4A, ROUND-BOTTOM HOLES, 0°, 1/64-8/64" DIAMETER.
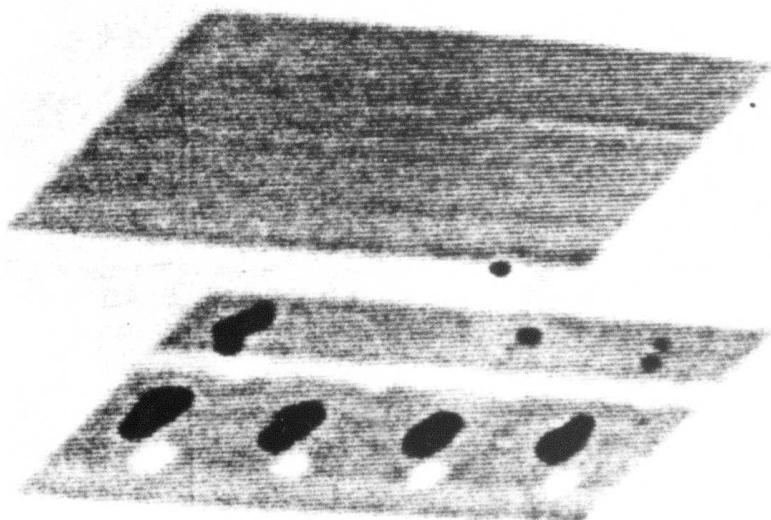
FIGURE 6.6: ISOMETRIC IMAGE OF BLOCK 4B, ROUND-BOTTOM HOLES, 0°, NOMINAL 9/64-16/64" DIAMETER. Gain = 73 dB.
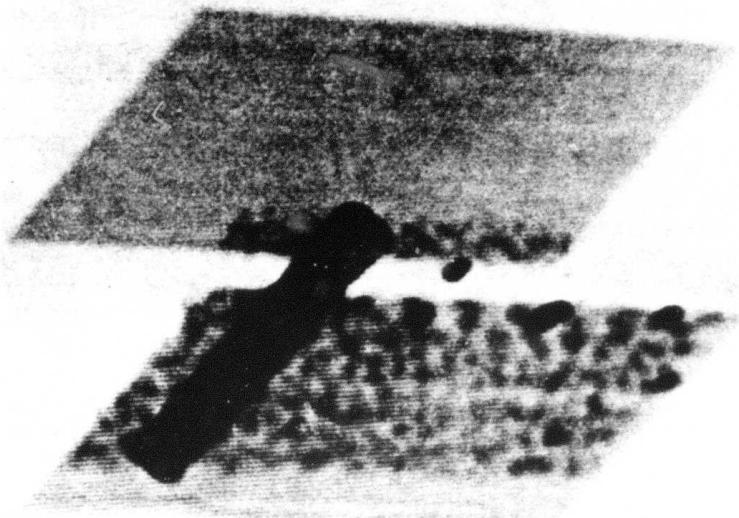
FIGURE 6.7: ISOMETRIC IMAGE OF BLOCK 5A, ROUND-BOTTOM HOLES, 30°, NOMINAL 1/64-8/64" DIAMETER. Gain = 58 dB. The dark band on the left is from side lobe energy echoing from the back corner of the block.
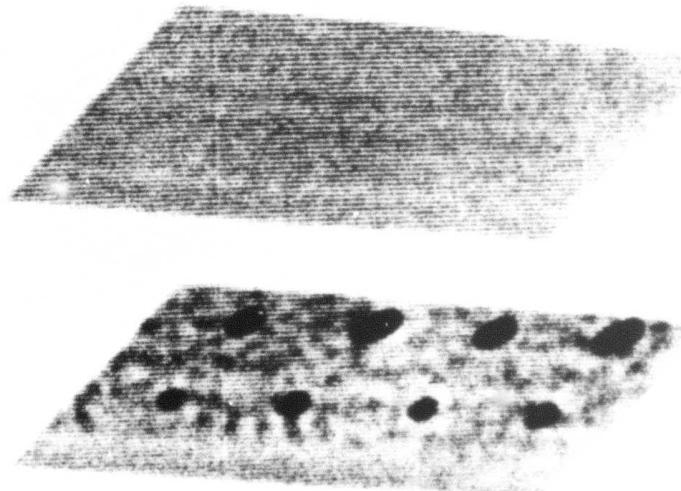
FIGURE 6.8: ISOMETRIC IMAGE OF BLOCK 5B, ROUND-BOTTOM HOLES, 30°, NOMINAL 9/64-16/64" DIAMETER. Gain = 49 dB.
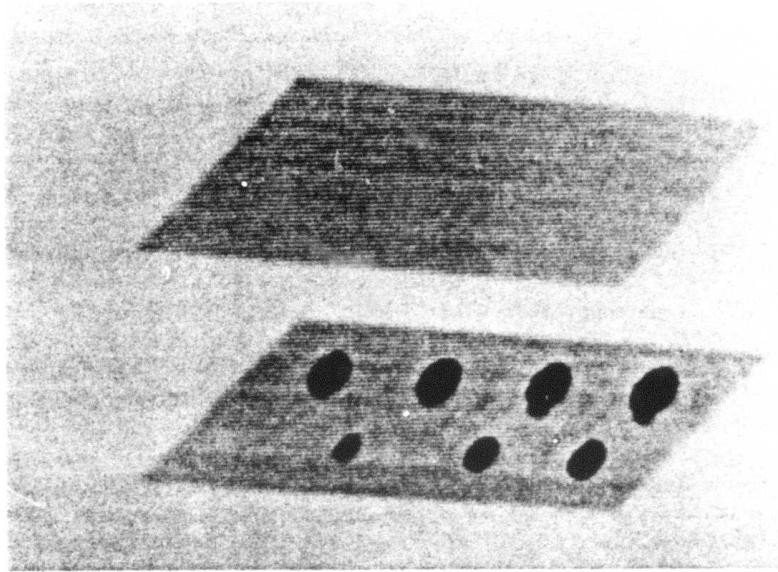
FIGURE 6.9: ISOMETRIC IMAGE OF BLOCK 6A, EDM NOTCHES, 0°, 3:1
ASPECT RATIO, 10 TO 80 MILS DEEP. Gain = 40 dB.
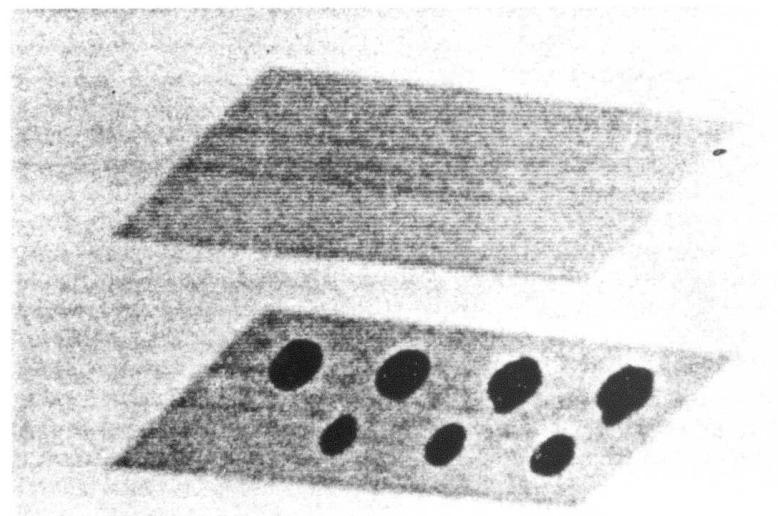
FIGURE 6.10: ISOMETRIC IMAGE OF BLOCK 6B, EDM NOTCHES, 0°, 5:1
ASPECT RATIO, 10 TO 80 MILS DEEP. Gain = 40 dB.
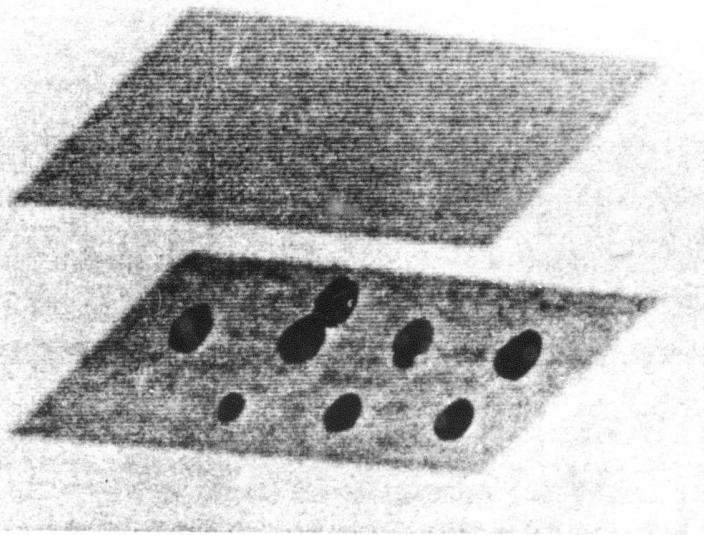
FIGURE 6.11:   ISOMETRIC IMAGE OF BLOCK 7A, EDM NOTCHES, 30°, 3:1
              ASPECT RATIO, 10 TO 80 MILS DEEP. Gain = 40 dB.
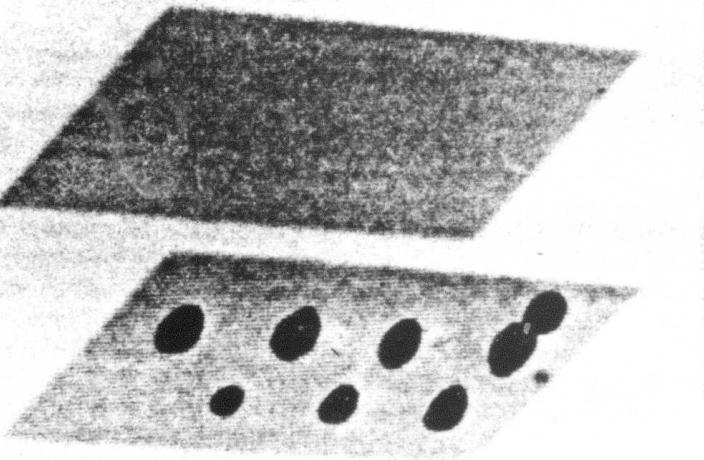
FIGURE 6.12:   ISOMETRIC IMAGE OF BLOCK 7B, EDM NOTCHES, 30°, 5:1
              ASPECT RATIO, 10 TO 80 MILS DEEP. Gain - 40 dB.

with those presented for the hole samples, even though the geometrical proper-
ties of the defect classes are quite different.

It is evident that the results obtained from conventional pulse-echo imaging
techniques can be improved in a significant fashion through the combination of
signal processing and ALN techniques presented in the previous chapter. The
improvements are related to both the defect detection and characterization
tasks. For example, the FBH and RBH defects could be detected quite consis-
tently down to diameters of 3/64 inch, while the threshold for the imaging
system was as high as 11/64 inch in diameter. The images obtained from the
pulse-echo system contain very limited information for a reliable method of
defect classification, orientation, or size estimation. The results presented
in the previous chapter address each of these characterization requirements
with a higher degree of certainty; however, improvements in the imaging capa-
bilities can also be obtained by the introduction of more sophisticted tech-
niques. A set of improved imaging techniques will be described and evaluated
in the subsection which follows.

6.2 Enhanced Images

The defect images shown in Figures 6.1 through 6.12 were obtained by BNW using
a conventional pulse-echo imaging technique. The procedures used during the
exercise described above were to form a black/white representation, where the
black signifies a detection and the white signifies no detection. Since the
modified system described in this report possesses the capability of recording
the raw waveforms as well as applying temporal averaging to improve the

signal-to-noise ratio, it was decided to repeat the imaging exercise for a few defects in the data base. The procedures employed in this exercise are outlined below.

The scanning bridge was used manually to position the appropriate transmitter over the defect until the maximum amplitude response was obtained. Once this position was located, the operator informed the ALN 4000 of this fact, and the ALN 4000 moved the transducer 0.5 inch in the X and Y directions and initiated its acquisition of the ultrasonic waveforms. The defect was scanned over a one-square-inch area, and data were recorded with a resolution of 0.1 inch in both directions. This scanning pattern is illustrated in Figure 6.13.

A total of 121 waveforms was obtained for each defect scanned during these operations. The waveforms were written to magnetic tape cartidges after a temporal average of 10 individual recordings was obtained. The contents of the tape cartridge were then transferred to the Data General Eclipse computer system for plotting and off-line analysis purposes.

Using software packages resident on the off-line computer, a sequence of three-dimensional plots was made of the rectified recordings. An example of this output for a 20 x 100 mil 0° EDM notch is shown in Figure 6.14, and for an 80 x 400 mil 0° EDM notch in Figure 6.15. The waveforms presented in these two figures represent five positions along the X-axis, with the ten waveforms in each grouping corresponding to the ten Y-axis positions. The amplitude values indicated on these plots have been normalized by the maximum amplitude within a given sequence so that the relative change in strength as a function of position can be seen. It should be noted that the amplitude does decay

FIGURE 6.13: SCANNING GRID USED TO FORM IMPROVED DEFECT IMAGES

X=-0.2

X=-0.1

Front Surface

Defect

X=0.0

X=0.1

X=0.2
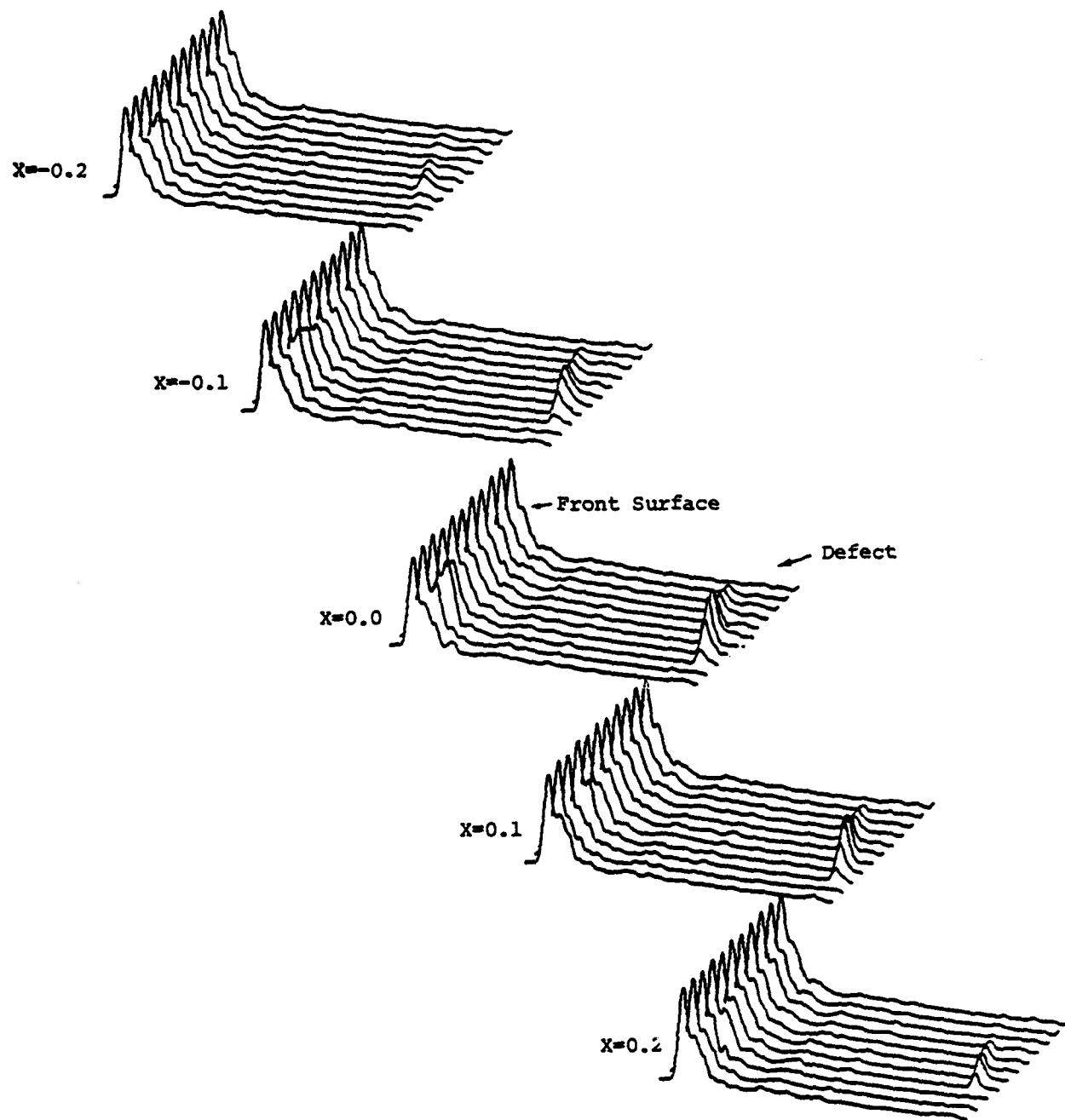
FIGURE 6.14: RECTIFIED WAVEFORMS OBTAINED FOR A 0° EDM
NOTCH DEFECT OF SIZE 20 x 100 MILS
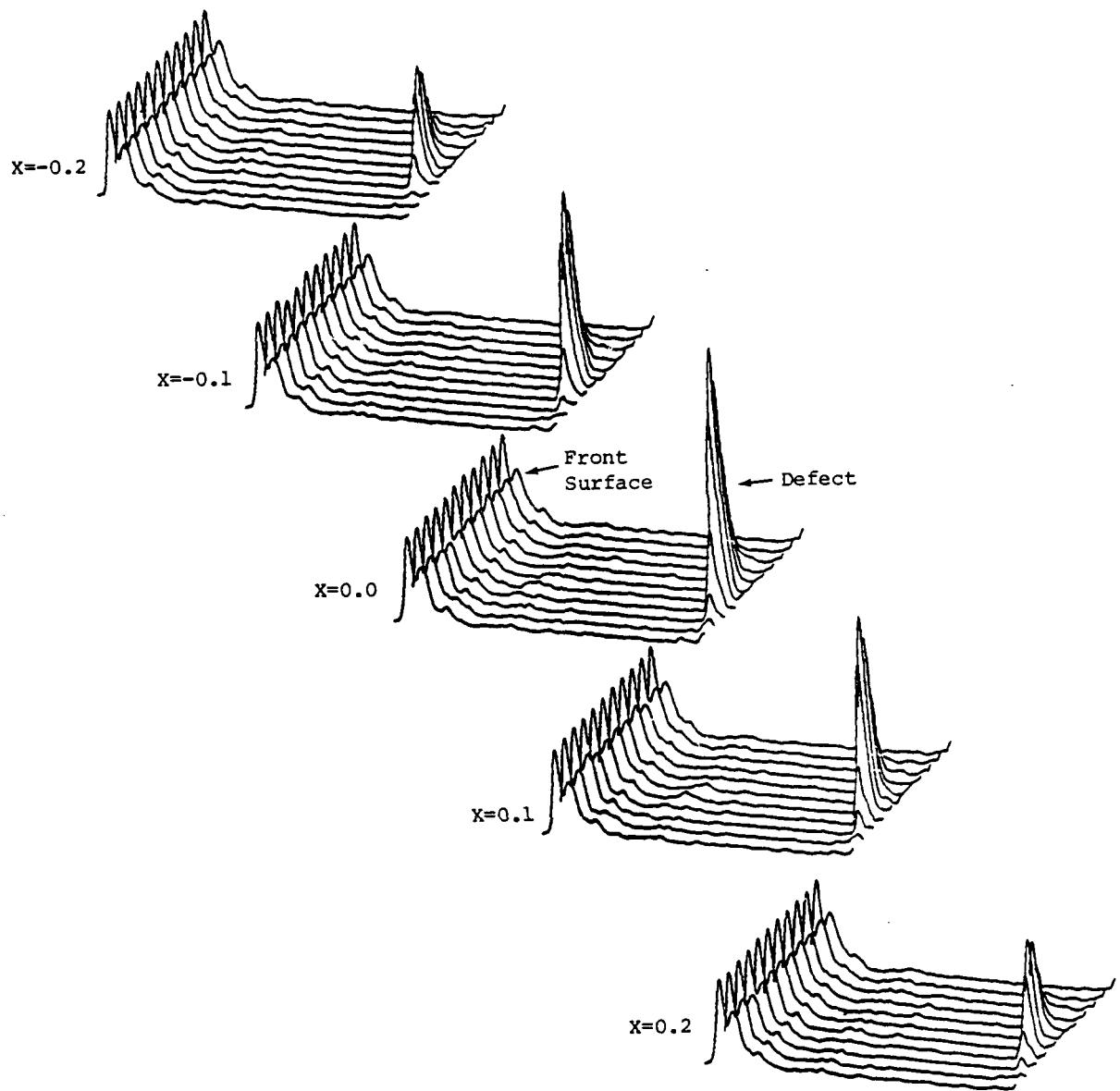
FIGURE 6.15: RECTIFIED WAVEFORMS OBTAINED FOR A 0° EDM
NOTCH DEFECT OF SIZE 80 x 400 MILS

with position, which would enable an image to be formed which would color the image in more than a conventional black/white fashion. The most logical way to form this colored image is to weight the scale from black to white according to the signal-to-noise ratio of the defect response. An example of this procedure is shown in Figure 6.16 for the 20 mil and 80 mil defect responses shown in Figures 6.14 and 6.15. Several different views of the images are shown so that a more direct visual interpretation of the flaw characteristics can be obtained. The illustrations presented here provide a much clearer description of the EDM notch responses than those shown in Figure 6.10 for the same defects. In fact, the indications of length and depth provided by the different viewing positions tend to confirm a notch-type defect. Representative images were obtained for the remaining defects in this test block and are shown in Figures 6.17 through 6.19. The same general trends identified above are also evident for these different size EDM notches.

Waveforms were also obtained from a 13/64 inch diameter 0° round-bottom hole using the inboard transmitter following the same procedures outlined above for the notch defects. The rectified waveforms for this defect are shown in Figure 6.20. The maximum amplitude occurred in the middle scan and decayed quickly for the RBH defect. The reflection was entirely lost after a movement of 0.2 inch. This observation is consistent with the expected results, because the curvature of the defect causes a change in direction of the large amplitude reflections. The rectified waveforms obtained from a 10/64 inch 0° flat-bottom hole defect are shown in Figure 6.21. The defect amplitude was nearly constant in the middle positions, which was expected from a rather uniform reflector. The amplitude decayed once the transducer moved outside the diameter of the FBH defect. Images of these rectified reaponses were not
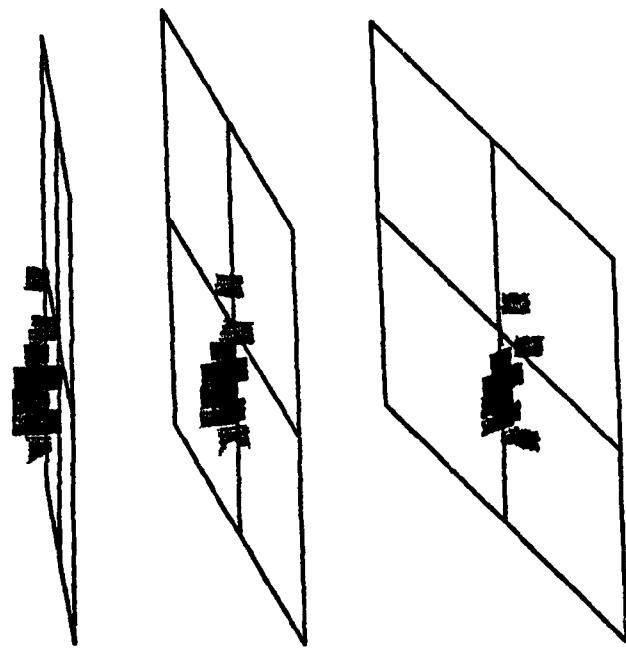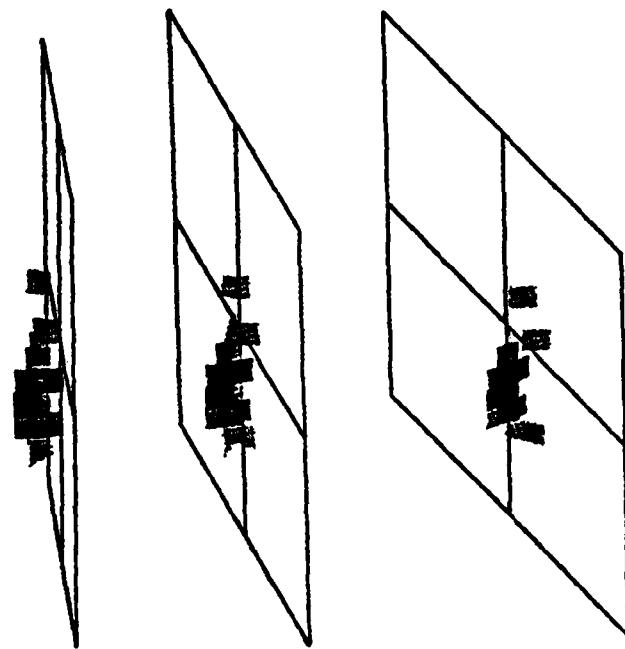
FIGURE 6.16: DIFFERENT VIEWS OF 0° EDM NOTCH DEFECT RESPONSES
(Images are Weighted by the Signal-to-Noise Ratio)

40 x 200

30 x 150
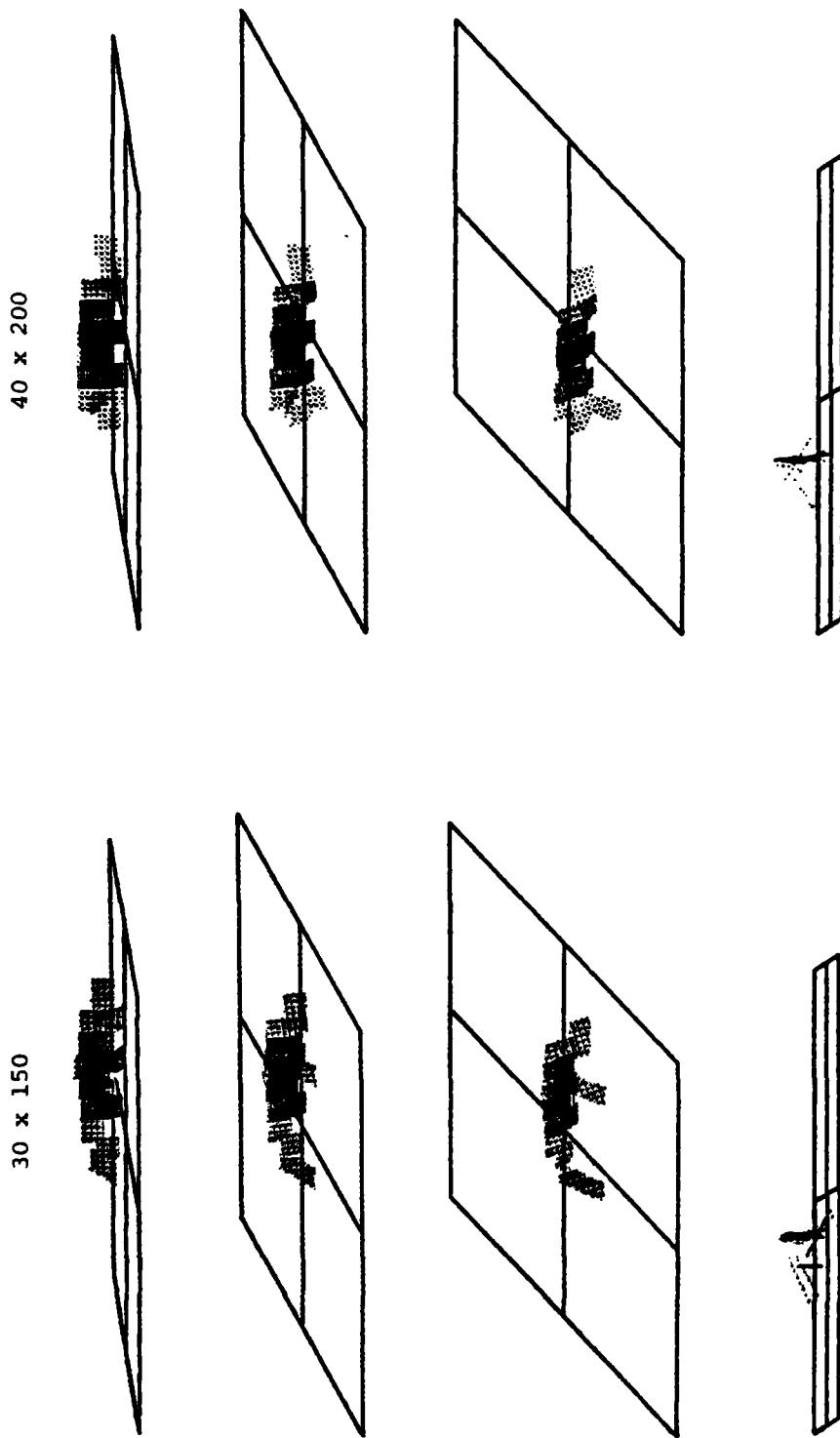
FIGURE 6.17: DIFFERENT VIEWS OF 0° EDM NOTCH DEFECT RESPONSES
(Images are Weighted by the Signal-to-Noise Ratio)
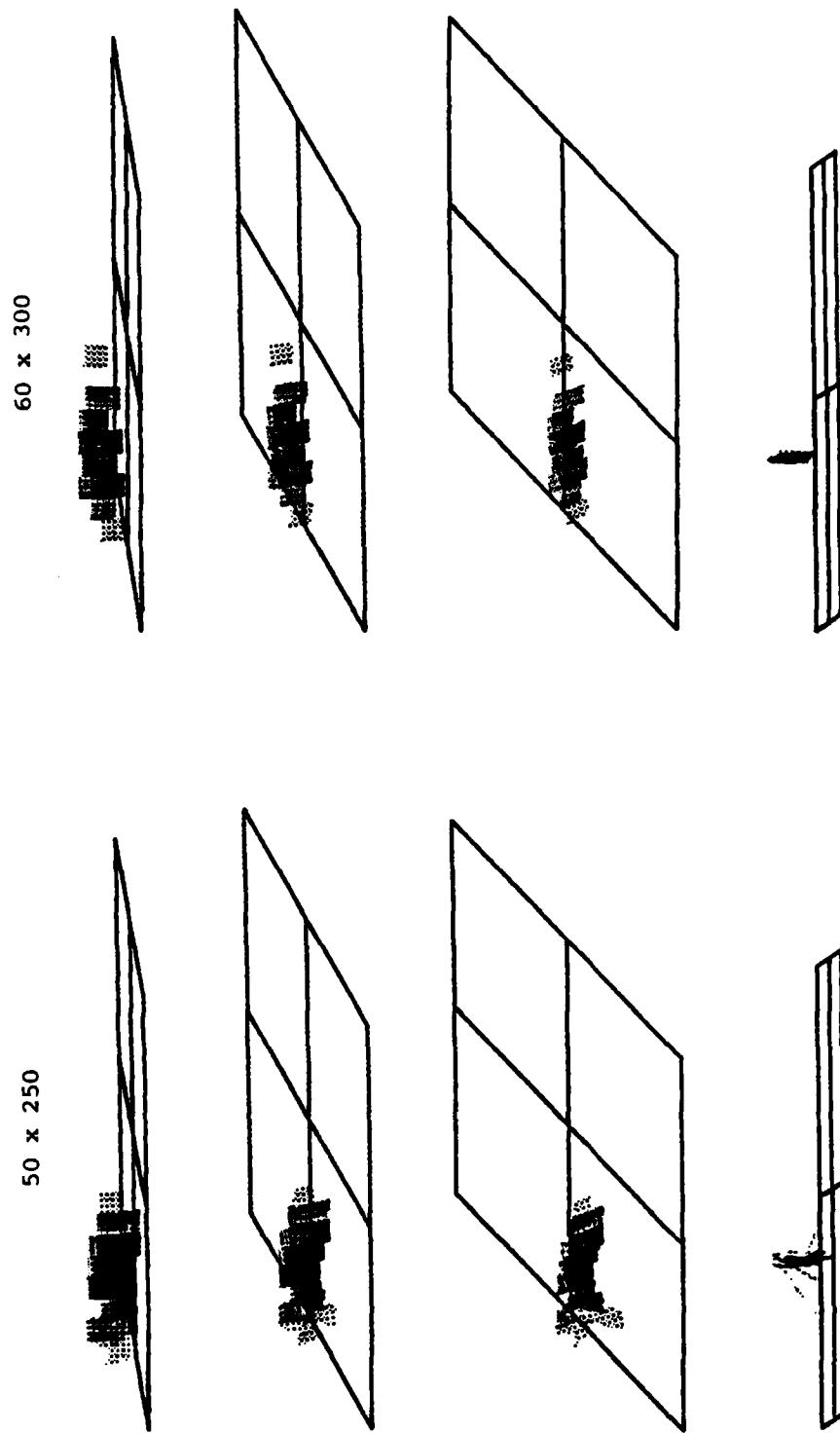
FIGURE 6.18: DIFFERENT VIEWS OF 0° EDM NOTCH DEFECT RESPONSES
(Images are Weighted by the Signal-to-Noise Ratio)

70 x 350
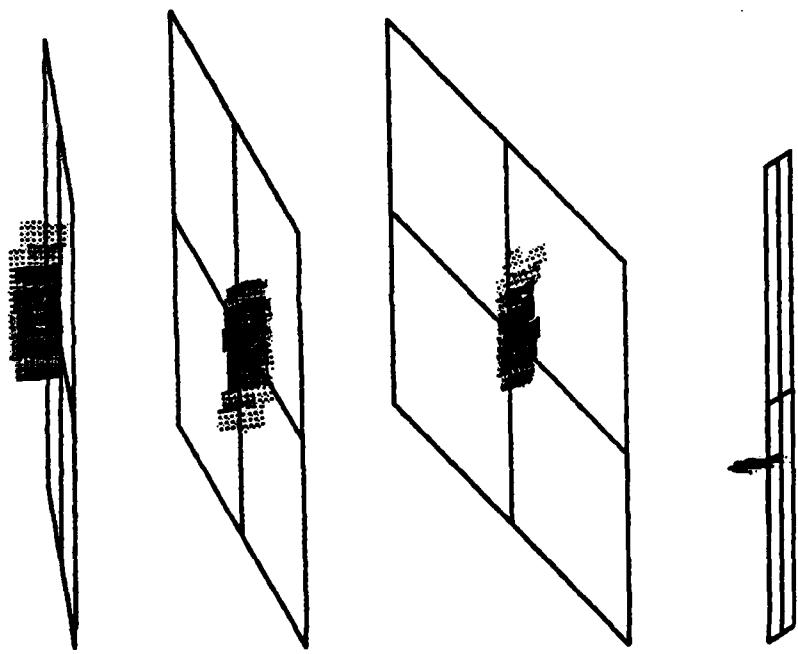
FIGURE 6.19: DIFFERENT VIEWS OF 0° EDM NOTCH DEFECT RESPONSES
(Images are weighted by the Signal-to-Noise Ratio)

Labels on figure: X=-0.2, X=-0.1, X=0.0, X=0.1, X=0.2, Front Surface, Defect, Back Surface
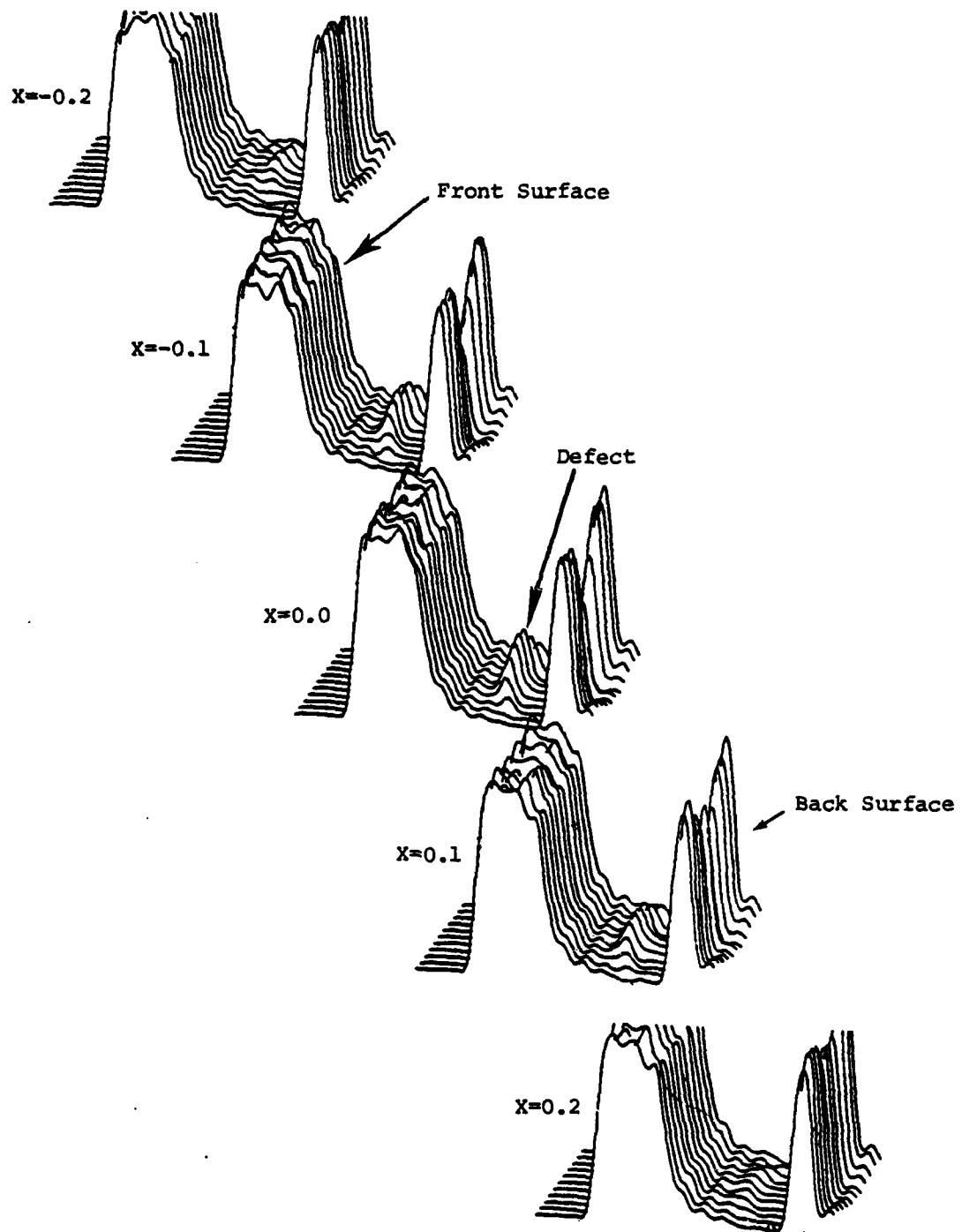
FIGURE 6.20: RECTIFIED WAVEFORMS OBTAINED FROM A 0°
ROUND-BOTTOM HOLE OF DIAMETER 13/64 INCH

Front Surface

X=-0.2

Defect

X=-0.1

Back Surface

X=0.0

X=0.1

X=0.2
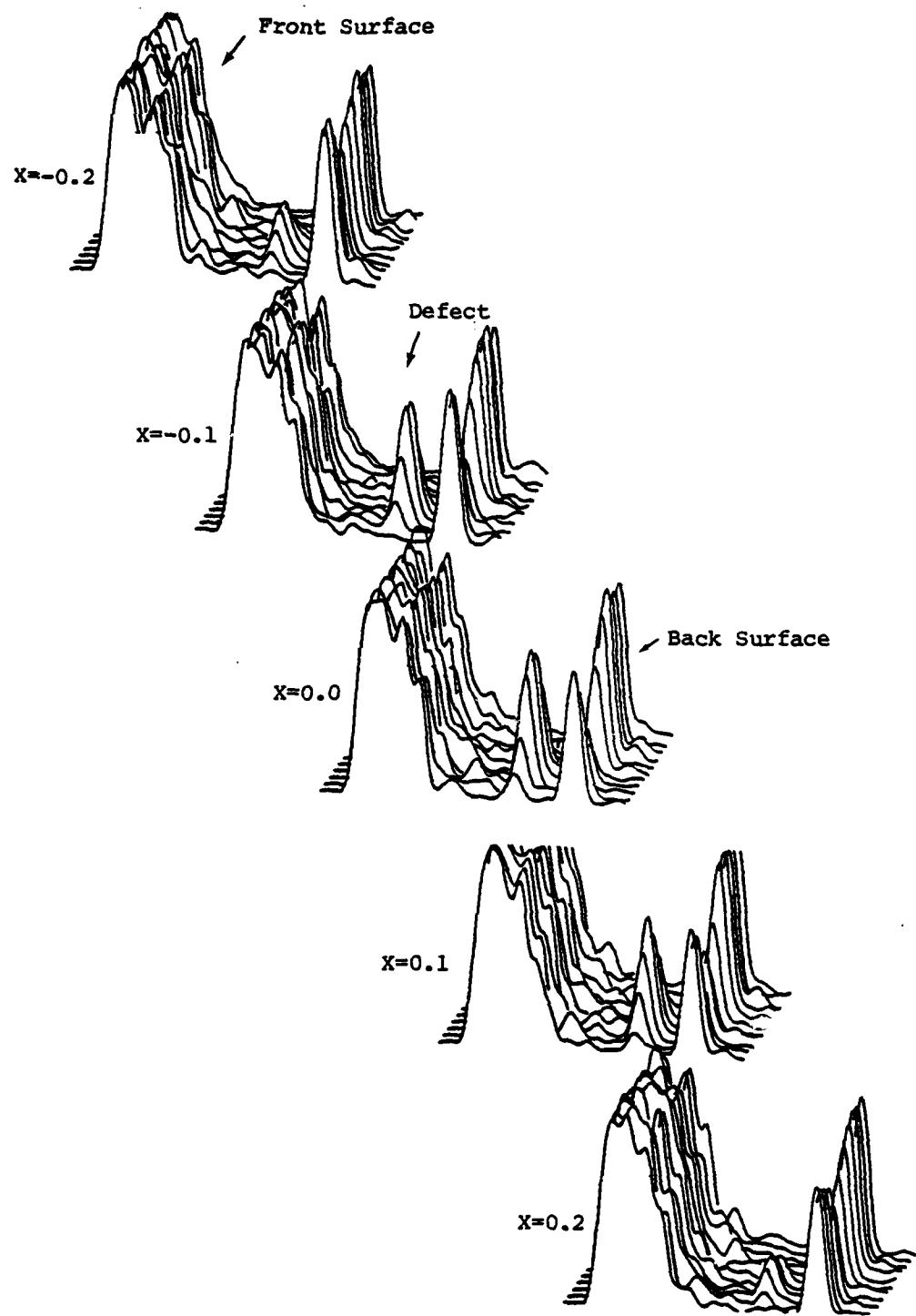
FIGURE 6.21:   RECTIFIED WAVEFORMS OBTAINED FROM A 0°
   FLAT-BOTTOM HOLE OF DIAMETER 10/64 INCH

6-21

drawn; however, the images of these defects would be much narrower than those presented earlier for the EDM notch defects. The distinguishing characteristic between the RBH and FBH defect images is the flatter amplitude distribution for the FBH, while a sharp amplitude decay is visible for the RBH.

The images presented in this section contain sufficient information to assist an analyst in his visual interpretation of the flaw characteristics. A combination of these improved images with the characterization activities described in the previous chapter could prove to be a very important tool for many nondestructive evaluation applications. A more stringent application of these techniques will be described in the section which follows.

6.3 SPECIAL TESTS

The defects considered thus far in this report are types that have been machined into steel test blocks. These flaws are rather smooth and symmetrical, whereas, in reality, flaws are often characterized by multiple, adjacent defects and/or highly irregular shapes. Two special cases have been considered and are discussed in this section. One case concerned the placement of a series of multiple artificial defects close to each other to determine if any indication of these multiple targets was present in the reflected signals. The second case involved the detection of a fatigue crack in a test block.

A series of four EDM notches was placed into four Aluminum test plates according to the specifications shown in Figure 6.22. Cases 1, 2, and 3 involved EDM notches of constant depth, but the spacing between the defects

CASE 1 - constant depth,
150 mil spacing

150
mils

CASE 2 - constant depth,
100 mil spacing

100
mils
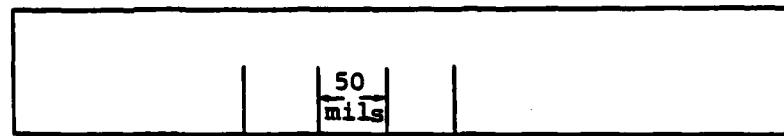
CASE 3 - constant depth,
50 mil spacing

50
mils
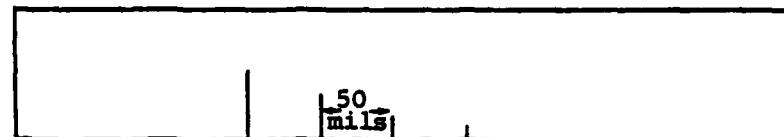
CASE 4 - different depths,
50 mil spacing

50
mils

FIGURE 6.22: CONFIGURATION OF DEFECTS IN ALUMINUM PLATES

varied from 150 to 50 mils. Case 4 consisted of four notches of different depths, with a 50-mil spacing between the defects.

Ultrasonic waveforms were collected from each of these plates using the outboard transmitter/receiver. The transmitter/receiver was moved a distance of 40 mils across the top of the notches for each successive collection. The waveforms are shown in Figure 6.23 for each of the four test cases. These waveform sets exhibited some very interesting characteristics which could be used to obtain information relative to the defect sequences.

In Case 1, the position of the maximum amplitude changed as the transducer was moved across the defect sequence. In some of the waveforms obtained for this case, a double peak appeared, which may lead an analyst to conclude that multiple defects were present. The smaller defect spacing for Case 2 appeared to manifest itself as a sharp increase in the duration of significant energy; however, the fine 50-mil spacing for Case 3 was difficult to detect through a visual comparison of the defect responses. The waveforms obtained for Case 4 presented a rather unique pattern. In some instances, two distinct arrivals were seen, while in the later waveforms, the individual arrivals appeared to coincide in time.

The purpose of these tests was to determine if any information could be obtained from the Aluminum test plates which could be used to infer the presence of multiple defects. The positional responses shown for these tests certainly deviated from the single defect responses shown in earlier sections. The deviations could be used to justify more detailed examinations of the flaw areas to determine if any additional quantitative information could be derived from the ultrasonic echoes.
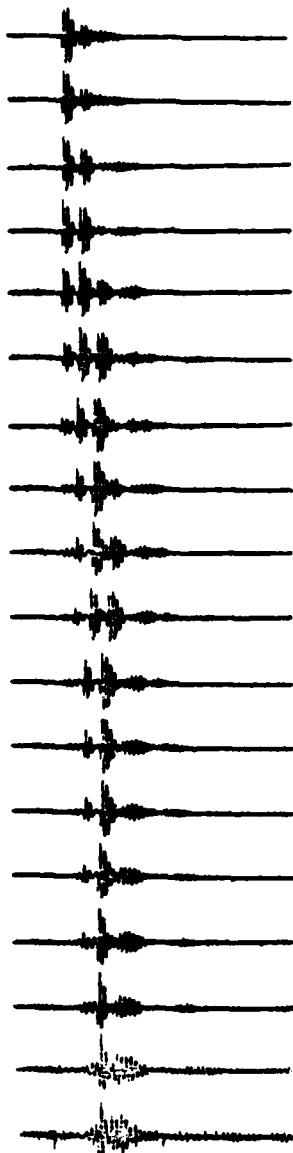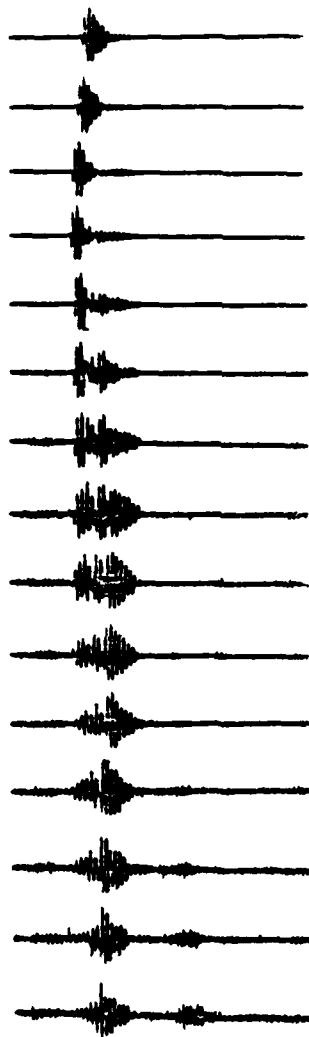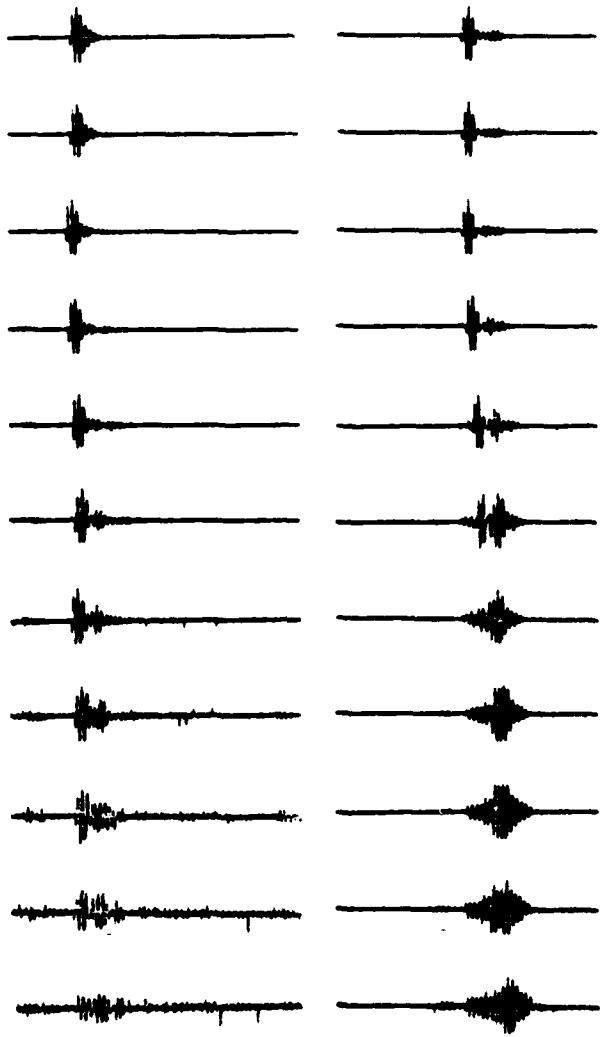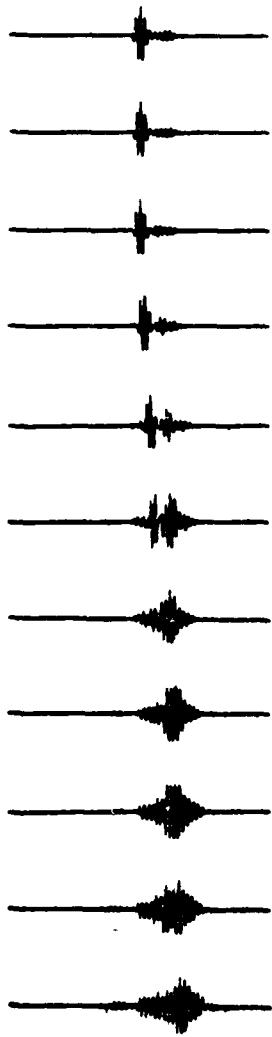
FIGURE 6.23: COMPARISON OF WAVEFORMS RECORDED FROM
THE FOUR ALUMINUM TEST PLATES

The second special test was related to a fatigue crack placed in a steel block (EPRI Block EPT-18). Two fatigue cracks are located in this test block. The rectified waveforms obtained from the larger defect are shown in Figure 6.24. It is interesting to note that this crack is not a simple defect but consists of several distinct cracks. This fact was essentially verified by the waveforms shown in this figure. The amplitude of the insonified region rises and falls throughout the scan. Ultrasonic images were prepared for this fatigue crack and are presented in Figure 6.25. The complexity of this crack is clearly depicted in these images: several local maximum-amplitude and minimum-amplitude regions can be seen.

The special tests performed during this project were designed to demonstrate potential field applicability of the developed techniques. The evaluations described in this section were not totally exhaustive but do indicate that the results obtained from the machined specimens can be applied to more complex defect geometries to obtain some information which would assist the analyst in defect characterization.

X = +0.4

X = -0.3

λ = -0.2

X = 0.1

X = 0.0

X = 0.1

X = 0.2

X = 0.3

X = 0.4
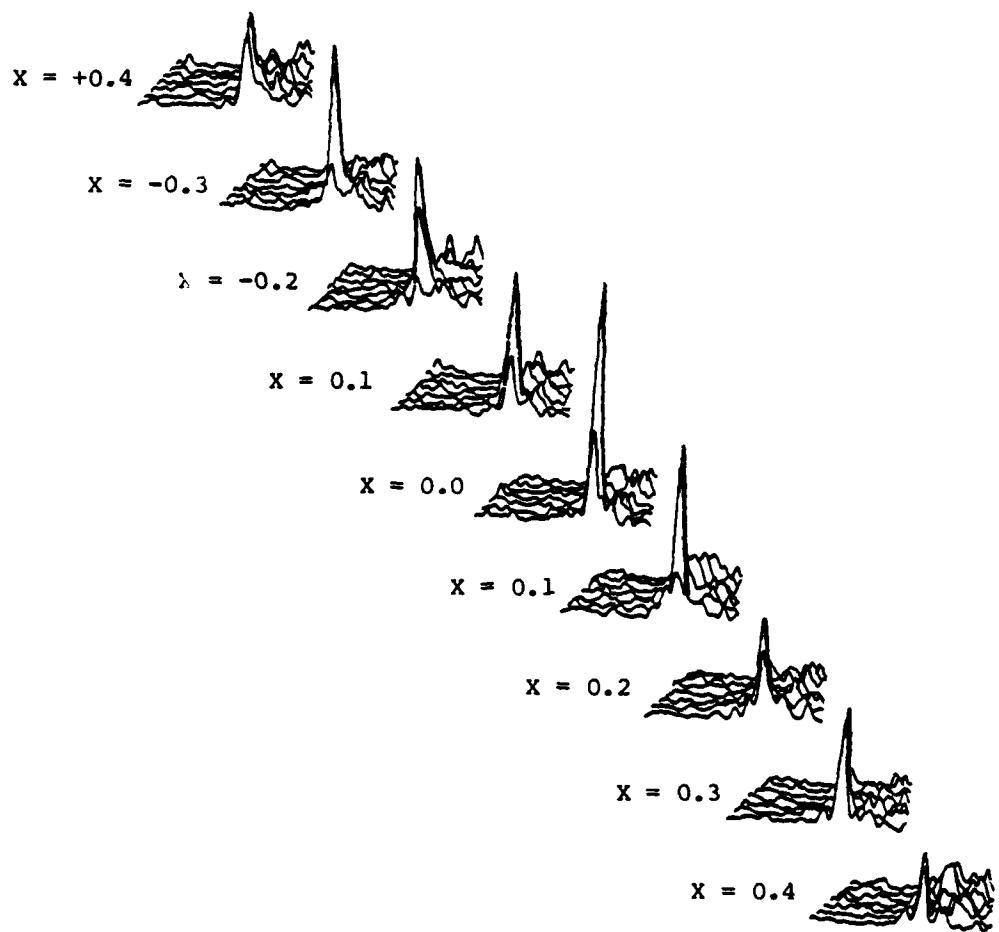
FIGURE 6.24:   RECTIFIED WAVEFORMS OBTAINED FOR THE LARGER FATIGUE CRACK
   LOCATED IN EPRI BLOCK EPT-18
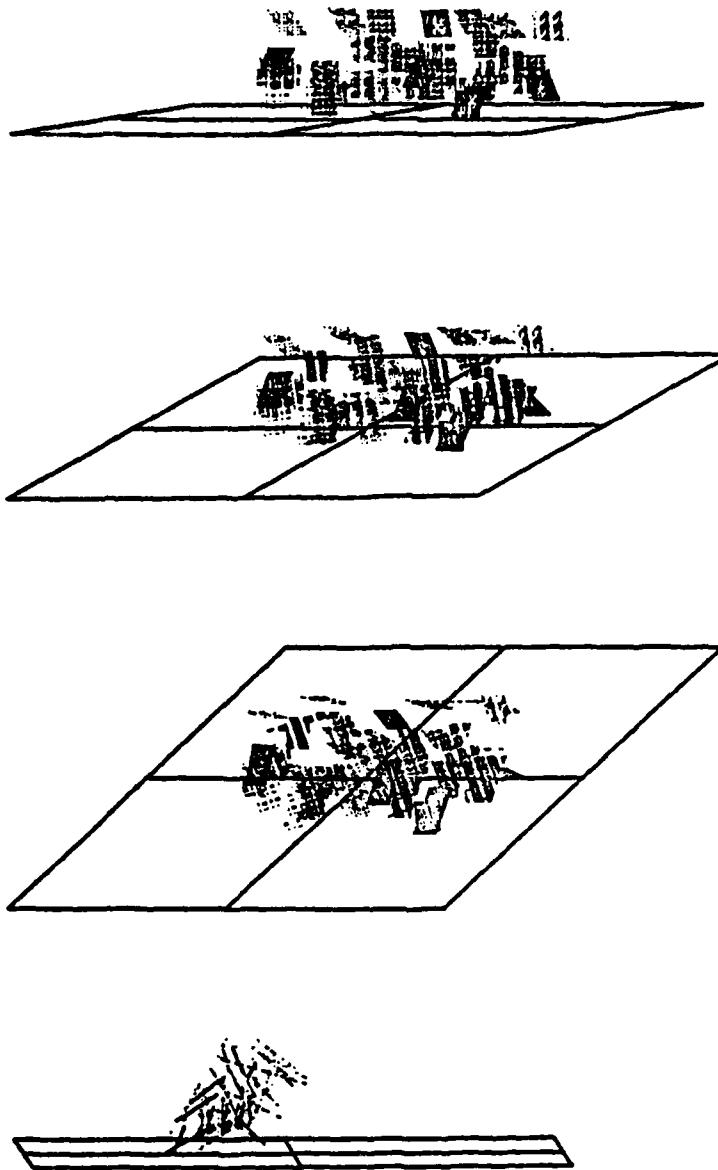
FIGURE 6.25: DIFFERENT VIEWS OF THE FATIGUE CRACK LOCATED IN EPRI BLOCK EPT-18 (Images are weighted by the signal-to-noise ratio.)

7. CONCLUSIONS AND RECOMMENDATIONS FOR FUTURE WORK

Results obtained during the performance of this project indicate that significant improvements in capabilities of existing ultrasonic imaging systems can be obtained through a combination of linear array technology, signal processing, and Adaptive Learning Network modeling.

A large aperture linear array has been used to record the pulse-echo signal as well as the diffracted and mode-converted signals resulting from the interaction of the input sound wave and the defect. The availability of these various signal types was extremely helpful in the defect characterization activities. Both temporal and spatial beamforming algorithms were applied to the recorded waveforms and were successful in improving the signal-to-noise ratios of the defect responses. Detection of the defect responses was accomplished by means of an advanced algorithm which was much more sensitive to the smaller-sized defects than the conventional pulse-echo imaging system. The use of the ALN methodology in defect characterization has been shown to be far superior to conventional schemes in which defect characteristics are inferred from an ultrasonic image.

The activities described above can be incorporated into an automatic system to provide information directly to the analyst concerning detection and characterization of flaw responses. This is a primary area recommended for future development. Other areas of recommended future work concern investigation of phase-steered and focused transmitters, incorporation of more elaborate scanning mechanisms (including variable transducer emergent angles), and testing of algorithms developed under this program on a specific application of interest.

8. REFERENCES

Achenbach, J.D., A.K. Gautensen, and H. McMaken, "Application of Geometrical Diffraction Theory to Quantitative Nondestructive Evaluation Analysis," Interdisciplinary Program for Quantitative Flaw Definition, Special Report Fourth Year Effort, AFML Contract F33615-74-C-5180, Science Center, Rockwell International, July 1978, pp. 31-38.

Becker, F.L., V.L. Crow, T.J. Davis, S.R. Doctor, B.P. Hildebrand, D.K. Lemon, and G.J. Posakony, Development of an Ultrasonic Imaging System for Inspection of Nuclear Reactor Pressure Vessels, Electric Power Research Institute, Palo Alto, CA, NP-1229, October 1979.

Domay, E., K.E. Newman, and S. Teitel, "Elastic Wave Scattering by General Shaped Defects: The Distorted Wave Born Approximation," Interdisciplinary Program for Quantitative Flaw Definition, Special Report Fifth Year Effort, AFML Contract F33615-74-C-5180, Science Center, Rockwell International July 1980, pp. 1-6.

Lane, S.S. and D.K. Lemon, "Automatic Interpretation of Ultrasonic Imaging," Paper presented at ARPA-AFML Conference on Nondestructive Evaluation, La Jolla, CA, July 1979.

Lemon, D.K., G.J. Posakony, J.R. Skorpik, and V.L. Crow, Investigation of Flaw Characterization Through Application of Ultrasonic Linear Arrays and ALN Technologies, Final Report No. 23111 03373, DARPA Contract MDA903-78-6-0223, June 1980.

Mucciardi, A.N., et al., Signal Processing for ISI - Interim Report, Electric Power Reseasrch Institute, Palo Alto, CA, NP-1421, May 1980.

Newhouse, V.L. and E.S. Furgason, "Development of Digital Techniques for Improved Flaw Detectability by Ultrasound Systems (Flaw-to-Grain Echo Enhancement by Frequency Agility)," Section 8 of EPRI NDE Program Progress Report, October 1980.

O'Brien, L.J., N.A. Aravanis, and A.N. Mucciardi, "Application of Adaptive Learning Network Signal Processing Techniques to Ultrasonic Imaging," Paper presented at the Fifth International Symposium on Ultrasonic Imaging and Tissue Characterization, National Bureau of Standards, Gaithersburg, MD, June 1980.

Posakony, G.H., "Acoustic Imaging - A Review of Current Techniques for Utilizing Ultrasonic Linear Arrays for Producing Images of Flaws in Solids," Elastic Waves and Nondestructive Test of Materials, ASME, NY, 1978.

Wells, Peter N.T., Physical Principles of Ultrasonic Diagnosis, Academic Press, London and New York, 1969.

Whalen, M.F., L.J. O'Brien, and A.N. Mucciardi, "Application of Adaptive Learning Netowrks for the Characterization of Two-Dimensional and Three-Dimensional Defects in Solids," Interdisciplinary Program for Quantitative Flaw Definition, Special Report Fifth Year Effort, AFML Contract F33615-74-C-5180, Science Center, Rockwell International, July 1980, pp. 50-76.